Università degli Studi di Milano–Bicocca
Facoltà di Scienze Matematiche, Fisiche e Naturali

Scuola di dottorato di Scienze
Corso di Dottorato di Ricerca in Fisica e Astronomia

The use of optical coherence for instrumentation devoted to CMB experiments

Coordinatore: Prof. Claudio Destri
Tutore: Prof. Massimo Gervasi

Tesi di: **Sebastiano Mauro Spinelli**
Matricola: **032914**

XXII ciclo
anno accademico 2008-2009

Contents

List of Tables

List of Figures

"Strive to enter by the narrow door, for many,
I tell you, will seek to enter and will not be able"
Luke 13, 24.

Foreword

The progress in the study of Cosmic Microwave Background (CMB) radiation is pushing observations towards the detection of tiny features of this radiation field that nevertheless contain precious information about the universe. The community is therefore forced to develop detection techniques that are very sensitive and accurate.
The subject of this thesis is the application of the concept of optical coherence to novel instrumentation dedicated to the study of CMB polarization and of the SZ effect from which we hope to extract lot of information.
The complex degree of mutual coherence γ_{12} is used to describe the performances of QUBIC (Q and U Bolometric Interferometer for Cosmology), a millimeter wave bolometric interferometer devoted to the study of CMB polarization fields up to multipoles $\ell \sim 125$. In the framework of the QUBIC collaboration two studies have been carried out.
An adding, single baseline, interferometer prototype, working in the 90 GHz WR10 waveguide band, has been assembled to test the basic properties of mm-wavelength bolometric interferometry in a mm-wave laboratory. Each instrument component has been tested with a Microwave Vector Network Analyzer (MVNA) to unveil systematic effects. This is a crucial aspect for an experiment that aims to detect CMB polarization B-modes. The most relevant result of this analysis is the study of the signal amplitude modulation induced by the phase shifters. The system has also been tested with large bandwidth (30%) signals in order to investigate its wide band response. Bandwidth smearing ($\gamma_{12} = 0.96 \pm 0.03$ in the WR10 band) is observed even if ideally it should not be present, since the phase shifters are ideally frequency independent. This is induced by frequency dependent asymmetries between the two interferometer branches that alters their electrical length.

The low transmission of the system (-7 dB maximum, -20 dB in the band tails) prevents the detection of major spurious systematic signals, since their effect is dominant at the borders of the bandwidth. This fact, combined with the frequency integration done by the wide-band detector washes out most of the systematic effects. Finally, the interferometer has been used to illuminate a 4K cooled bolometer to verify the principle of bolometric interferometry.
The final QUBIC instrument will consist in a set of modules with a 20% bandwidth and each equipped with 144 horns looking at the sky. QUBIC aims to observe the CMB B-modes (supposing a tensor to scalar ratio r=0.01) with 1 year of integration time. QUBIC will combine sky signals thanks to a Fizeau combiner, an optical system that produces a measure of γ_{12} of the observed source in its focal plane. The 4th chapter of the thesis concerns the definition and analysis of the optical properties of such a combiner.
To guarantee a clean detection of B-modes the optical combiner has to produce interference fringes with efficiency as close to 1 as possible in order to maximize its sensitivity. The combiner must have an effective focal length f_{eq} bigger than 200 mm in order to Nyquist sample fringes corresponding to multipoles up to ℓ ∼125 considering a bolometer size of 5 mm. On the other hand f_{eq} has to be less than 300 mm in order not to have a focal plane filled with unrealistic number (thousands) of detectors. Moreover the optical system has to be compact (scale size less than ∼ 1m) in order to be lodged in a 4K cryostat.
A simulation machine for the combiner is defined with the ZEMAX simulation code and then applied to various optical layouts. Since the combiner is operated in a coherent way and ZEMAX is not able to simulate the Coherent Transfer Function, the efficiency has been estimated computing the modulus of the complex degree of mutual coherence form the complete fringes patterns simulated with ZEMAX.
Deviations from ideality of the instrument produce incoherent illumination: for this reason incoherent performances have been studied with the simulation and analysis of the combiner Optical Transfer Function. The most favorable solution that fits the requirement is a gregorian like, off-axis telescope, however given its small focal ratio ($F_{\#}$ ∼0.5) aberrations are large

and its design must be accurately optimized in order to maximize its efficiency.

The last part of the thesis is devoted to the use of the complex degree of self coherence to investigate the SZ effect, using a Fourier Transform Spectrometer (FTS) based on the classical Michelson two beam interferometer.

The optical design of a double FTS instrument based on the layout, proposed by Martin and Pupplet, is developed for the focal plane of the telescope of the SAGACE space mission of the Italian Space Agency.

A double coupled spectrometer is proposed, in order to increase its sensitivity compared to existing similar instruments, where half of the power is rejected.

The outputs of a first polarizer, placed in the spectrometer input, feed two equal, symmetric spectrometers with a common mechanical drive for the insertion of the optical path difference required to achieve the spectral resolution needed for the observations. This procedure equalizes the optical path difference in the two branches. Signals in the output of these two spectrometers are recombined with another common polarizer before being split in 4 frequency bands (100-200 GHz, 200-300 GHz, 300-400 GHz, 700-740 GHz) and detected with 4 bolometric detector arrays.

The layout is projected in order to be lodged in a cylinder with 800 mm diameter and 750 mm height. This cylinder will be inserted inside a cryostat fed with a 800 lt helium tank that will ensure a 2 year lasting mission.

Chapter 1

CMB Physics

Since its discovery in 1965 [1], Cosmic Microwave Background (CMB) has been one among the most powerful tools in cosmology.
Nowadays, in the so called precision cosmology era, CMB still plays an important role in understanding all the different properties observed and expected in the universe, and in certain particular cases is the most direct way to verify predictions coming from theories.

1.1 The CMB frequency spectrum

One of the most important features of CMB is the blackbody spectrum, as proved by FIRAS (Far InfraRed Absolute Spectrometer) [2]. FIRAS, together with experiments at lower frequencies, showed that the CMB follows the blackbody spectrum for over a factor approximatively 1000 in frequency. This implies that the universe was in thermal equilibrium when the radiation was released, at a temperature $\sim$ 3000 K. The blackbody temperature of CMB is nowadays 2.725$\pm$0.002 K [3] and its peak is around $\sim$ 160 GHz. Even if the CMB blackbody spectrum has been so well observed, it's still interesting to look for spectral distortions inside it, since they could provide information on mechanisms of energy exchange that could operate in the universe since the very beginning of its life up to now.
Among the processes that generate spectral distortions there is the scattering of CMB photons by electrons with kinetic temperatures higher than the CMB radiation field temperature.

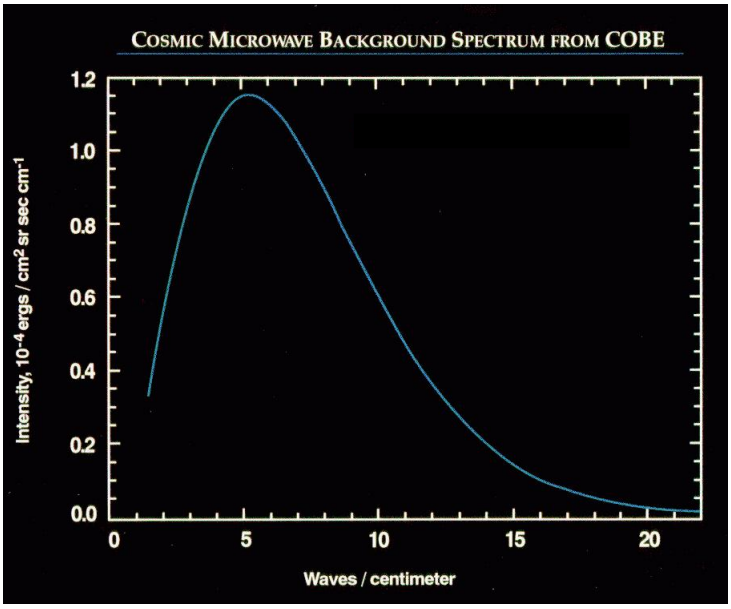

Figure 1.1: Best fit of FIRAS data to the CMB blackbody frequency spectrum. Picture taken from [3]

This phenomenon (inverse Compton scattering) played a role in generating the so-called "y distortion" of CMB [3], and nowadays generates the Sunyaev Zel'dovich [4] effect towards galaxy clusters.

1.2 The Sunyaev Zel'dovich effect

It's widely known that galaxy clusters are filled with a maxwellian distributed electrons gas with density $N_e \sim 10^{-3} - 10^{-2}$ cm^{-3} and temperatures of the order of $T_e \sim 10^8$ K. Bremsstrahlung emission from this gas has been detected and analyzed by X-ray space missions.
The interaction (inverse Compton scattering) of the CMB photons with this hot gas induces (SZ effect [4]) a spectral distortion of its blackbody spectrum, leading to a decrement of photons in the Rayleigh-Jeans region and to an increase of photons in the Wien spectral region.

1.2.1 Thermal SZ

Let's suppose we model a cluster of galaxies filled with hot gas with a plasma cloud with a Thomson scattering optical depth τ_T

$$\tau_T = \int \sigma_T N_e dl, \tag{1.1}$$

where l is measured along the line of sight that crosses the cloud center.
Suppose we have a maxwellian distribution of electrons and a blackbody spectrum of the CMB with $h\nu \ll k_b T_e$, then the spectrum, will suffer of a distortion with the net effect of increasing the photons frequency. The distortion appears as a decrement of photons in the Rayleigh-Jeans part of the spectrum and increment of photons in the Wien part.
This result can be obtained starting from the Kompaneets equation applied to CMB radiation field [4]

$$\frac{\partial I_\nu}{\partial y} = x \frac{\partial}{\partial x} x^4 \frac{\partial}{\partial x} \frac{I_\nu}{x^3}, \tag{1.2}$$

where $x = \dfrac{h\nu}{k_b T}$ is a proper adimensional frequency parameter and y, defined as

$$y = \int \frac{kT_e}{m_e c^2} \sigma_T N_e(l) dl = \frac{kT_e}{m_e c^2} \tau_T, \tag{1.3}$$

is the Comptonization parameter.
Recalling that variations are small with respect to the mean CMB temperature, the solution to this equation corresponds to a relative change of brightness temperature

$$\frac{\Delta T_r}{T_r} = \frac{\Delta I_\nu}{I_\nu} \frac{dln T_r}{dln I_\nu} = y \left(x \frac{e^x + 1}{e^x - 1} - 4 \right). \tag{1.4}$$

This function has a minimum at $x \sim 1.78 \sim 94$ GHz (for CMB, RJ Rayleigh Jeans spectral region) and a maximum $x \sim 6 \sim 344$ GHz (for CMB, Wien spectral region). The frequency with zero distortion is at $x \sim 3.83 \sim 217$ GHz for CMB (see fig. 1.2). For a given y the flux spectral density per unit solid angle in the direction of the cluster does not depend on redshift z, since it depends only on x that in the standard cosmological model is independent of z[1].

[1]The adimensional frequency is defined as $x = \dfrac{h\nu}{k_b T}$ that does not depend on z since in the standard cosmological model both ν and T present the same linear scaling with redshift.

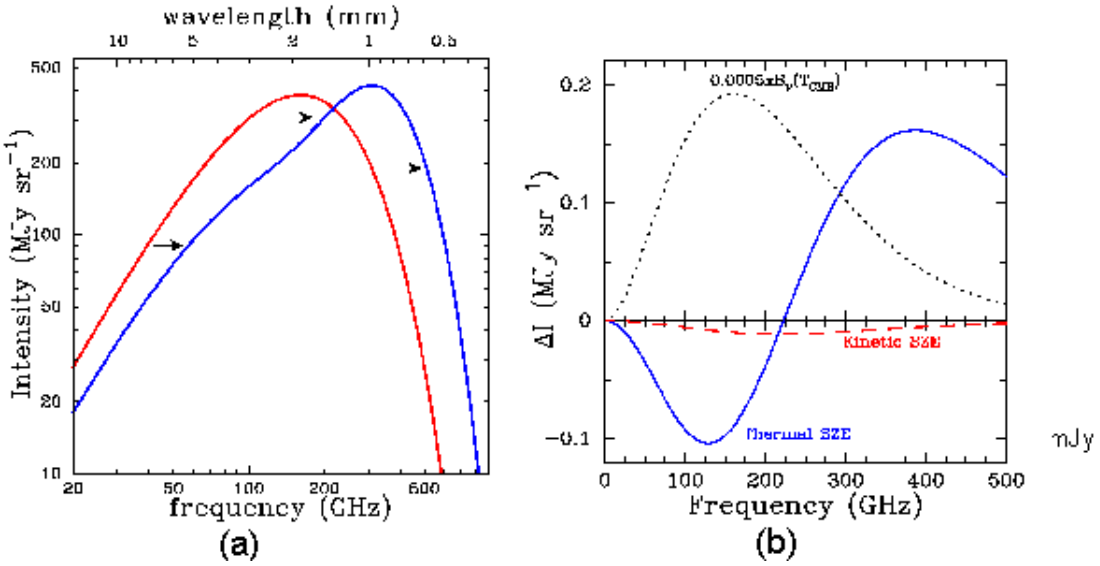

Figure 1.2: Left panel: the effect of SZ effect (blue line) on the CMB blackbody frequency spectrum (red line). Right panel: difference (blue line) between the CMB blackbody spectrum and the SZ altered one. In red the kinematic SZ effect.

1.2.2 Kinematic SZ effect

The motion of the cluster along the line of sight with respect to the CMB frame is another source of distortion on the CMB spectrum induced by the Doppler effect.

Consider a cluster moving with velocity v_r with respect to the CMB, then the expected distortion from this effect is [4]

$$\frac{\Delta T}{T_{CMB}} = -\frac{V_r}{c}\tau_T. \tag{1.5}$$

This effect is called *kinematic* SZ effect and should be more easily detected in the proximity of the crossover frequency ($x \sim 3.83$) where the thermal SZ effect vanishes to zero.

1.2.3 Cosmology with the SZ effect

Combining both X-ray data of the thermal bremsstrahlung emission and of the radio SZ data it's possible to derive the intra-cluster gas density and the linear dimension of the cluster. This latter parameter enables the use of SZ detected galaxy clusters as universal rulers for the scale of distance analysis.

Suppose for simplicity a isothermal spherical cloud with a constant radial independent gas distribution[2]: then in the direction of the cloud center the bremsstrahlung brightness is

$$I_\nu = 2AN_e^2 T_e^{\frac{1}{2}} e^{-\frac{h\nu}{kT_e}} g(\nu, T_e) R, \tag{1.6}$$

where A is a constant, g is the Gaunt factor and R is the cloud radius.
In the same time a CMB intensity decrement in the RJ spectral region due to SZ effect is expected, so that

$$\frac{\Delta T_r}{T_r} = -\frac{4kT_r}{m_e c^2} \sigma_T N_e R. \tag{1.7}$$

Using multiple X-ray observations at different energies T_e can be estimated, leaving a system with two equations and two unknowns, N_e and R.
The determination of R is crucial in cosmology since, having it and the cluster angular size one can directly obtain the cluster distance. Then if also the cluster redshift is known, the Hubble constant H_0 can also be estimated via the Hubble law.

Cosmological models test

Having the linear dimension of a cluster and its distance enables to derive cosmological parameters but also to perform cosmological model tests. For example, consider the case of a cosmological scenario where photon creation is possible [5], then in this case the scaling for temperature with redshift becomes

$$T(z) = T_0 (1+z)^{1-\beta}, \tag{1.8}$$

while for the photon frequency the usual scaling is preserved, so that

$$\nu(z) = \nu_0 (1+z). \tag{1.9}$$

In relation 1.8 β is a number expressing how many photons are created in the universe, $\beta = 0$ means the usual conservation case. Looking at the

[2]It's been shown that the gas distribution has a r^{-2} dependance that, combined with the fact that bremsstrahlung emission depends on N_e^2, makes X-ray gas detection sensitive only to the central part of the cluster. On the other hand, since its emission depends on N_e, SZ analysis could provide more information on intracluster gas physics towards the cluster borders.

dimensionless frequency x one gets in standard cosmology

$$x = \frac{h\nu}{kT} = \frac{h\nu_0(1+z)}{T_0(1+z)} = \frac{h\nu_0}{kT_0} = x_0, \tag{1.10}$$

while if condition 1.8 holds, x becomes

$$x = x_0(1+z)^{\beta}, \tag{1.11}$$

which is no longer independent of the redshift z, as for the case 1.10 of standard cosmology.
For example, a survey of the SZ effect towards galaxy clusters [6] located at different redshifts could test if 1.10, which is one of the strongest results of the standard cosmological paradigm, really holds.

1.3 CMB anisotropy and the angular power spectrum

The CMB shows an high isotropy level, up to 10^{-4}K. Moreover, going down to a 10^{-5}K level, CMB presents spatial anisotropy which is its second crucial feature. The description of CMB anisotropies is realized using the so called

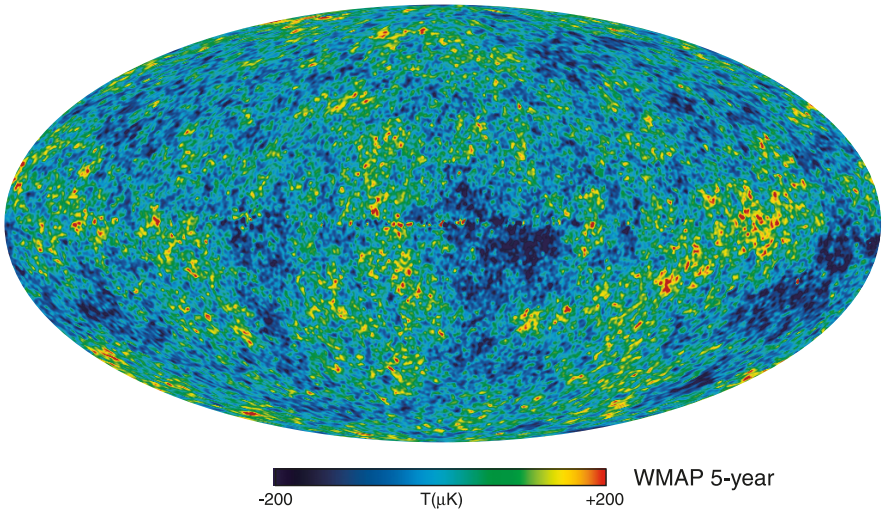

Figure 1.3: Map of CMB anisotropies with foregrounds removed. Picture taken from [7].

angular power spectrum.
Consider an observation of CMB brightness temperature in a direction $\hat{n}$:

the relative brightness temperature discrepancy of the CMB in this direction with respect to the average blackbody temperature $\langle T \rangle$ is defined as:

$$\Theta(\hat{n}) = \frac{\Delta T}{\langle T \rangle} = \frac{T(\hat{n}) - \langle T \rangle}{\langle T \rangle}. \tag{1.12}$$

This discrepancy is then usually decomposed in multipoles above the spherical harmonics base over the entire sphere, so that

$$a_{\ell,m} = \int_{4\pi} \Theta(\hat{n}) Y_{\ell,m}(\hat{n}) d\Omega. \tag{1.13}$$

The order m describes the angular orientation of a fluctuation mode, while ℓ express its angular size. The power spectrum $\langle \delta_{\ell,m} \delta_{\ell',m'} \rangle$ is then introduced and, since in the universe there is no preferred direction (m), it is expected that the power spectrum is independent from the order m. This means that

$$\langle \Theta_{\ell,m} \Theta_{\ell',m'} \rangle = \delta_{\ell,\ell'} \delta_{m,m'} C_\ell, \tag{1.14}$$

and the best estimate of the coefficients C_ℓ's is found by averaging over m. CMB anisotropy data reveal the initial inhomogeneities of the universe, caused by small overdensities arisen from a small adiabatic compression or expansion of the fluid that built up the universe in the recombination era. Some of the most relevant observations of the anisotropy power spectrum are presented in fig 1.4, taken from [8]. The horizon scale at decoupling is $\sim 1^\circ$: regions smaller than this size had time to compress before decoupling, these are the acoustic oscillations of CMB.

Modes with wavelengths larger than the horizon at decoupling time substantially do not evolve: this is explained by the fact that these modes correspond to distances larger than the one expressing the causal contact at that time. Large scale (small ℓ's) perturbations are observed in their almost original form when they were set down.

Smaller scales modes corresponding to acoustic peaks evolve in a different way. Consider for example the first peak in the power spectrum. As the mode enters the horizon, the perturbation starts to grow until it reaches a maximum at the time of recombination, hence the power spectrum will have a peak at the angular scale corresponding to the mode that just reached its maximum at recombination.

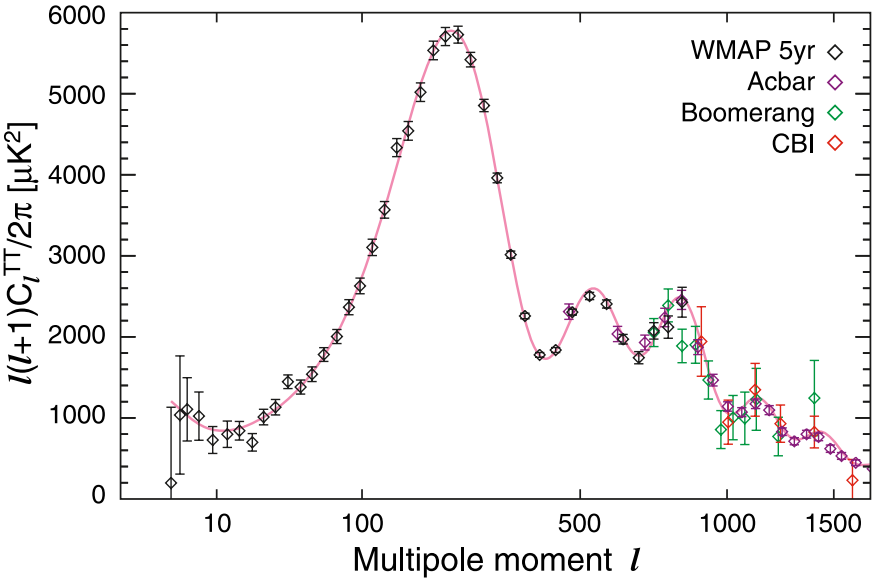

Figure 1.4: The angular power spectrum of CMB anisotropies. The red lines is the model best fit to data. Picture taken from [8].

At smaller scales perturbations had time to oscillate for more time, thus its amplitude in the power spectrum is a function of its phase at decoupling, leading to a series of maxima and minima for all perturbations with wavelengths smaller than the horizon size.
The damping of smaller scales perturbations, clearly seen experimentally, is a phenomenon called Silk damping and is related to the photon mean free path.

1.4 CMB polarization fields

The fact that the CMB photon distribution at the epoch of last scattering is slightly anisotropic directly means that there must be a (small) fraction of linear polarization in the CMB, due to the Thomson scattering the photons have with free electrons. In fact the Thomson scattering cross section depends upon the polarizations of the incoming and scattered polarizations $\hat{\epsilon}, \hat{\epsilon}'$ [9]:

$$\frac{d\sigma_T}{d\Omega} \propto |\hat{\epsilon} \cdot \hat{\epsilon}'|. \tag{1.15}$$

The presence of anisotropy is crucial. Incident light scatters a free electron, that starts oscillating in the direction of the incoming wave electric field E, that is the polarization direction. Now, if the incoming radiation were isotropic, orthogonal polarized states from incident directions separated by an angle of 90° degrees would combine so that the whole scattered radiation is unpolarized (see fig 1.5).
On the other hand if the incoming radiation distribution has a quadrupolar component the net result is a linear polarized outgoing radiation field. In

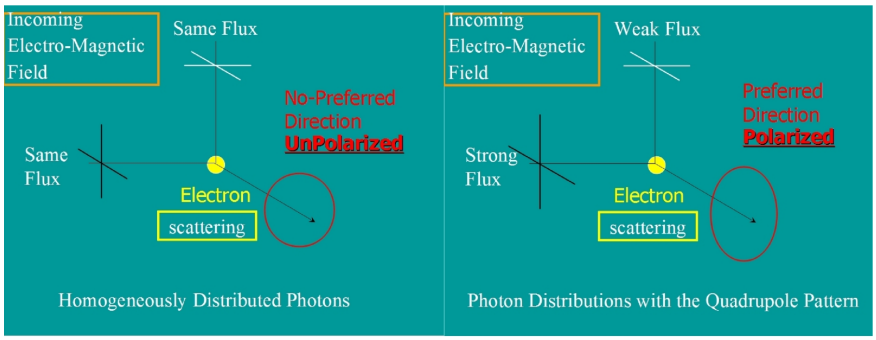

Figure 1.5: Example of polarized Thomson scattering produced by an anisotropic radiation field (right panel) compared to the isotropic unpolarized case (left panel)

terms of spherical harmonics the quadrupole ($\ell = 2$) component of the perturbation corresponds to 5 different modes, namely $m = 0, \pm 1, \pm 2$. These different temperature fluctuations have different physical origin and are respectively associated to scalar (compressive), vector (vortical) and tensor (gravitational waves) modes, as represented in fig 1.6. Each of them leads to a different polarization pattern of the CMB [9].

Each polarization field can be decomposed in two components: in complete analogy with the electro-magnetic field there will we be a gradient component called E mode and a curl component called B mode that build up the real field.
Scalar polarization is due to scalar perturbations and is generated by the quadrupolar component of the radiative field at the decoupling time via the Thomosn scattering process.
This process only produces E-type polarization.
Vector polarization is explained by vortical motions of matters like "eddies"

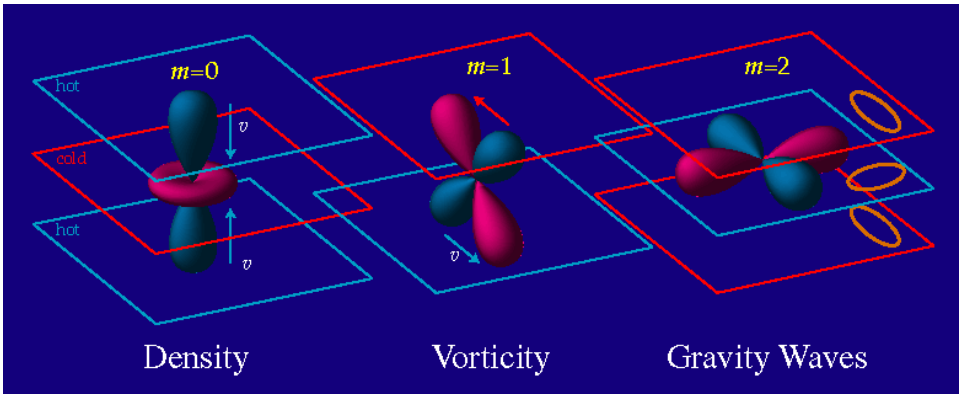

Figure 1.6: Different temperature fluctuations that arise from a quadrupolar component of perturbation [9].

in the water [9] and is made up by B modes. Moreover this processes is not associated with density perturbations and vorticity is damped by the expansion of the universe, since it is not amplified by gravity.
Tensor fluctuations are traceless perturbations of the space-time metric that can be seen as a gravitational wave. This perturbation induces a stretching of the space time in its directions, stretching also the wavelength of the incoming photons. The metric stretching produces a quadrupolar component in the radiative field. Thomson scattering again induces polarization.
Also tensor fluctuations decay with time, but with a rate much more slower than for vector perturbations. This fact, combined with the argument that scalar perturbations do not produce B modes means that the discovery of a B mode component in the CMB is a proof of the existence of tensor perturbations, that is of gravitational waves.

1.4.1 Statistical description

In general the polarization state of radiation in direction $\hat{\mathbf{n}}$ is described by the coherence matrix $\langle E_i(\hat{\mathbf{n}})E_j^*(\hat{\mathbf{n}})\rangle$, where E is the electric field vector in the plane perpendicular to the propagation direction, i j are polarization components in a given reference system and brackets denote a time average. The Stokes' parameters [12] can be recovered from this matrix, as usual Q and U parameters describe the linear polarization state while the circular state is encoded in the Stokes' V parameter. Specifically Q represents po-

larizations aligned to one of the principal axis of the polarization reference system, while U represents polarization 45° rotated with respect to this reference system.
The reference system dependance is a disadvantage of the Stokes' representation. This is why the CMB community usually describes the polarization state for an harmonic decomposition with a basis that is simply defined by the wavevector. For small patches of the sky (so that it can be considered being flat instead of spherical), the harmonic decomposition becomes a Fourier transform, so that the E, B harmonics can be defined as [10]

$$E(l) \pm iB(l) = e^{\mp 2i\phi_1} \int d\hat{\mathbf{n}} \left[Q(\hat{\mathbf{n}}) \pm U(\hat{\mathbf{n}})\right] e^{-il\cdot\hat{\mathbf{n}}}. \tag{1.16}$$

In this equation ϕ_1 is the angle the Fourier vector makes with the x coordinate system axis.
The generalization to the full curved sky is done by replacing the plane waves (that are the eigenfunctions of the Laplace operator in a flat space) with the tensor eigenfunctions for the curved space, namely the spin-2 spherical harmonics [10]. Via this change eq 1.16 provides the Stokes' parameters

$$\left[Q(\hat{\mathbf{n}}) \pm iU(\hat{\mathbf{n}})\right] = -\sum_{lm} \left[E_{lm} \pm iB_{lm}\right]. \tag{1.17}$$

In a way equivalent to the temperature field, power spectra can be defined as

$$\langle E^*_{lm} E_{l'm'} = \delta_{ll'}\delta_{mm'} C_l^{EE} \rangle \tag{1.18}$$

$$\langle B^*_{lm} B_{l'm'} = \delta_{ll'}\delta_{mm'} C_l^{BB} \rangle. \tag{1.19}$$

$$\tag{1.20}$$

In addition also the temperature-E-polarization correlation

$$\langle a^*_{lm} E_{lm} = \delta_{ll'}\delta_{mm'} C_l^{aE} \rangle \tag{1.21}$$

is present. All other correlations vanish if parity is conserved. The peak patterns in the observed spectra showed in figures 1.7,1.8 are in agreement with what was expected in the standard cosmological model. As expected, the oscillations in the polarization E mode are out of phase with respect to the temperature ones. By the way, the signal enhancement at great angular

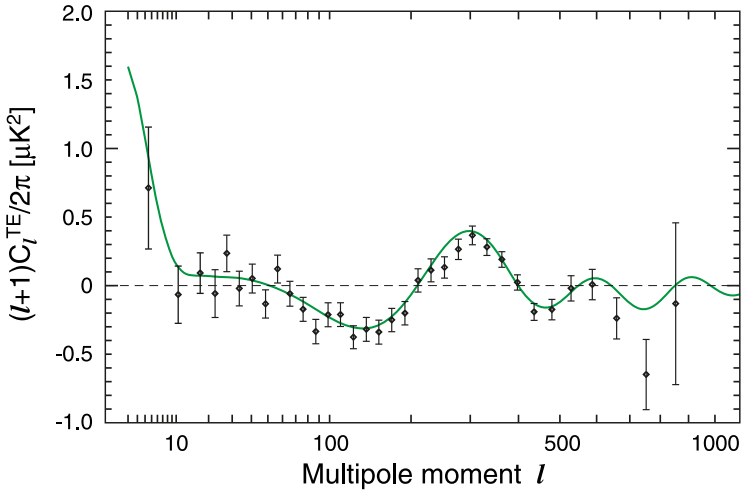

Figure 1.7: The angular power spectrum of CMB anisotropies-E-mode correlation. The red lines is the model best fit to data. Picture taken from [8].

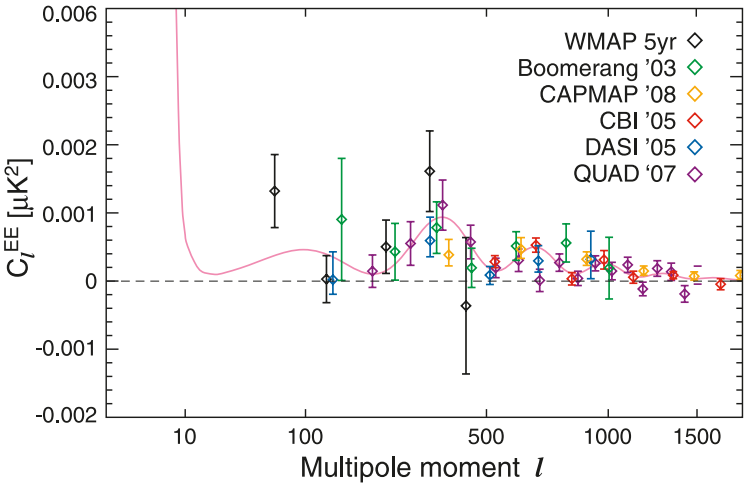

Figure 1.8: The angular power spectrum of CMB polarization E-modes. The red lines is the model best fit to data. Picture taken from [8].

scales (low ℓ) was not expected. This is connected to the so called universe reionization that occurred at redshifts $z \sim 20$.

When the universe got reionized the free electrons scattered CMB photons, polarizing them. This phenomenon has a signature at low multipoles, corresponding to the horizon scales at the time of reionization. The integrated optical depth for this phenomenon from WMAP data is $\tau_e = 0.087 \pm 0.017$

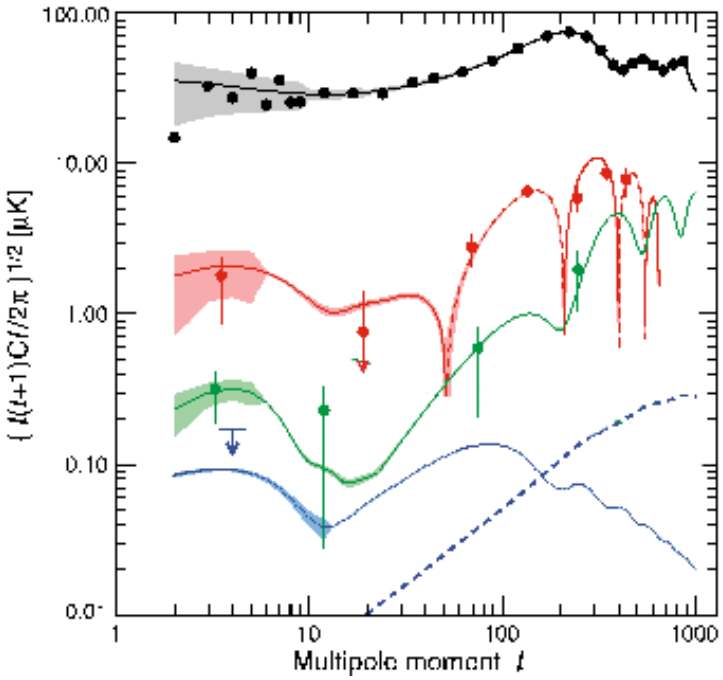

Figure 1.9: The angular power spectrum of CMB polarization modes. In red the model best fit to data for TE correlation. In green best fit model to data for the E mode power spectrum. In blue (solid line) the primordial B modes model. The blue dashed line represents B modes from gravitational lensing. For comparison the TT power spectrum is presented (black line). Picture adapted from [11].

at 95% CL [7].

In a wide variety of inflation scenarios, the amplitude of the tensor perturbations, which is usually characterized in terms of the tensor-to-scalar ratio r, is directly related to the energy scale of inflation. The measured spectrum of CMB temperature anisotropy constrain r to be less than about 0.2. This leads to a very faint signal that is not yet detectable with the instruments that up to now have investigated CMB polarization. By the way, according to WMAP data for some favorable inflationary models there is a clear indication that $r \sim 0.1$ [14].

The cosmological signal of B modes has to be searched for at scales lower than $\ell \sim 100$, since at scales higher than this the signal from primordial fluctuations is overridden by the ones produced by gravitational lensing of CMB photons [15].

Chapter 2

Light coherence

Light from a real physical source is never strictly monochromatic, since even the sharpest spectral line has a finite width. Moreover, a real source isn't a point source but has finite dimension consisting of many radiators. The disturbance produced by such a source may be expressed according to Fourier's theorem as a sum of monochromatic wave trains and essentially a monochromatic signal is just a single component of this representation.
In the context of monochromatic light, coherence is associated with the presence of phase correlations at two space-time locations. Usually coherence is related to the light ability to produce interference fringes, coherent light can interfere while incoherent light cannot interfere. This is reductive in the sense that for sure incoherent light cannot interfere but the absence of interference may not necessary mean that light is incoherent. Moreover, interference does not provide directly a quantitative measurement of light coherence. This is done with the visibility definition. Perfectly coherent light has 100% visibility while zero visibility implies incoherence. In the middle there is the regime of partially coherent light. Connected to the visibility concept there is the definition of the degree of coherence.

2.1 Complex coherence functions

The first order coherence between scalar fields at two space-time points (r_1, t_1) and (r_2, t_2) is defined via the first order complex coherence function [16]

$$\Gamma^{(1)}(r_1, t_1; r_2, t_2) = \langle E^*(r_1, t_1) E(r_2, t_2) \rangle. \tag{2.1}$$

If the points are spatially separated ($r_1 \neq r_2$) this coherence function is called complex mutual coherence function

$$\Gamma_{12} = \langle E_1^*(t_1) E_2(t_2) \rangle. \tag{2.2}$$

In this notation the subscripts refer to spatially separated locations. For spatially coincident points the first-order phase correlation refers to different times, so that the self coherence function

$$\Gamma_{11} = \langle E_1^*(t_1) E_1(t_2) \rangle \tag{2.3}$$

is found.

The coherence functions express correlations among fields at different times, anyway it is not important to know wether these correlation are sought at the same time or spatial position. It is convenient assuming that only the time delay $\tau = t_2 - t_1$ between relevant events is important, instead of exactly knowing the time scale origin. In this way it is assumed that the coherence functions have the same values for the same τ for all different absolute times the event happens.

Light fields satisfying this criterion are known as stationary fields and are produced by sources having steady-state conditions. In this case the self and mutual coherence functions can be written as

$$\Gamma_{11} = \langle E_1(t+\tau) E_1^*(t) \rangle, \tag{2.4}$$

$$\Gamma_{12} = \langle E_1(t+\tau) E_2^*(t) \rangle. \tag{2.5}$$

2.2 Complex degree of coherence

The complex degree of coherence $\gamma(\tau)$ is defined as the ratio of the complex coherence function $\Gamma(\tau)$ for a given time delay τ, with respect to its value at zero time delay so that for the self and mutual coherence function respectively one gets:

$$\gamma_{11}(\tau) = \frac{\Gamma_{11}(\tau)}{\Gamma_{11}(0)}, \tag{2.6}$$

$$\gamma_{12}(\tau) = \frac{\Gamma_{12}(\tau)}{\sqrt{\Gamma_{11}(0)}\sqrt{\Gamma_{22}(0)}}. \tag{2.7}$$

The complex degree of mutual coherence can be investigated in Young's double slit type interferometer (fig. 2.1), even neglecting diffraction due to the finite size of the source and of the slits. The resultant scalar field $E(P,t)$

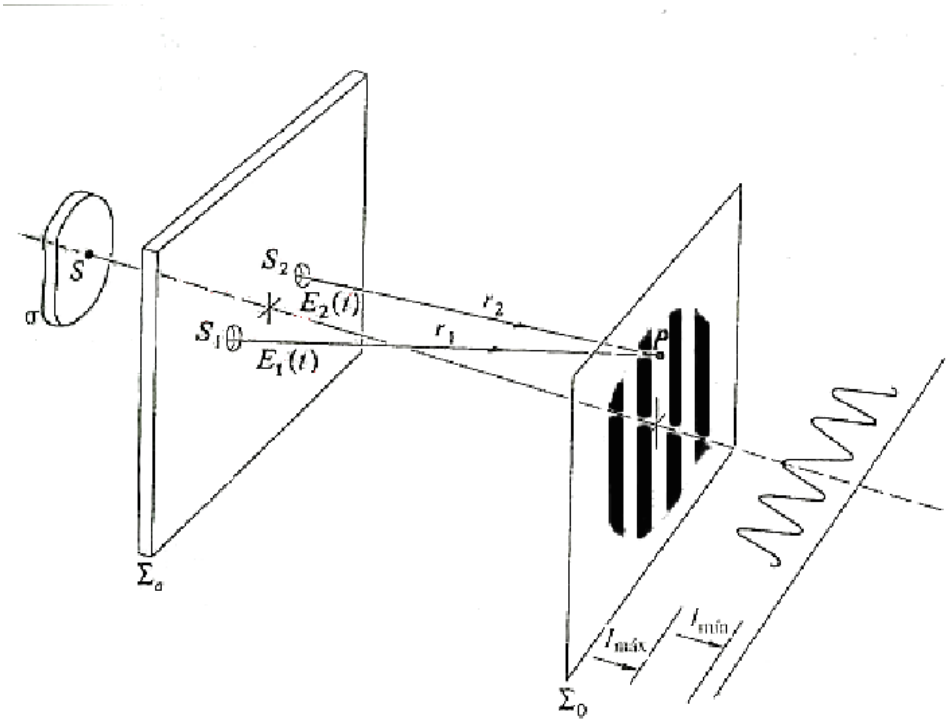

Figure 2.1: Scheme of the Young interference experiment (neglecting diffraction).

at a given point P of the observation plane is the superposition of the field arriving from the two slits, so that

$$I(P,\tau) \propto |E(P,t)|^2 = |E^{(1)}(P,t) + E^{(2)}(P,t)|^2. \tag{2.8}$$

Developing this calculation one gets:

$$I(P,\tau) \propto \langle \Big(E^{(1)}(P,t) + E^{(2)}(P,t)\Big) \Big(E^{(1)}(P,t) + E^{(2)}(P,t)\Big)^* \rangle \tag{2.9}$$

$$\propto I^{(1)}(P) + I^{(2)}(P) + \langle E^{(1)}(P,t) E^{(2)*}(P,t) \rangle \tag{2.10}$$

$$\propto I^{(1)}(P) + I^{(2)}(P) + Re\left(\langle E(\vec{r_1}, t+\tau) E^*(\vec{r_2}, t) \rangle\right) \tag{2.11}$$

$$\propto I^{(1)}(P) + I^{(2)}(P) + Re\left(\Gamma_{12}\right). \tag{2.12}$$

The last equation finally becomes for a point P in the screen plane [24]:

$$I(P,\tau) = I^{(1)}(P) + I^{(2)}(P) + 2\sqrt{I^{(1)}(P)I^{(2)}(P)}Re\left(\gamma_{12}(\tau)\right). \tag{2.13}$$

Eq. 2.13 is usually called the *general interference law* and for quasi monochromatic signals takes the form:

$$I(P,\tau) = I^{(1)}(P) + I^{(2)}(P) + 2|\gamma_{12}(\tau)|\sqrt{I^{(1)}(P)I^{(2)}(P)}\cos\left(\alpha(\tau) - 2\pi\bar{\nu}\tau\right), \tag{2.14}$$

where α is the argument of the complex degree of mutual coherence $\gamma_{12}(\tau)$ and $\bar{\nu}$ is the mean frequency of the quasi-monochromatic signal.
The mutual intensity function $\Gamma_{12}(0)$ is also called the complex spatial coherence function. Using Schwartz's inequality it can be proven that [16]

$$|\gamma_{12}(\tau)| \leq 1. \tag{2.15}$$

Inequality applies to partially coherent light, while equality holds for fully coherent light.
Finally, the visibility $V(\tau) = \dfrac{I_{max} - I_{min}}{I_{max} + I_{min}}$ of the Young's fringes equals

$$V(\tau) = 2\frac{\sqrt{I^{(1)}(P)I^{(2)}(P)}}{I^{(1)}(P) + I^{(2)}(P)}|\gamma_{12}(\tau)|, \tag{2.16}$$

which implies that for $I^{(1)}(P) = I^{(2)}(P)$ the visibility is the modulus of the complex degree of mutual coherence.
The phase $\alpha(\tau)$ is interpreted as some sort of constant phase difference between the field emanating from the slits that one has to take into account for quasi monochromatic light as with respect to perfectly monochromatic light.

The complex degree of self coherence can be investigated with the Michelson interferometer, showed in fig. 2.2. In this case one finds out that the output of the interferometer is

$$I(P,\tau) = \frac{1}{2}I(P_0)\left[1 + |\gamma_{11}(\tau)|\cos(\Phi(\tau) - 2\pi\bar{\nu}\tau)\right], \tag{2.17}$$

where $\Phi(\tau)$ is the complex degree of self coherence argument and $\bar{\nu}$ is the central frequency of partially coherent light.
It can be also shown that, in analogy with the mutual degree of coherence [24]

$$|\gamma_{11}(\tau)| \leq 1, \tag{2.18}$$

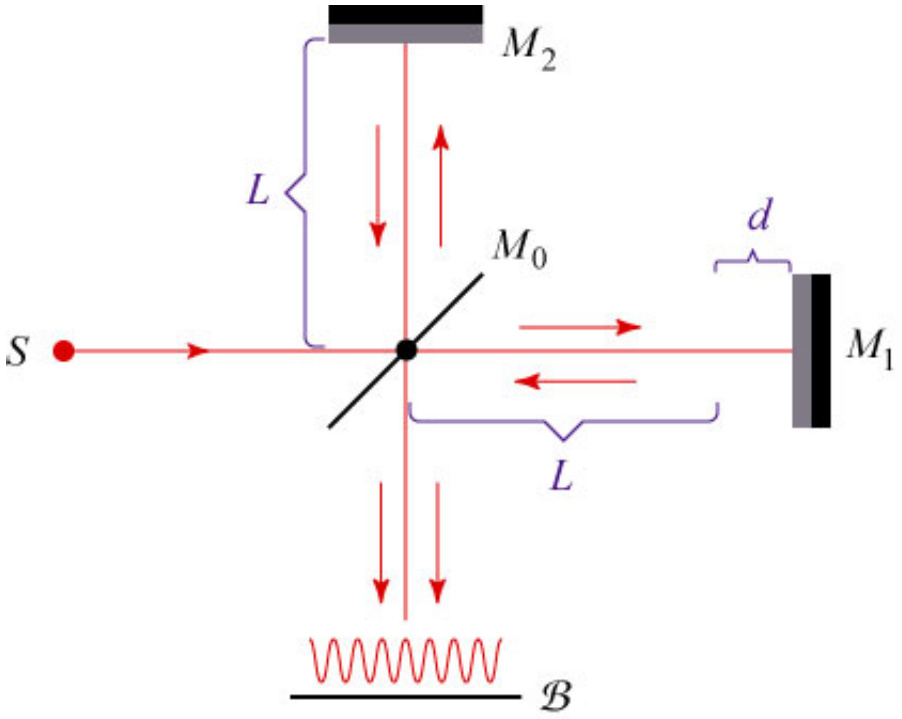

Figure 2.2: Scheme of the Michelson interferometer.

where equality holds for completely coherent light.
Finally the visibility of Michelson's fringes is:

$$V(\tau) = |\gamma_{11}(\tau)| \tag{2.19}$$

2.3 Coherence from an extended source

2.3.1 The Zernike-van Cittert theorem

This fundamental theorem allows us to obtain the mutual coherence function on a surface illuminated by a an extended incoherent quasi-monochromatic source. Consider a 2-dimensional incoherent quasi-monochromatic source σ and an observation plane xy, parallel to the source plane and separated from it by a distance R, supposed to be much larger than any dimension of the source. In addition let's suppose that R is much greater also with respect to the maximum distance among two point in the observation plane in consideration. This last point allows us to consider the time delay of radiation

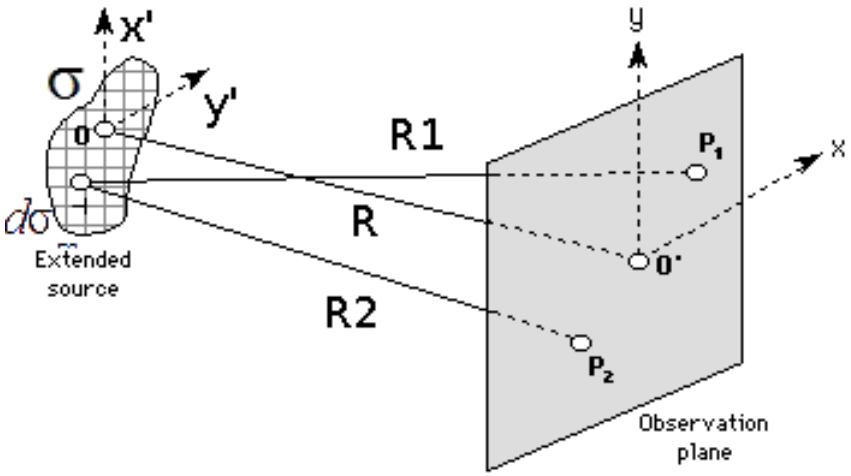

Figure 2.3: Observation of a extended incoherent source σ at point P1 and P2.

reaching points P_1 P_2 in the observation plane much smaller that the source coherence time [1].

Let's divide the source into infinitesimal area elements $d\sigma_m$, each smaller than the source wavelength λ. The complex (spatial) mutual coherence function can be obtained by summing up the contributions of each area element

$$\Gamma_{12}(P_1, P_2, \tau = 0) = \langle E(P_1, t)E^*(P_2, t)\rangle \tag{2.20}$$

$$= \sum_m \sum_{m'} \langle E_{m,1}(t)E^*_{m',2}(t)\rangle \tag{2.21}$$

$$= \sum_m \langle E_{m,1}(t)E^*_{m,2}(t)\rangle + \sum_m \sum_{m' \neq m} \langle E_{m,1}(t)E^*_{m',2}(t)\rangle, \tag{2.22}$$

where $E_{m,1}$ and $E_{m,2}$ are the scalar fields at point P_1 and P_2, respectively, due to the mth element of the source. According to this notation, having supposed the source to be incoherent, the double sum term in equation 2.22 (that represents the contributions for different area elements m, m') vanishes to zero so that:

$$\Gamma_{12}(P_1, P_2, \tau = 0) = \sum_m \langle E_{m,1}(t)E^*_{m,2}(t)\rangle. \tag{2.23}$$

$E_{m,1}$ and $E_{m,2}$ are the scalar fields at points P_1 and P_2 respectively, due to the mth element of the source. Relating these fields in the source plane

[1] Under these assumptions $\Gamma_{12}(\tau) = \Gamma_{12}(0)$.

and substituting the sum with an integral (in the limit of the area element $d\sigma_m \to 0$) one finally gets [24]

$$\gamma_{12}(P_1, P_2) = \frac{\Gamma_{12}}{\sqrt{I_1 I_2}} = \frac{\int\int_\sigma \frac{I(x',y')}{R_1 R_2} e^{-i2\pi\nu(R_2-R_1)/c} dx'dy'}{\sqrt{I_1 I_2}}, \tag{2.24}$$

where $I(x', y')$ is the intensity distribution over the source plane and R_1 and R_2 are respectively the distance of the image plane points P_1, P_2 from the source area element.

Thus the modulus of the spatial degree of mutual coherence between two points P_1, P_2 of the observation plane of an extended incoherent source equals the Fourier transform of the source intensity distribution.

2.3.2 Interferometric observations of CMB

The mutual coherence function describes the cross-correlation of the radiation field at two given points. This has the dimensions of power and can be easily measured using two element-interferometers.

In the case of an observation of CMB, that peaks in the millimeter wave region of the electromagnetic spectrum, its coherence can be measured using a radio interferometer, that is a system that is able to correlate electric fields collected by different antennas.

Consider the case of an interferometric observation of an extended source like the CMB: because of the Van Cittert - Zernike theorem the instrument would detect the fourier transform of the source intensity, called visibility. The visibility of an incoming radiation field $S(\vec{n})$ is [12]

$$V_S(\vec{u}) = \int S(\vec{n}) A(\vec{n}) e^{i2\pi\vec{u}\cdot\vec{n}} d\vec{n} \tag{2.25}$$

where $\vec{u} = \dfrac{b}{\lambda}$ is the baseline, defined as the vector separations between two antennas (b) in units of wavelength and $A(\vec{n})$ is the antenna beam pattern response in direction $\vec{n}$ [12]. The baseline $\vec{u}$ is also called spatial frequency. In the flat sky approximation[2] this can written as the convolution of the Fourier transform of the signal and of the beam:

$$V_S(\vec{u}) = \int \hat{S}(\vec{u}) \hat{A}(\vec{u} - \vec{v}) d\vec{v} \tag{2.26}$$

[2]This is true for small sky patches so that the spherical sky can be treated as flat. This is not realistically true for primordial B modes, that peak at angular scales of $\sim$ few degrees. Argument is treated in [10].

where the $\hat{hat}$ symbol denotes the Fourier transform operation.
In the case of the E and B modes of CMB polarization one gets [37]:

$$V_E(\vec{u}) = \int \hat{E}(\vec{u})\hat{A}(\vec{u}-\vec{v})d\vec{v} \tag{2.27}$$

$$V_B(\vec{u}) = \int \hat{B}(\vec{u})\hat{A}(\vec{u}-\vec{v})d\vec{v}. \tag{2.28}$$

The covariance matrix of the B visibilities contains the BB angular power spectrum

$$\langle V_B(\vec{u})V_B^*(\vec{u'})\rangle = \int \langle \hat{B(\vec{v})}\hat{B^*(\vec{v'})}\rangle \hat{A}(\vec{u}-\vec{v})\hat{A^*}(\vec{u'}-\vec{v'})d\vec{v}d\vec{v'} \tag{2.29}$$

$$= \delta(\vec{u}-\vec{u'}) \int C_\ell^{BB}(\vec{v})|\hat{A}(\vec{u}-\vec{v})|^2 d\vec{v}. \tag{2.30}$$

The angular power spectrum multipoles sampled are those corresponding to $\ell = 2\pi|\vec{u}|$.
This brief demonstration, expresses the fact that with CMB interferometry, the instrument output is directly the angular power spectrum instead of the usual sky map one gets with an imaging experiment. This is the same as stating that an interferometer looking at the CMB would directly measure samples of its angular power spectrum. This is something that comes directly from the fundamental Van Cittert-Zernike theorem.

2.4 Fourier Transform Spectroscopy

Consider the case of interference form polychromatic light, then the monochromatic general law of interference 2.13 would apply to each of the frequency that builds up the bandwidth to be observed.
For example the output of the Michelson interferometer for monochromatic light is

$$I(P,\tau) = \frac{1}{2}I(0)\left[1+\cos(2\pi\nu\tau\right], \tag{2.31}$$

and in presence of polychromatic light it becomes

$$I(\tau) = 4I(0)\int_0^\infty W(\nu)\left(1+\cos(2\pi\nu\tau\right)d\nu, \tag{2.32}$$

where $W(\nu)$ is the spectral density distribution of the source to be observed.
Recalling Euler's form of complex numbers eq. 2.32 can be rewritten so that

one gets

$$I(\tau) = I(0) + \Delta I(\tau) = I(0)\left(1 + \int_{-\infty}^{+\infty} W(\nu) e^{-i2\pi\nu\tau} d\nu\right). \tag{2.33}$$

The oscillatory part of this last equation represents the Fourier transform of the spectral density distribution of the source. Thus, the inverse Fourier transform of the oscillating part of the output intensity distribution of a Michelson (two beam) interferometer gives the spectral distribution of the source.

This is a standard spectroscopic technique, widely used in each branch of physics, and also CMB experiments adopted it. The most relevant FTS (Fourier Transform Spectrometer) devoted to CMB spectrum investigation is FIRAS (Far Infrared Absolute Spectrometer) that, onboard of the COBE satellite, proved the blackbody nature of the CMB spectrum. The optical

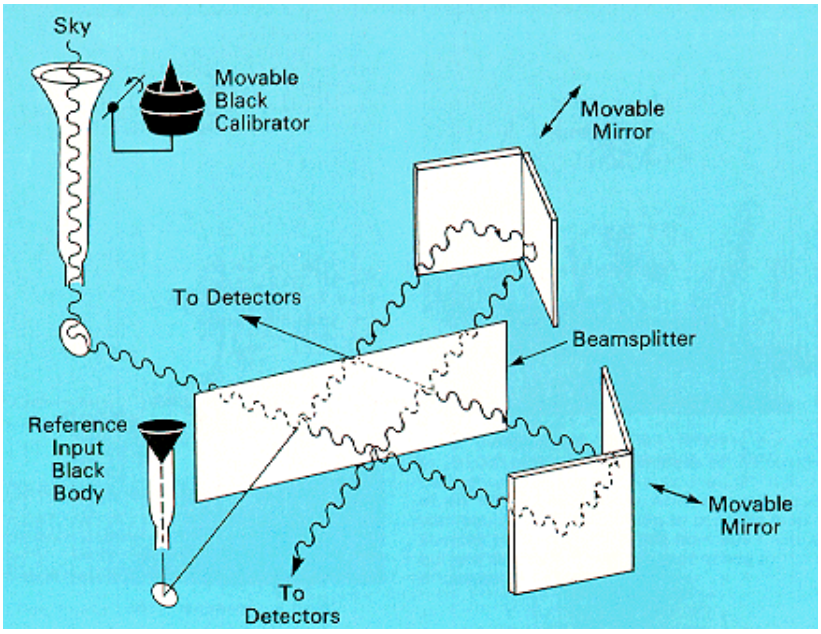

Figure 2.4: Optical layout of the FIRAS [2] instrument. The instrument measures the difference among sky intensity and the one of a variable thermal load.

layout [2], showed in figure, of this instrument is the classical Michelson one with two crucial differences:

- Beam division is performed with polarization splitting, that is beam-splitters are substituted by polarizers. This solution has been presented

for the first time by Martin and Puplett [19], who showed that at millimetric wavelengths this kind of beam-splitting technique is more efficient than amplitude division.

- The instrument has two inputs and operates in differential mode. One input is fed by sky radiation while the other is fed by a variable, high precision thermal load (black-body). With this scheme the instrument registers the intensity difference between the two inputs. By simply changing the thermal load temperature sky brightness is found with a zero signal level measurement.

Chapter 3

DIBo (Démonstrateur d'Interferometrie Bolometrique

3.1 Introduction

Together with site testing [20], the first step of the QUBIC (formerly BRaIn) collaboration towards the realization of a large bandwidth millimeter wave bolometric interferometer devoted to the study of CMB polarization [21] was the definition of a prototype to test the working principle of the final instrument.

DIBo is a single baseline interferometer made with commercial components used as a benchmark of the final instrument. Experiments involving DIBo have been done to test the application of the adding interferometry principle in the full WR10 waveguide band. Moreover, an experimental method to investigate the instrument performances has been defined and validated. Some measurements were done coupling the instrument with a 4K bolometer as a detector.

The first objective is then simply to detect interference fringes at the instrument output: a further analysis of these fringes should then help in the description of the instrument performances.

The second but not less important step aims to define an experimental setup and procedure that is able to fully characterize each element of the instrument and the whole assembled system. In this way a procedure able to

describe the real performances of the system is completely developed.This is very important in the framework of having a large instrument made with hundreds of elements that just in principle are equal and whose differences can introduce spurious effects in the measurements.
Finally, measurements done with the bolometer provide the first step toward the detection of interference fringes in a large (20%) bandwidth.

3.2 DIBo working principle

Two orthogonal components of the incoming electric field are conditioned through two symmetrical parallel chains, along relative phase shift is ideally just that one fixed by a couple of programmable phase shifters $\Delta\alpha = \alpha_2 - \alpha_1$. The DIBo principle is to collect radiation with two identical corrugated horns

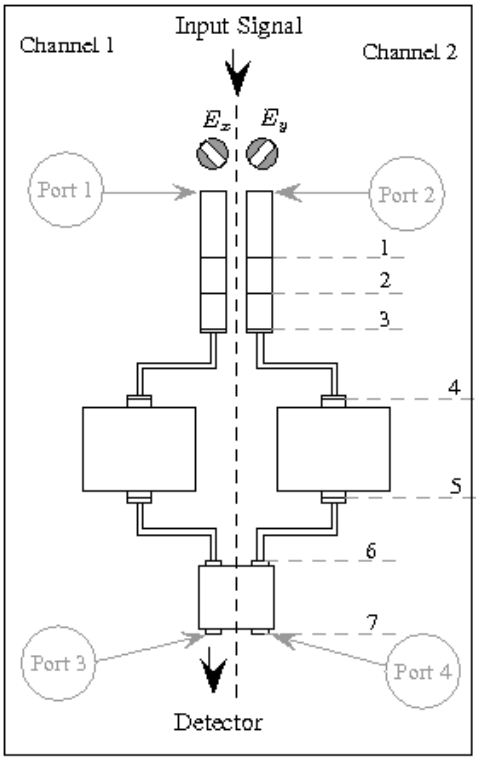

Figure 3.1: DIBo scheme viewed from top: (1) Input Horns, (2) Circular to Rectangular Transitions, (3) ±45° Twists, (4) Bends, (5) Phase Shifters, (6) Bends, (7) Hybrid Ring Coupler

(that constitute the interferometer baseline) that feed two separate ideally

equal arms. The horns polarization axis are $\pm 45°$ twisted with respect to the vertical axis, so that the angle between them is 90°.
The horns are connected to a couple of $\pm 45°$ twists (fig. 3.1) with a circular to rectangular transitions whose aim is to realign polarizations in order to combine signals in the two arms. A couple of bends then leads signals to phase shifters.
Phase shifters are the elements that introduce an optical path difference between the two arms. This phase shift is required in order to observe an interferogram without introducing a geometrical optical path difference (for example rotating the source). They are a couple of QUINNSTAR programmable phase shifter that can introduce a phase shift up to one wavelength (360°).
The two signals are combined in the 90° hybrid ring, where the superposition of the in phase and phase quadrature waves takes place.
After detection the output is:

$$R \propto I + V \cos \Delta\alpha - U \sin \Delta\alpha, \tag{3.1}$$

where I, U and V are the usual Stokes' parameters [12].

3.3 Single component measurements

Each DIBo component has been measured with a AGILENT 8510 MVNA in the whole WR10 (75 GHz-110 GHz) band, in order to find out the real frequency behavior of each part that builds up the instrument.
The S matrix [22] of each microwave component has been obtained before assembling the full instrument.
The MVNA had been operated in the 75-110 GHz waveguide band, sampled with 801 frequency points that are the maximum resolution achievable with the instrument. The MVNA calibration accuracy is around 0.005 dB.
The instrument was calibrated with the standard full two ports calibration procedure using an AGILENT WR10 standard calibration kit.

3.3.1 Phase Shifters

The devices that deserve the most careful characterization are the phase shifters (PSs) since they are the key feature of the instrument and the most complicated device that build it. A picture of the experimental layout for the phase shifters MVNA measurements can be seen in appendix A.
Commercial phase shifters like the ones used for DIBo usually have a nearly ideal behavior when they are operated close their nominal operational frequency while unwanted effects appear when working at other frequencies.
The first measurements on phase shifters has been done to check the uniformity of the phase shift[1] with respect to frequency.
To do this phase shift has been set to 0°: this measure has been used as the zero electrical length reference. A fixed phase shift has then been inserted among the two interferometer branches and measured at each of the 801 frequency points inside the WR10 band. Good agreement is found. For example, setting the phase shift to 180° the average phase shift in the 85 GHz-95 GHz sub-band is $178.5° \pm 1.5°$, while the overall dispersion in the complete band is around 2 degrees, as showed in fig 3.2. These results underline that the programmable phase shift is frequency dependant, anyway the optical path difference related to such a dispersion is around $\sim \frac{\lambda}{180}$ which is negligible.
A second measurement on the phase shifter was a complete study of their transmission function. The full S parameters matrix has been measured.
S_{21} and S_{12} measurements showed unwanted amplitude modulation (fig. 3.4) of the transmitted signal. This modulation depends both on frequency and the phase shift introduced (fig. 3.3). As said, this effect increases when operating close to the band borders.
The aim of this measurement is, apart from characterizing the phase shifter, to try to learn its behavior in order to better recognize it inside the full instrument output. Moreover, far from the central frequency the PSs transmission is as low as $\sim$ -20 dB.

[1] The phase shift is introduced by setting the desired value on the programmable phase shifter.

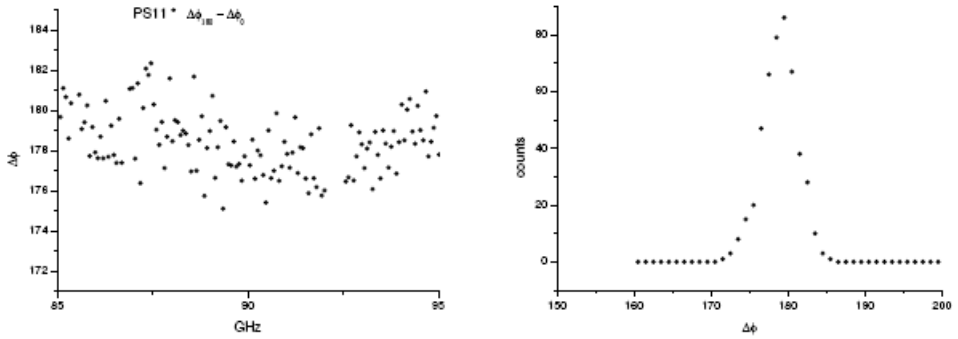

Figure 3.2: DIBo phase shifters phase stability. Left panel: measured phase shift as a function of frequency when the programmable phase shift is set to 180°. right panel: measurements histogram.

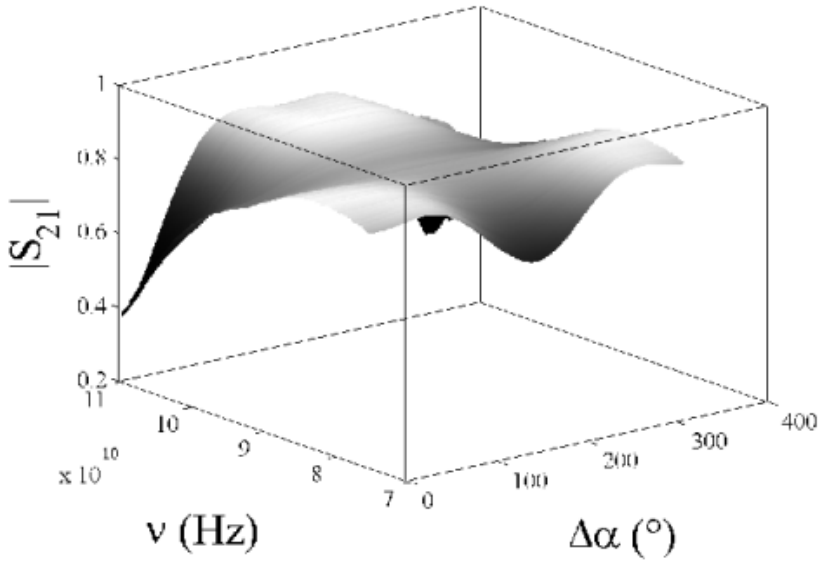

Figure 3.3: DIBo phase shifter power transmission as a function of frequency and phase shift.

3.3.2 Hybrid ring

Tests on the hybrid ring were done to investigate its transmission, the frequency dependance of the 90° phase shift it introduces in one of its paths and its inputs isolation. A picture of the hybrid ring MVNA measurements can be seen in appendix A.

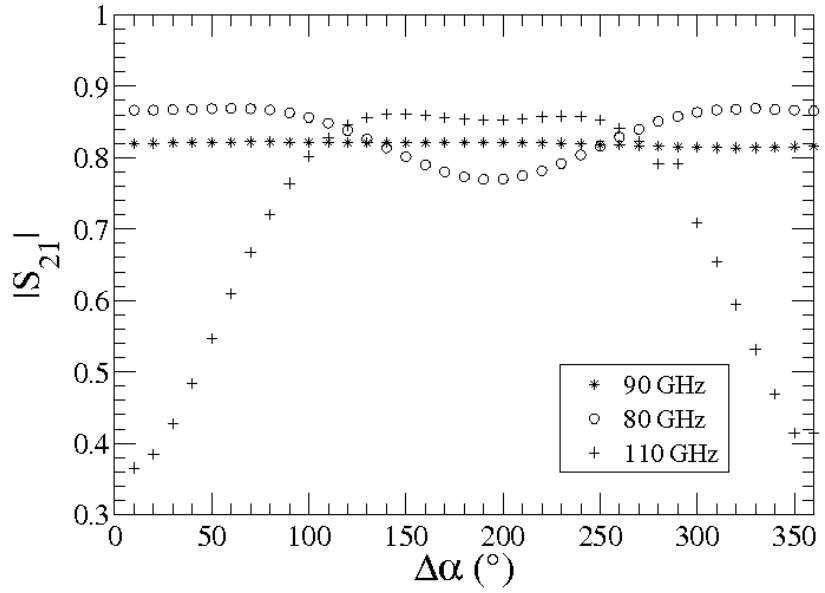

Figure 3.4: DIBo phase shifters power transmission at 80 GHz (circles), 90 GHz (asterisks) and 110 GHz (crosses) as a function of the phase shift.

The overall transmission is measured to be around ~ 5 dB, as declared by the firm data sheet. Fig 3.5 shows phase shift frequency $\Delta\varphi$ dependance.

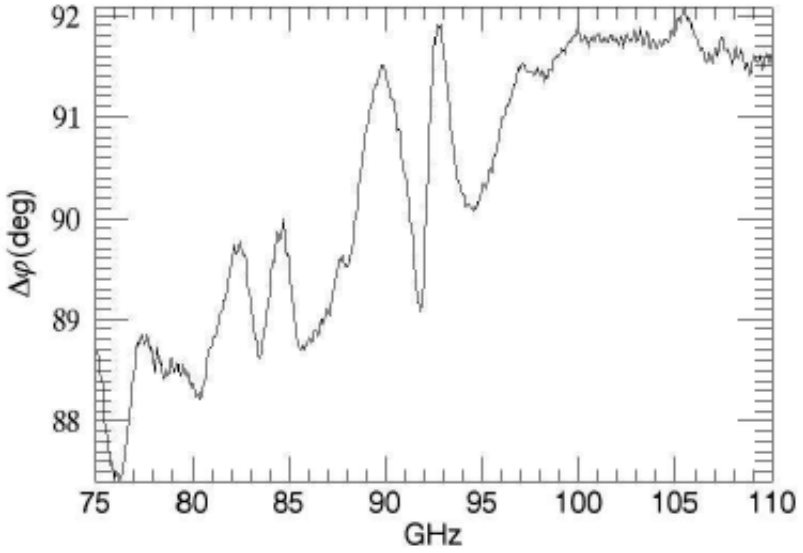

Figure 3.5: Hybrid ring phase shift as a function of frequency.

The discrepancy in the full band is roughly $\sim 2°$. This effect can be an issue when dealing with large bandwidth measurements since, being frequency dependent, it induces bandwidth smearing [12].
The last set of measurements was held to quantify the hybrid isolation, that is what part of signal is transmitted between the two inputs. This a very important aspect, since a coupling between the two inputs would lead to a polarization leakage [23] from one Stokes' parameter to another.
The measurement reported a coupling at a level -25 dB and was done connecting the VNA sources to the hybrid inputs, while the two outputs were terminated with two standard waveguide loads.

3.4 Full arms measurements

After the single component characterization, measurements in the WR10 band were held on a single DIBo complete arm. These measurements aim to give the full instrument power transmission function as a function of the phase shift and frequency (fig 3.6). A picture of the MVNA full arm measurements is shown in appendix A.
Measurements have been done on each of the two branches of the interferometer, with one VNA port connected to the twist placed just after the horn and the second port connected to one of the two hybrid ring outputs while the other output was terminated with a standard waveguide load.

The overall instrument transmission is low with a maximum of -7 dB in the central part of the band, rapidly decreasing to -20dB going towards the band borders.
Moreover, clear signature of the phase shifter amplitude modulation can be seen. This effect is more evident in the tails of the band.
This is because the PSs are optimized to work in a 6 GHz band centered at 90 GHz. The overall transmission function does depend also on the phase shift (fig. 3.6).

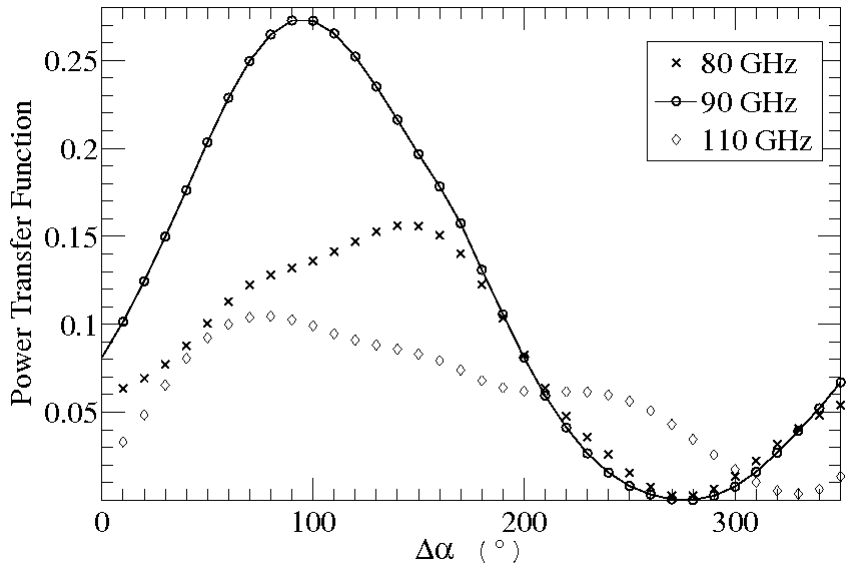

Figure 3.6: DIBo full chain power transmission at 80 GHz (crosses), 90 GHz (circles) and 110 GHz (diamonds) as a function of the programmable phase shift.

3.5 Bolometric measurements

Bolometric measurements were held using as source the head of a ABmm MVNA. Only monochromatic measurements were done. Source signal was modulated with a chopper. Detection was achieved with a 4K semiconductor bolometer read with a lock-in amplifier.

The optical path difference required to produce fringes was inserted by simply rotating the instrument with respect to the source by an angle φ. The baseline was set to 20.5 cm, while the source is connected to ah horn radiating a beam with an FWHM of 10° at 90 GHz. The first measurement done with the bolometer was the simple fringe detection. To do this the inclination with the source φ had been fixed, while varying the phase shift $\Delta\alpha$ with PSs. A sinusoidal response with the expected period has been detected. Moreover, as a cross check that it's produced by interference one of the two DIBo horns has been obscured and the interference vanished.

The angular response of the interferometer had been measured by rotating the source by an angle φ. In this way the convolution of the primary horn beam with the interference fringes it's being detected. The power response

has the form

$$P(\beta) \propto B^2 \left[1 + \sin\left(2\pi u \sin(\varphi - \varphi_0) + \theta\right)\right], \tag{3.2}$$

where $u = D/\lambda$ is the baseline (D is the DIBo horn separation), $B(\varphi)$ is the primary beam profile, φ_0 is an offset angle for the source rotation and θ is an angle that takes into account the phase shift $\Delta\alpha$ and other possible offsets of the system. These offsets can be for example due to horn misalignments but also to asymmetries in the interferometer arms that introduce an extra optical path difference which is frequency dependent. Other sources of θ could be the non ideal behavior of some of the instrument components, mainly the hybrid ring and the PSs. Figs. 3.7, 3.8 show as an example the

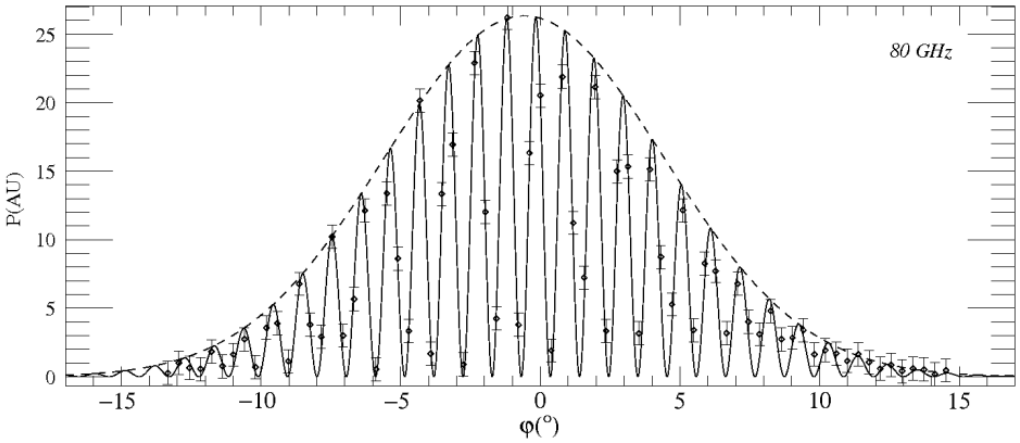

Figure 3.7: DIBo fringes power pattern at 80 GHz obtained by rotating the source by and angle φ and detected by a bolometer placed after the hybrid ring.

power detected by DIBo at 80 GHz and 90 GHz respectively, when rotating the source by an angle φ: solid lines are the best fit for the interference fringes while the dashed one is the best fit for the DIBo primary beam profile. The best fit ($\chi^2/dof \sim 1.99$, $\chi^2/dof \sim 1.75$ respectively at 80 GHz and 90 GHz) parameters to measured data are shown in table 3.1 and indicate that what was observed was nothing more than interference fringes produced by the source rotation convolved with the primary horn beam pattern, as expected. It can be somewhat said that in this case the DIBo horns act as the slits

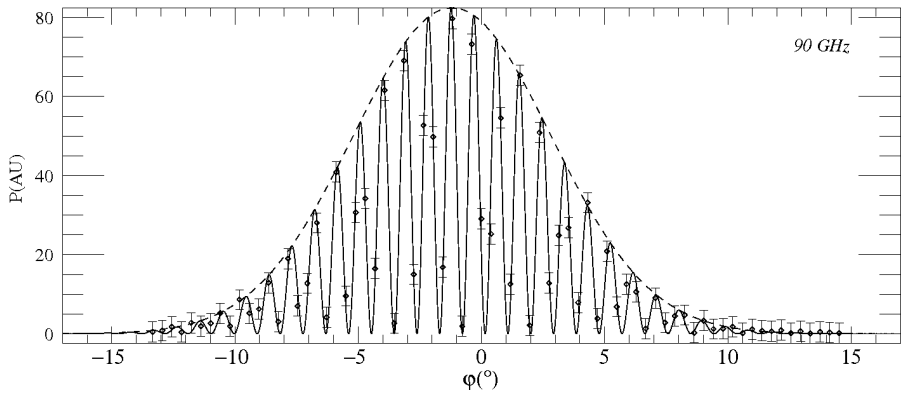

Figure 3.8: DIBo fringes power pattern at 90 GHz obtained by rotating the source by and angle φ and detected by a bolometer placed after the hybrid ring.

of the Young's experiment and the fringes produced by the interference of light fields emanating from them is convolved with their diffraction pattern.

ν (GHz)	B (ADU)	φ_0 (°)	σ (°)	u	θ (°)
80	13.2 ±0.02	-0.58±0.08	5.01±0.08	54.07±0.05	305.±27
90	41.2 ±0.06	-1.1±0.07	4.02±0.07	62.1±0.07	107±26

Table 3.1: Best fit parameters for eq. 3.2 for the bolometric measurements taken at 80 GHz and 90 GHz frequency.

3.6 Large bandwidth Measurements

3.6.1 Experimental setup

A frequency sweeper FARRAN BWO-10 is used as a source, operating both in Continuous Wave (CW) mode and in sweep mode. In the first case, a quasi-monochromatic signal is produced at a fixed frequency. In the second case, a frequency sweep across a chosen bandwidth (87-93 GHz, or 75-110 GHz in our case) is performed in 10 ms. The signals, collected by the two antennas of the interferometer, after phase shifting are combined in the hybrid, and then detected with a power sensor HP W8486A, placed on one of the two outputs of the combiner (the second one is closed on a matched load). Then, the analog output of the power meter HP 438A feeds a single

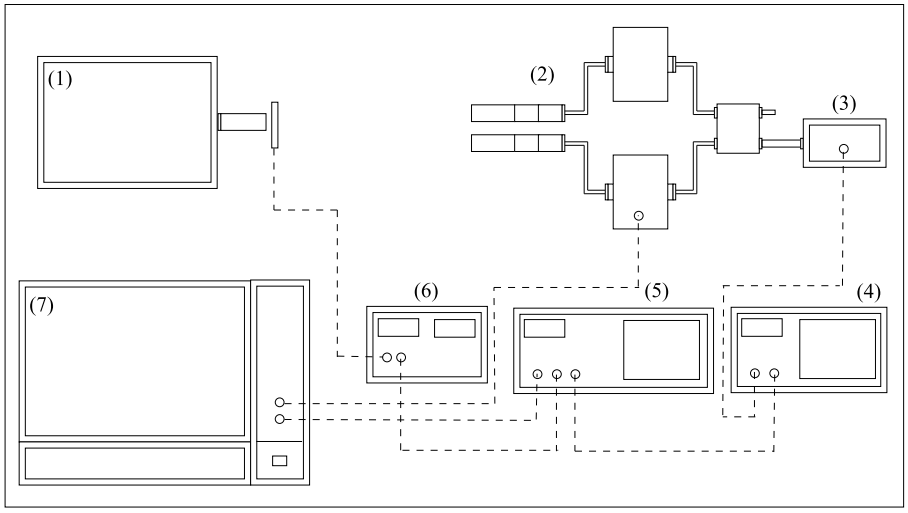

Figure 3.9: Layout of the instrumental setup used for large band measurements. (1) Farran BWO-10 power generator, (2) DIBo under test, (3) HP W8486A power sensor, (4) HP 438 A power meter, (5) EG&G lock-in amplifier, (6) Chopper controller, (7) Computer for PSs programming and data acquisition.

channel lock-in amplifier EG&G 5209. The external reference of the lock-in is the driving signal coming from the control unit of the chopper, which modulates the source signal at 10 Hz. The basic idea behind this set-up is to replace an artificial black body with a fast frequency sweep across all the frequency band. If the sweep is much faster than the response time of the power meter (as in our case, since the typical time constant of the power sensor is τ =35 ms), this system can mimic a broad-band source. Of course the best solution would be an artificial black-body, but commercial power meters operating at room temperature are not sensitive enough to detect a 300-500 K signal. A picture of this layout is presented in appendix A. This set-up can be useful for the characterization of millimeter-wave systems whenever cryogenic front-ends are not available. Even if the signal of the sweeper is strong enough to be directly detected by the power sensor, the use of a lock-in has been preferred, in order to operate always with a favorable signal-to-noise ratio, even when the source oscillator was used at power levels below the 25% of the peak power available. In fact below this threshold the sweeper output power vs frequency is practically flat.

3.6.2 Analysis

The measurements done with this setup represent the visibility of the signal emitted by the generator and detected by DIBo, it is then straightforward to recover from them the complex degree of coherence.
In principle the phase shifters introduce a delay in the lines that is frequency independent at least in the central 87 GHz-93 GHz central sub-band, so that the degree of coherence should be constant with phase shift and equal 1. This is because the optical path difference should be the same at each frequency, leading to the same fringe pattern at each frequency, provided the power carried at each frequency is the same.
In reality there are various reasons to suppose that the measured degree of coherence is less than one, among them for example the fact that there could be a small ($\sim$ 1mm) asymmetry in the optical path of one interferometer arm with respect to the other. This asymmetry would in fact introduce an optical path difference (phase shift) that is frequency dependent, and the effect on large band measurements is a reduction of the amplitude of the interference fringes. A reduction of the complex degree of coherence is also expected because it has been shown that the programmable phase shift is frequency dependent (fig 3.2) in the full WR10 band. There are well known aspects of large band interferometry grouped in the so called bandwidth smearing [12] phenomenon.

Bandwidth smearing

Suppose to measure the real and imaginary part of the interference field formed by two waves having equivalent amplitude A_0 and wavenumber σ: then for an optical path difference δ we have:

$$I_{\pm}(\delta, \sigma) = 2A_0^2 \left[1 \pm \cos(2\pi\sigma\delta)\right] \tag{3.3}$$

When performing an interference measurement, signals are always distributed in a given band of frequencies $\Delta\sigma$; the ideal monochromatic case is recovered considering $\Delta\sigma$ small.
To obtain the complete interference pattern the monochromatic response must be integrated over ν.

Suppose now that the signal is defined in a band $\Delta\sigma = \sigma_2 - \sigma_1$, then the intensity is

$$I(\delta) \sim \int_{\sigma_1}^{\sigma_2} I(\delta, \sigma) d\sigma, \tag{3.4}$$

where $I(\delta, \sigma)$ is the monochromatic response of the interferometer written in a form like the one in eq 3.3. The frequency integration gives the result

$$\begin{aligned} I(\delta) &= 2A_0^2 \left[\Delta\sigma \pm \int_{\sigma_1}^{\sigma_2} \cos(2\pi\sigma\delta) d\sigma \right] & (3.5) \\ &= 2A_0^2 \Delta\sigma \left[1 \pm \frac{1}{2\pi\delta\Delta\sigma} \left(\sin(2\pi\sigma_1\delta) - \sin(2\pi\sigma_2\delta) \right) \right]. & (3.6) \end{aligned}$$

This last equation can be manipulated using prostapheresis formulas so that

$$I_{\pm}(\delta) = \frac{I_0}{2} \left[1 \pm \cos(\pi\delta(\sigma_1 + \sigma_2)) \frac{\sin(\pi\delta\Delta\sigma)}{\pi\delta\Delta\sigma} \right]. \tag{3.7}$$

In the real world monochromatic signals do not exist and what happens is that the usual monochromatic frequency response of the interferometer is multiplied by a *sinc* ($\sin x/x$) function that depends upon both the phase shift δ (optical path difference) and on the bandwidth $\Delta\sigma$ considered. Specifically, fixing the system bandwidth, the greater δ the narrower the *sinc* function and the higher the fringes damping. This express the fact that the superposition of waves with different wavelengths occurs with an efficiency that is less than one, the greater the wavelength difference, the smaller the efficiency.

Moreover, the greater the phase difference, the smaller the efficiency because the optical path difference approaches the coherence length [24] $l_c \sim \dfrac{\bar{\lambda}^2}{\Delta\lambda}$ of the system. Fig 3.10 shows the output of exit 3 of the hybrid ring: a small compression of the signal can be seen as the bandwidth increases.

The degree of coherence γ can be computed using the visibility definition, so that

$$|\gamma| = \frac{I_{max} - I_{min}}{I_{max} + I_{min}}. \tag{3.8}$$

Results of this calculation are showed in the following table 3.2. In this table errors are computed with the error propagation formula starting from eq 3.8; only the statistical error on the measurements has been considered.

For the narrow (6 GHz, 90 GHz centered) band there is no evidence for a complex degree of coherence significantly less than one, but considering

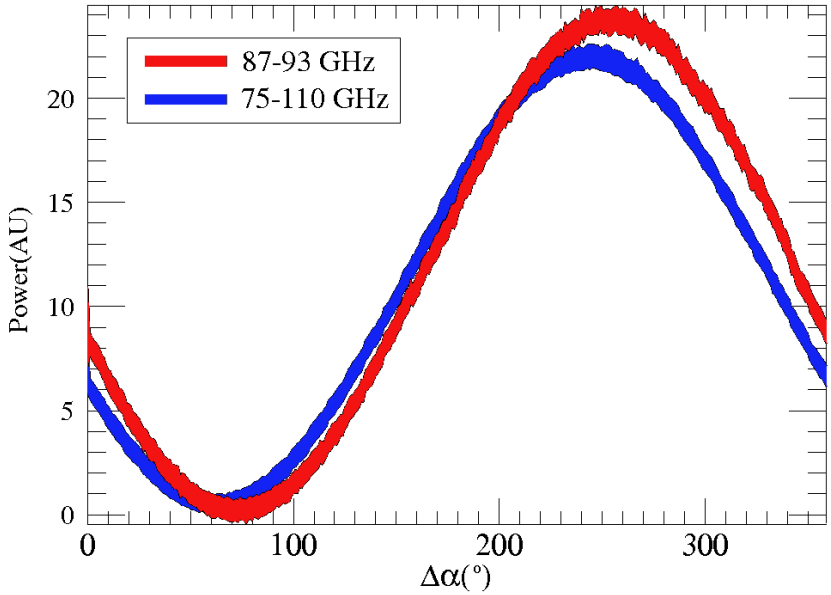

Figure 3.10: Power detected by the HP sensor as a function of the programmable phase shift when connected to one of the hybrid outputs. The red line is for a signal radiated by the FARRAN generator in the 87-93 GHz bandwidth while the blue one is for 75-110 GHz bandwidth.

Band	$\|\gamma\|$
6 GHz	0.99±0.04
WR10	0.96±0.04

Table 3.2: Modulus of the complex degree of coherence for signals measured by the power meter at output 3 of the DIBo hybrid ring for the 6 GHz and full WR10 bandwidths signals.

the case of the full WR10 bandwidth there is an indication of the presence of a small amount of bandwidth smearing. The interpretation of this effect is the frequency dependance of the phase shifter. An asymmetry between the electrical length od DIBo arms cannot explain this compression because in this latter case the effect would still depend upon the frequency, but it should also be constant while changing the phase shift, which is in contrast with observation.

Comparison with VNA measurements

Even if VNA measurements are substantially monochromatic ($\sim$ 40 MHz wide), they can be combined to produce a sort of expected frequency integrated system response. This has been done numerically integrating the monochromatic transmission function measured with the full chain VNA measurements.
In this way a sort of simulated system response has been produced in order to be compared to the measured one.
Anyway the comparison is not straightforward since the transmission function is normalized, while the measured data are not. The first problem is to look for a normalization for the large bandwidth measurements.
Moreover, the numerical routine used for the frequency integration changes the normalization of the transmission function.
The normalizing factor for the measured data has been computed using a CW measurement with the large bandwidth experimental setup. In this way a 90 GHz monochromatic signal was detected by the power meter at the interferometer output. This measurement has been compared with the 90 GHz transmission function measured with the VNA in order to extract the normalizing factor for the large band signal, in the hypothesis that this factor is constant over all the WR10 band.
Formally with the CW measure one detects a power $P(90GHz, \Delta\alpha)$:

$$P(90GHz, \Delta\alpha) = P_{inc}T(90GHz, \Delta\alpha), \tag{3.9}$$

which is a function of the power transmission function of the system transmission $T(90GHz, \Delta\alpha)$ (measured with the VNA) and of the incoming power P_{inc} radiated by the generator. Having the CW measure $P(90GHz, \Delta\alpha)$ one can solve this last equation for P_{inc}. It has to be stressed again that with this procedure large band measurements are normalized only if there is no reason to suppose that P_{inc} is frequency dependent[2].
In order to compare the large bandwidth measurements with the syntheti-

[2] Although it was explained in the experimental setup section that the power delivered by the sweeper is flat with frequency, the are reasons to suppose that there a frequency dependence can arise due to the optical coupling (which is surely frequency dependant) between the generator and DIBo.

cally reconstructed ones, the numerically integrated response must be normalized again. This has been done numerically integrating the frequency response of an ideal monochromatic inteferometer[3] of which the analytical form is know to be like 3.6. Again, comparing the correlated parts of eq. 3.6 and of the numerically integrated ideal response the factor A_0 can be extracted.

This factor is finally applied to the numerical integration of the real instrument transmission (measured with the VNA). Figures 3.11, 3.12 show the

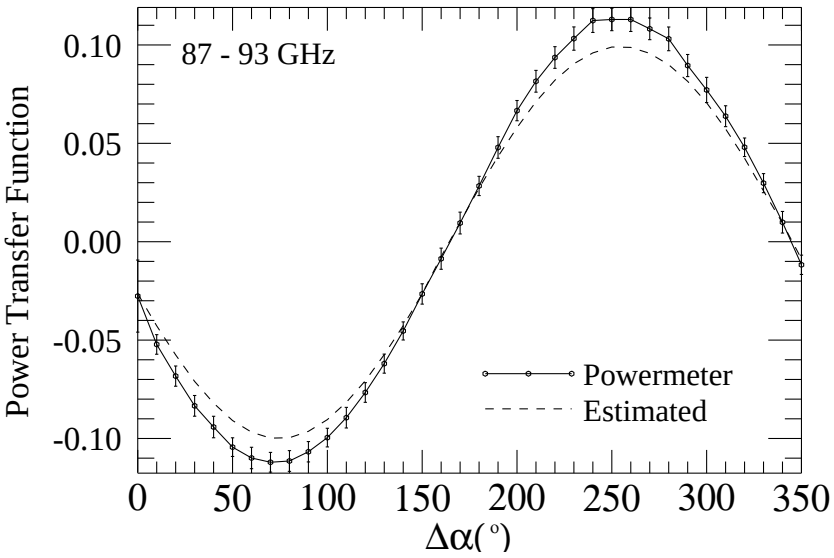

Figure 3.11: Comparison between the 87-93 GHz bandwidth power transmission functions as function of the programmable phase shift, derived from large band measurements (solid line with error bars) and the synthetic one derived numerically integrating in the same band full chain VNA measurements (dashed line).

comparison of the simulated and measured band response of the interferometer for both 6 GHz band and full WR10 cases. Error bars are computed with errors propagation formula starting from equation 3.9, where errors on VNA measurements have been considered to be negligible with respect to the large band measured errors since the accuracy level of the VNA is at least 10^{-2} dB.

The discrepancy present between simulated and measured data appears to

[3] $T_{ideal} = 1 - 2\sin(\frac{2\pi\delta}{\lambda} + \Delta\alpha)$

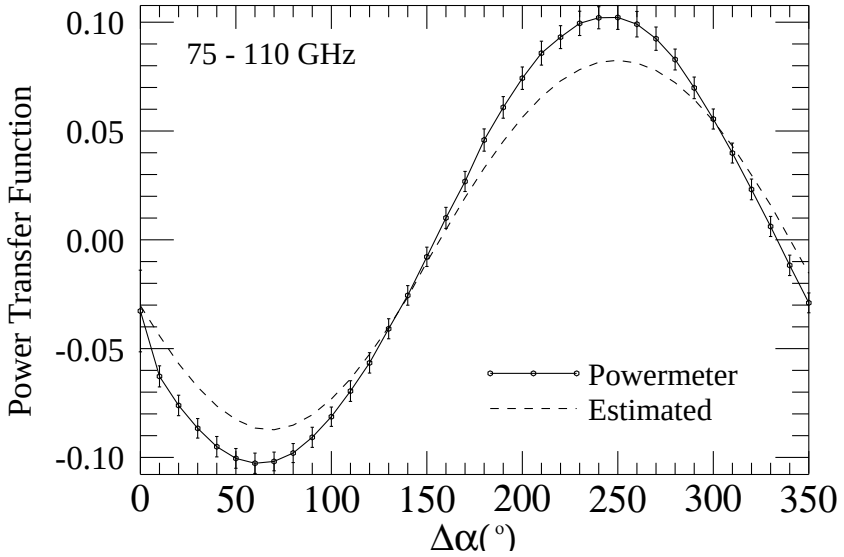

Figure 3.12: Comparison between the 75-110 GHz bandwidth power transmission function,as function of the programmable phase shift, derived from large band measurements (solid line with error bars) and the synthetic one derived numerically integrating in the same band full chain VNA measurements (dashed line).

be an artifact due to the normalizing technique. This idea is supported by the fact that the degree of coherence (which is, being a relative quantity, independent from scale factors) of the simulated patterns are $|\gamma^{sim}_{WR10}|$=0.94, $|\gamma^{sim}_{6GHz}|$=0.98, that are in agreement with the measurement reported in table 3.2. This means that the discrepancy is just a scale factor that has no frequency or phase dependence.

Systematic effects

Large bandwidth measurements were done in order also to look for the imprint of the systematic effects seen in the VNA measurements on the final output of the instrument.

Unfortunately this cannot be done with this data: there are at least a couple of reasons to explain it. First of all the error bars on the measurements are at few percent level[4] of the measured signal. Even if single component VNA measurements showed large systematics in some cases (phase shifter, hybrid

[4]This is just the statistical fluctuation of signals, computed from the raw data recorded by the DAQ.

ring) none of them is so high to be seen with this large error bars. This is enhanced by the low transmission of the instrument that reduces the signal level in the output.
The second main reason for the fail in the systematic effects detection is DIBo low transmission. Most of systematic effects comes up in the tails of the observational bandwidth (for example amplitude modulation by PSs), where transmission is really low ($\sim$-15dB$\div$20dB). For this reason the net contribution of signal from these tails to the mean response produced by the frequency integration of the signal in these tails is negligible. This means that the equivalent bandwidth is much narrower than the ideal WR10 band because of the low transmission of the instrument.
This explain also the fact that the output is similar to the one that can be obtained considering an ideal square frequency band (the *sinc* function is the Fourier transform of the square form.) even if it has been showed by VNA measurements that the bandpass is far from being ideal (rectangular).

Chapter 4

Design of the QUBIC Fizeau combiner

In the framework of the CMB experiments devoted to the study of the polarization B-modes, QUBIC [21] is an original one, orthogonal to the others proposed and developed by the scientific community.
The key concept of QUBIC is the use of bolometric interferometry as a detection scheme, combining the idea of interferometry (for a direct observation the CMB angular power spectrum as for example done in the DASI [25] and CBI [26] experiments) and the sensitivity of large band incoherent bolometer detectors [27].
QUBIC community was born by the mergeer of the BRaIn [20] and MBI [28] experiment communities in order to combine efforts in reaching the goal of the B modes detection.

4.1 Why a bolometric interferometer?

Up to now CMB polarization experiments have been based on two different detection techniques: imaging and interferometry. Imagers (like QUAD [30] for example) observe the CMB temperature field and produce a fluctuation map taking differences from different detectors; the power spectrum is recovered Fourier transforming this map.
This scheme suffers from various systematic effects, and the control of systematic effects is a crucial point of an experiment targeting a weak signal as the B-modes [23]. The telescope, used to achieve the angular resolution

required to observe the multipoles of interest, is a source of systematics like ground pickup from sidelobes of the antenna beam pattern [12] and beam mismatch.
Moreover, performing signal differencing from different detectors poses the problem of the intercalibration of different detectors. On the other hand, these instruments usually adopt very sensitive detectors (for example large bandwidth bolometers) that guarantee high sensitivity for the whole instrument.
Heterodyne interferometers have produced the first detection od CMB polarization [31]. The observation of CMB with an interferometer does not require the use of optics, since the angular resolution depends only upon the baseline length [12].
An interferometer measures the Fourier transform of the sky signal, directly producing the power spectrum from the fringes visibility. By the way heterodyne system are intrinsically narrow band and therefore not as sensitive as instruments using large band detectors (bolometers). The QUBIC collaboration decided to investigate the performances of a bolometric interferometer, that is of an instrument that combines the interferometric technique with large band incoherent (i.e. not able to directly measure the signal phase) detectors (bolometers).
The use of large band detectors in detecting interference fringes poses the problem of bandwidth smearing [12]. Since polychromatic light has a degree of coherence that can be significantly less than 1, this fact can lead to a loss of sensitivity of the instrument.
The collaboration carefully investigated the sensitivity of such an instrument and came to some conclusions.

- The sensitivity of a bolometric interferometer strongly depends upon the phase shift scheme adopted to recover the visibilities in the detector plane. It has been shown [37] that if the phase sequences are adjusted so that equivalent baselines (see fig. 4.1) [1] are all in phase and coherently summed (that is their relative phase is the same), then the interferometer sensitivity is maximized since statistical fluctua-

[1] Two baselines are said to be equivalent if they represent the same vector in the u, v Fourier space (see fig. 4.1)

tions become inversely proportional to the antenna number instead of its square root (fig. 4.2).

- It has been shown [36] that in this case the sensitivity of a bolometric interferometer is a factor of 2 worse for an Imager. This is the price to pay for having a cleaner detection (fig. 4.3).
- Bandwidth smearing is not a critical issue. An instrument with 20% bandwidth would have a factor of 1.6 sensitivity decrease compared to the sensitivity estimated without taking into account the effect [32].
- The maximum multipole that should be sampled to extract the cosmological information from primordial B-modes is $\ell \sim 125$. Going to higher multipoles would not constrain more tightly the power spectrum estimate (fig. 4.4).

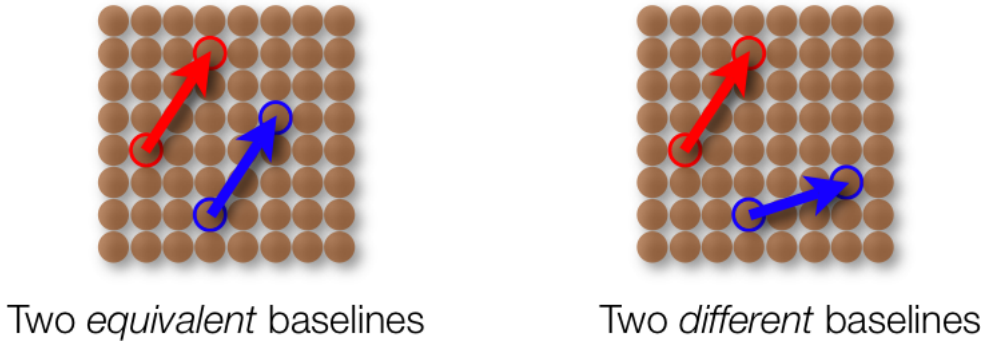

Figure 4.1: Schematic view of the concept of equivalent baselines. Right panel: two equivalent baselines. Left panel: two non-equivalent *different* baselines.

4.2 Instrument global design

QUBIC is a instrument based on the principle of adding interferometry devoted to the study of CMB polarization. The instrument can be seen as a Fizeau interferometer since fringes are displayed in the combiner focal plane all at once (Fizeau fringes) as in the Fizeau instrument [29].
The whole instrument is thought of a set of modules working in three different frequency bands (90 GHz, 143 GHz,220 GHz centered) for a good

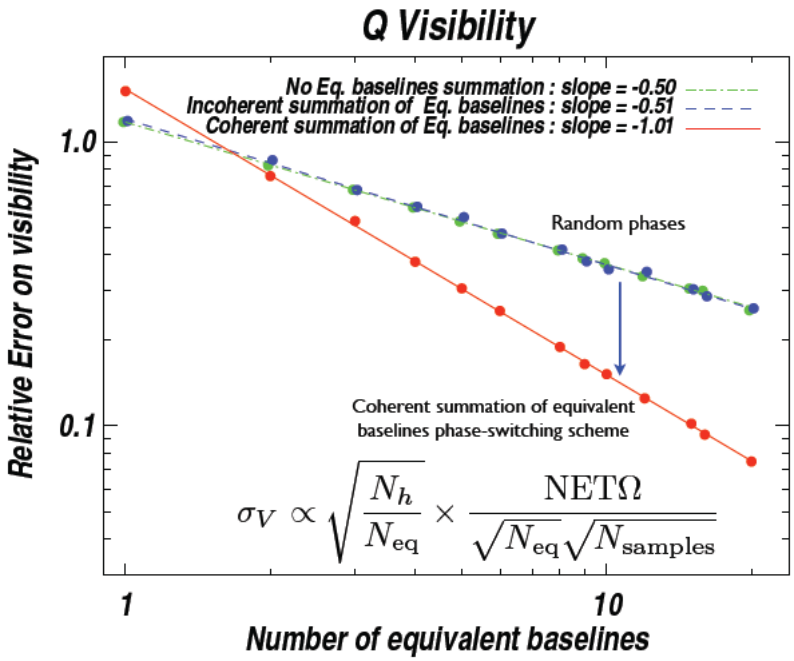

Figure 4.2: Sensitivity estimates for a bolometric interferometer when applying coherent (red line) or incoherent (blue line) equivalent baselines summation. Picture taken from [37].

foregrounds removal. There will be 6 modules for each frequency. The use of 6 modules is required to achieve the sensitivity needed to detect the B-modes signal with r=0.01 in 1 year of integration time [36]. Each module will consist of an instrument assembled and embedded in a cryostat (fig. 4.5).

The first element radiation encounters is the primary horn array, built with n=144 corrugated feed horns with 15° FWHM[2]. The horn separation is roughly the horns diameter $d \sim 12$ mm. This means that the minimum power spectrum multipole sampled is $\ell = 23$, corresponding to the primary horns size and to the multipoles sampling resolution $\Delta\ell$.

Just after the horn an Ortho-Mode-Transducer (OMT) enables the projection of the electric field onto a given base, in order to perform polarimetry. The next step is the passage through a phase shifter that introduces a phase modulation in the wave propagating towards detectors. This phase shifting is mandatory in order to label signals coming from each horn for the detec-

[2]This value has been selected in order to be sensitive down to multipoles $\ell \sim$12.

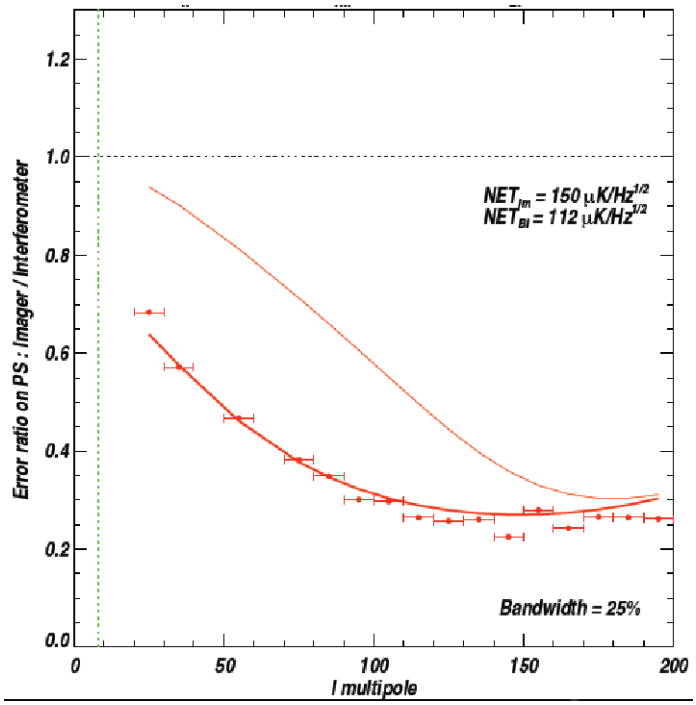

Figure 4.3: Sensitivity estimates for a bolometric interferometer compared to the imager one. Thin red line takes into account sample variance while the thick one is computed considering only noise contributions. Picture adapted from [36].

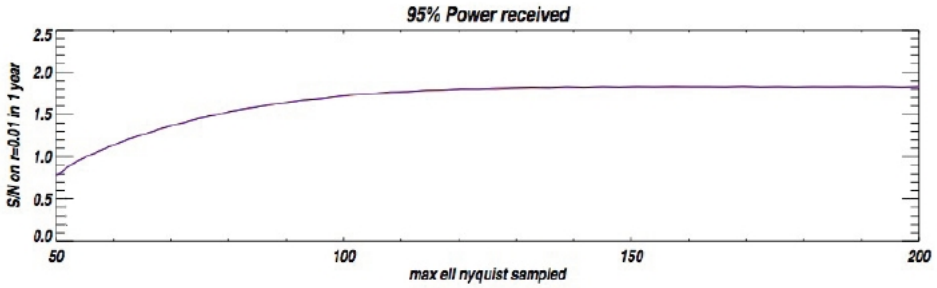

Figure 4.4: Gain in the tensor to scalar ratio r estimate as a function of the maximum multiple ℓ sampled by the instrument. Picture courtesy of J.C. Hamilton.

tion and to recover all the visbilities.

Signals are then ready to be combined just before detection. The usual correlation technique of radio-interferometers cannot be applied to the QUBIC case; since its complexity grows as n^2, this solution cannot be adopted for the QUBIC case and the collaboration has then studied other ways to com-

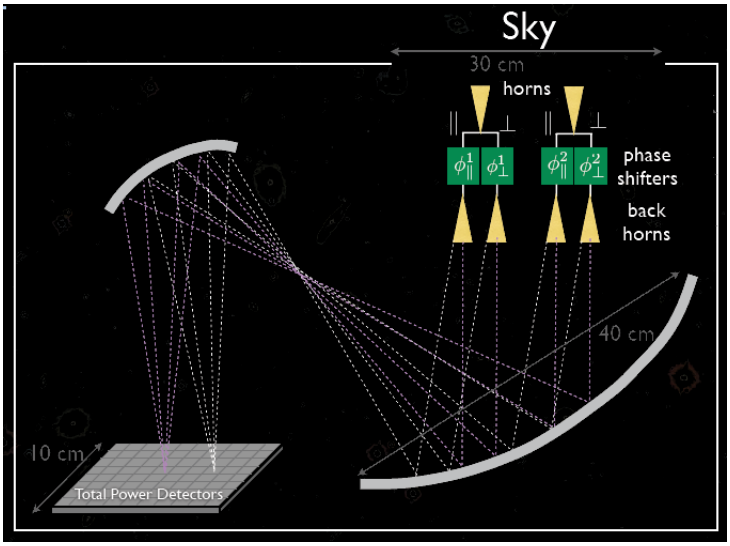

Figure 4.5: Scheme of one module of the QUBIC instrument. After crossing the cryostat window radiation is collected by primary horns and split in polarization (∥,⊥ symbols) inside OMTs and then phase shifted (phase shifters are showed in green). Radiation is then sent to an array of back horns that radiate towards a two mirrors optical systems that sends signals towards the detectors plane.

bine signals. We decided to adopt the principle of adding interferometry to combine signals, in a way analogous to what did the MBI community [28]. Signal combination will be done optically, thanks to a focusing optical system that illuminates a bolometer array where the fields superimposition will produce interference fringes.

Signals, after being phase shifted and split in polarization, will be first rotated by 45° twists in order to be aligned and then sent to $2n$ back horns (fig. 4.5) that re-emit radiation towards the optical system used for the signal combination. Detectors will be placed in the focal plane of this optical system. The aspect of signal detection is thus turned into the solution of a linear system: each bolometer in the detector plane will se a linear combination of signals from the equivalent baselines, where the unknowns are the single baseline visibilities and the linear coefficients are given by the phase modulation by phase shifters [37].

4.3 Optical combiner

The key feature of a bolometric interferometer, in order to maximize its sensitivity is to preserve the coherent sum of equivalent baselines. This means that all the instrument baselines that are represented by the same vector in the Fourier (u, v) plane [12] are coherently summed by the optical system and so they must be in phase in order to maximize the sum.
This way of proceeding can be carried out with a focusing optical system, that will be subsequently called the *combiner*.
The crucial point of the combiner is to map directions launched by the back-horns in its focal plane (fig. 4.5). In this way each direction launched by all the secondary horns is focused in a single, given point in the focal plane. Given the definition of focal plane, this is equivalent to the requirement of summing coherently the equivalent baselines, that produce the same fringe pattern in the focal plane (that is, they have the same fringe period and the same orientation in the focal plane).

4.3.1 First estimates

Sensitivity calculations have established that sensitivity to *primordial* B-modes does not increase significantly if observing at multipoles higher that $\ell = 125$. Consider the case of an instrument module observing the sky with 144 horns with a FWHM of 15° at 90 GHz frequency. The baseline corresponding to $\ell_{max} = 125$ at 90 GHz is $u_{max} = \frac{\ell}{2\pi}$=19.9. The image of the interferogram produced by antennas separated by this baseline would produce fringes separated by a quantity

$$\Delta_{max} = f_{eq} \tan \frac{1}{u_{max}} \tag{4.1}$$

where f_{eq} is the equivalent focal length of the combiner.
In order to correctly sample (to satisfy Nyquist rate) these fringes it has to be required that this separation is at least twice the dimension of the detector in the focal plane. In this way each fringe would be observed at least by two detectors; quantitatively this means that

$$\Delta = f_{eq} \tan \frac{1}{u} = n_s D_b, \tag{4.2}$$

where n_s is the sample number for each fringe (at least 2) and D_b is the bolometer size. Imposing $n_s = 2$ and $D_b = 5$ mm and recalling that $u_{max} \sim 20$ the crucial value $f_{eq} \geq 200$ mm is found.

On the other hand, the fact that the detector number cannot exceed 1000[3] also fixes a limit on the combiner focal length. Consider the minimum baseline of the system, $u_{min} = 4$, the fringe dimension on the focal plane is $\Delta_{min} = f_{eq} \tan \frac{1}{u_{min}}$ and must be smaller than the size of the focal plane, in order to be correctly sampled. Practically this means that with a 150x150 mm focal plane (30x30 pixels size) the peak to valley separation has to be around 75 mm, that implies that $f_{eq} \leq 300$ mm.

The mirror size can be estimated by considering the beams of the horns looking at the sky. As explained in the previous section, before being remitted towards the combiner by the back-horn array, radiation coming from the sky is divided into two polarized components by a set of OMTs. This means that the number of back horns is twice the number of sky horns.

In order to limit the cryostat window size and to keep the sky-horn array as compact as possibile, it is mandatory to keep the linear dimensions of the back horn array similar to those of the sky horn array, implying that the back horn beam size will be larger than the sky horns one, since their aperture is smaller.

Consider a sky horn of 15° FWHM: at a frequency of 90 GHz, its aperture is roughly $d = \frac{\lambda}{\theta_{FWHM}}$=12 mm and its throughput is

$$T_{in} = A_{in}\Omega_{in} \approx \frac{\pi^2 d^2 \theta_{FWHM}^2}{4}. \tag{4.3}$$

If the size of the array has to be preserved, then in the area A_{in} two back horns have to be placed, each of them with an area $A_{in}/2$; imposing the throughput conservation one gets:

$$T_{bh} = A_{bh}\Omega_{bh} \approx \frac{A_{in}}{2}\pi\theta_{bh}^2 = T_{in} = \pi A_{in}\theta_{FWHM}^2. \tag{4.4}$$

This implies a back horn beam FWHM a factor $\sqrt{2}$ ($\theta_{bh} \sim 21°$) greater than the primary horns FWHM.

[3]This is mainly due to technological problems in fabricating such a huge detector array and the related readout electronics. The planned technology for detectors is to adopt TES.

Considering the linear dimension of the sky array $L = (n-2)d \sim$150 mm, the mirror has to be off-axis and cannot be placed at distance from the back horn h smaller than 300mm in order to prevent shadowing or vignetting of the reflected rays by the horn array.
The mirror size is then

$$D_m \approx L + 2h \tan \frac{\theta_{bh}}{2} \sim 400\text{mm}. \tag{4.5}$$

These very rough first estimates define the combiner as a very fast (F# close to 0.5) optical system, having a small focal ratio. Aberrations will be in general present in the focal plane of such an instrument.
On the other hand, it has been showed by the collaboration that the performances of the combiner must be as high as possible in amplitude and phase when illuminated by the different pupils (corresponding to the different back horns). This is clear thinking of the key concept of considering equivalent baselines coherent summation: any detriment of this feature would decrease the signal in the bolometers and the instrument sensitivity. There are two kinds of problems to be faced when considering the combiner performances. The coherent sum of equivalent baselines must be preserved because any deviation from ideality (for example for an amplitude distortion or additional phase introduced by aberrations) would imply a reduction of the coherent signal, reducing the fringe contrast (complex degree of mutual coherence). This argument leads to the definition of a proper estimator representing an efficiency term in the sensitivity formula and expressing how close the combiner performances are with respect to an ideal one producing fringes by the back-horn array with degree of coherence equal to 1.
Moreover, there is another level of estimators that has to be considered and that is in strict connection with the control of systematic effects. Provided a given measured fringe pattern it can be aberrated, and therefore have a degree of coherence less than 1, (since aberrations will introduce phase distortions of the wavefronts coming towards the focal plane), what is relevant to extract the sky signal is the accuracy of the knowledge of the real fringe pattern. This could be done by realistic simulations of the specific instrument. The level of accuracy required in order to take these systematics under control will be investigated in the near future using the simulations

defined in this thesis. The point of a very fast low aberrating combiner induces the search of a suitable design in the class of two mirror telescopes, where recipes to minimize aberrations playing with the mirror surfaces are already explored in literature.
Unfortunately the initial conditions of the problem to be solved are far from the usual hypothesis made to find these conditions: the system under design is not paraxial and often the recipes are derived for systems with objects lying at infinity.
Finally, the combiner, being an interferometer, is intrinsically multi-pupil, this means that the estimator that has to be defined must be sensible to all the pupils, that is to the interferometer baselines distribution.

4.4 Coherent illumination of the combiner

In the QUBIC observing concept a wave entering in one antenna looking at the sky travels through an OMT and a phase shifter that adds a proper phase value to the wave one.
This means that the field radiated by each secondary horn illuminating the combiner has a precise phase value that must be accurately known in order to invert the linear problem for the visibilities in the detectors plane. Consider for example the case of four different horns producing two different representations of the same equivalent baseline, then the phase shift is introduced in a way such the phase difference among them is kept constant in order to maximize the coherent signals summation.
In agreement with the definition of [35], stating that two signals are said to be coherent when there is a precise correlation between their phases, for sure signals of different representations of the same equivalent baseline are coherent.
Extending this argument it can be stated that each set of equivalent baselines illuminates the combiner in a coherent way.

4.4.1 Coherent Spread Function

The description of the properties of an optical system illuminated in a coherent way is given in terms of the so called Coherent Spread Function (CSF).

The CSF describes the ability of the system to produce coherently illuminated image of a given coherent object. It relates the amplitude of the field in the object plane to the one in the image plane of a system that is coherently illuminated. This relation is proven to be linear.
When the object illumination is coherent, the various wave trains in the image plane must be added on a complex amplitude base[4]. Thus a coherent imaging system is linear in complex amplitude.
Consider the complex wave phasor $E_o(r,t)$ expressing both the phase and the amplitude of a wave in the object plane of the system, then according to diffraction theory its image in the system image plane is:

$$E_i = \int dr_o h(r_o - r_i) E(r_o, t-\tau), \tag{4.6}$$

where h is the impulse response of the system, that is its coherent point spread function (CSF).
Moreover the intensity in the image plane is

$$I_i = \langle |E_i|^2 \rangle = \int\int dr_{o1} dr_{o2} h(r_i - r_{o1}) h^*(r_i - r_{o2}) \langle E(r_{o1}, t_1 - \tau_1) E^*(r_{o2}, t_2 - \tau_2) \rangle, \tag{4.7}$$

Where $h(r_i - r_{o1}), h(r_i - r_{o2})$ are the CSFs of the optical system in imaging the point 1,2 of the coherent object. Looking at eq 4.7 one can notice that, provided the field is stationary (see chapter 2),

$$\langle E(r_{o1}, t_1 - \tau_1) E^*(r_{o2}, t_2 - \tau_2) \rangle = \langle E(r_{o1}, t_1) E^*(r_{o2}, t_1 - \tau) \rangle = \Gamma_{12}(r_{o1}, r_{o2}, \tau), \tag{4.8}$$

where Γ_{12} is the complex mutual coherence function of the object.
This argument underlines that the intensity in the image plane depends upon the coherence of the object. Starting from this it can be proven that the system is linear in complex amplitude [35] and highly non linear in intensity mapping.
Recalling the mutual coherence definition and fixing $\tau = 0$ [5] eq 4.7 can be

[4] Since there is a precise phase relation, the phase of each impulse can be known at any time.

[5] Setting $\tau = 0$ simply means that the mutual coherence function will express the *spatial* coherence of light in two distinct object points.

rewritten so that one gets:

$$I_i = \int\int dr_{o1} dr_{o2} h(r_i - r_{o1}) h^*(r_i - r_{o2}) E(r_{o1}) E^*(r_{o2}, 0) = \Big| \int dr_o h(r_i - r_o) E(r_0) \Big|^2. \tag{4.9}$$

It's then clear that each property the combiner has to satisfy in reality applies for the various CSFs h_i of the different pupils that coherently illuminate the combiner. To estimate the performances of the combiner it's thus mandatory to derive information about the CSFs of the various pupils (back-horns) that illuminate it.

4.5 Incoherent illumination

Ideally, as explained in the previous section, the optical combiner is illuminated in a coherent way, but there could be various effects in the instrument that produce incoherent illumination of the system.
In the case of incoherent illumination the phasor amplitudes across the object change in a statistically stochastic way. This is the case for example of spurious effects that are introduced by non-idealities of the system that alter in a unpredictable way the phase of the wave traveling from the horns looking at the sky towards the back horns.
The fact of having statistically independent phase variations can be modeled in eq 4.7 considering that in this case

$$\langle E(r_{o1}, t_1 - \tau_1) E^*(r_{o2}, t_2 - \tau_2) \rangle \propto I_o(r_1) \delta(r_1 - r_2) \tag{4.10}$$

that express that there is no phase correlation in the object.
Substituting this results into eq 4.7 leads to the result

$$I_i(r) \propto \int dr_o \Big| h(r_i - r_o) \Big|^2 I_o, \tag{4.11}$$

that shows that for incoherent illumination the image intensity is the convolution of the intensity impulse response $|h|^2$. A incoherent imaging system is linear in *intensity*, opposed to the coherent case where its response is linear in *amplitude*. The quantity $|h|^2$ is called Point Spread Function (PSF) and express the relation between the intensities of the image and of the incoherent object that is illuminating the optical system.

While dealing with interferometers and extended objects it's useful to express eq 4.11 in the Fourier plane [38]: by Fourier transforming both sides of equation one gets:

$$I(\nu_{sp}) \propto \int dr_i I_o(r_o) h(r_o - r_i) e^{-2i\pi\nu_{sp} r_i}, \tag{4.12}$$

where the quantity $\int dr_i h(r_o - r_i) e^{-2i\pi\nu_{sp} r_i}$ is the Fourier transform of the system PSF, called Optical Transfer Function, [35] and ν_{sp} is a spatial frequency (inverse of a length).
The OTF is the Fourier transform of the PSF and describes the ability of a system in imaging an object that has a sinusoidal shape in the domain of spatial frequencies (fig. 4.6) [34]. When dealing with interferometers the

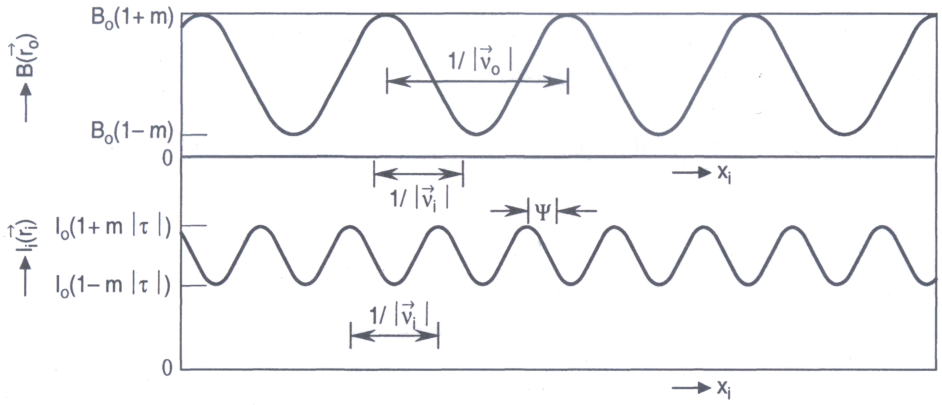

Figure 4.6: Example of imaging of a sinusoidal object by an optical system: The image contrast with respect to the object one is given by the OTF modulus (MTF), while the phase change is given by the OTF argument (PTF). Picture taken from [34].

OTF is useful, since it's defined just in the spatial frequency domain. More in detail, recalling that a baseline b subtends a spatial frequency $u = \frac{b}{\lambda}$, the modulus of the OTF will tell the efficiency in imaging an incoherent object with a spatial frequency component u. If the combiner has a focal length f_{eq}, while imaging a spatial frequency u, the corresponding detail in focal plane will have a dimension Δ:

$$\Delta = f_{eq} \tan\frac{1}{u} \approx \frac{f_{eq}}{u}, \tag{4.13}$$

and the spatial frequency on the focal plane will be:

$$\nu_{sp} = \frac{1}{\Delta} \approx \frac{u}{f_{eq}}. \tag{4.14}$$

To understand the role of incoherent illumination of the combiner focal plane OTF simulations are needed. It can be shown that the OTF has a cutoff frequency [35]: provided that the combiner OTF cutoff frequency is smaller than the focal plane spatial frequency $\nu_{sp,min}$ corresponding to the smallest back horn array baseline, then the incoherent illumination of the combiner by the back hors array won't affect the measurements.

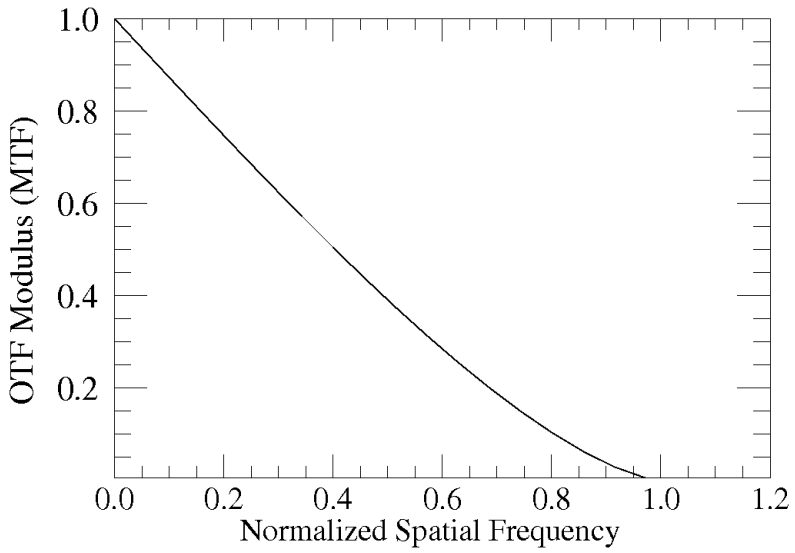

Figure 4.7: Cross section of the OTF of an aberration free optical system as a function of the spatial frequency normalized to its cutoff value.

4.6 Estimators for the requirements

The QUBIC combiner can be described as a system that produces the map in its focal plane of the directions launched by the secondary back horns. This means that all rays launched by different horns (pupils) in the same direction are all focused in the same place in the focal plane. In this sense the combiner can be seen as a dirty imager with very crap imaging capabilities. It must be kept in mind that the combiner transfers the field radiated by

the horns in its focal plane, where the detectors detect signal performing a *coherent* sum.

An estimator that wants to describe the combiner performance must therefore give information on how *fields* are transferred to detectors.

The information on both phase and amplitude transfer tell the combiner efficiency in producing interference fringes. Obviously this efficiency will affect the instrument sensitivity, so it's mandatory to keep it as close to 1 as possible in order to maximize the instrument performances.

The complex degree of mutual coherence γ_{12} offers the capability of estimating both phase and amplitude efficiency in one shot. Recalling chapter 2 it can be stated that

$$|\gamma_{12}| = \frac{I_c}{I_i}, \tag{4.15}$$

where I_c and I_i are the coherent and incoherent intensities respectively registered by the detector. The complex degree of mutual coherence thus tells the fraction of the total intensity detected used to produce fringes.

There can be various reasons for an efficiency loss, for example phase and amplitude distortions of the wavefront at the detectors plane due to aberrations, but they would all lead to a reduction of the fringes contrast, that is of the modulus of the complex degree of mutual coherence.

The evaluation of γ_{12} for each set of equivalent baseline tells which is the mean efficiency the system has in producing that kind of fringe, compared to the ideal case where $\gamma_{12} = 1$. To do this it is important to know the coherence features of the source used to produce fringes. As stated in the previous section, all sources producing the same equivalent baseline are coherent because of the presence of phase shifters. Moreover in the simulation performed with ZEMAX all sources have been considered to be perfectly coherent ($\gamma_{12} = 1$)). This means that the estimation of γ for a given fringe pattern of the detectors will exactly tell the efficiency term needed (compared to the ideal case).

Anyway the step of equivalent baselines averaging cannot be done with ZEMAX since it's not possible to introduce phase shifters inside the code. Because of this fringes have been off-line averaged.

The simulation code written in ZEMAX operates through the following

steps:

- Fixes the baseline length and orientation (equivalent baseline definition).
- It simulates and saves the coherent irradiance (fringe pattern) registered by the detectors while looping among all the possible representation of the selected equivalent baseline.
- The possible representation of the fixed baselines are recovered shifting the sources (pupils) positions inside a pair nested loops.

4.7 Fringes efficiency simulation results

The ZEMAX sequential editor has been used to design a system to be tested. The design is based on the arguments presented in Appendix B. The selected system to be tested is a Gregorian combiner with an equivalent focal length $f_{eq} = -241.8$ mm; table 4.1 presents values of all the parameters needed to fix the system (see appendix A for a complete description of these parameters). As a starting point, the back horn array has been implemented in

Parameter	Value	
Primary-backhorns distance	h	400 mm
Secondary mirror magnification	k	1.1
Bending angle	φ	50°
Exit focus	s	0.7
Horizontal dimension	l	1
Secondary curvature radius	R_1	254.5 mm
Secondary curvature radius	R_2	280 mm
Angle between mirror axes	α	59.2°
Equivalent focal length	f_{eq}	241.8 mm

Table 4.1: Gregorian combiner parameters values.

ZEMAX with a set of 144 (12x12) point sources radiating a beam with 10° FWHMs. The sources separation is 20 mm, so that the total length of the array side is 240 mm. The array is located in a yx plane of the reference system used in fig. 4.8: baselines parallel to the y axis are called *horizontal*, while those parallel to the x axis are said to be *vertical*. The test have

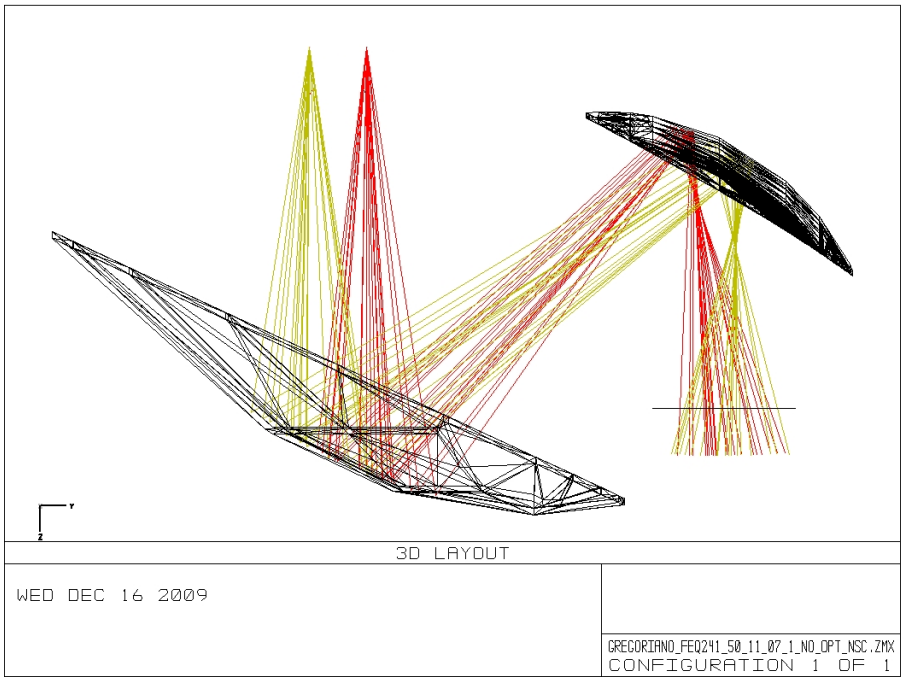

Figure 4.8: yz projection of the combiner under test in the ZEMAX NSC environment showing a 60 mm y displaced (*horizontal*) baseline illumination.

been carried out in the non-sequential mode of ZEMAX, where one, despite having less tools for the optimization, has direct access to the detected intensities. The 150 mm x 150 mm focal plane has been equipped with 30x30 5 mm naked detectors.

Figs 4.10, 4.11 present the modulus of the complex degree of mutual coherence for the mean fringe pattern simulated for different lengths of horizontal and vertical baselines. The maximum length considered is b=70 mm, that corresponds to a multipole ℓ=125 at 90 GHz frequency (see section 4.3). In fig 4.9 an example of vertical and horizontal fringes are presented. In this case no aberrations are present, because very narrow ($< 1°$) beams have been used. For horizontal fringes the modulus of the complex degree of mutual coherence is computed for each column of the detectors array, while for vertical ones the computation is for each row of detectors. The computation is done on the off-line averaged signal, realized averaging all the simulated fringes corresponding to different representations of the same equivalent baseline.

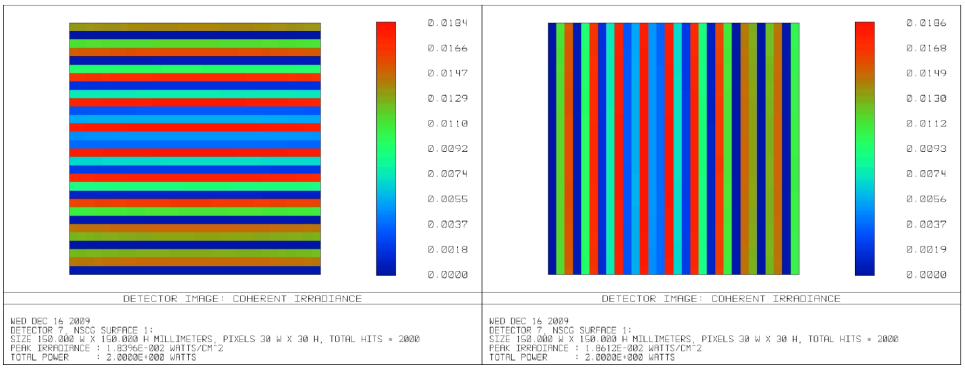

Figure 4.9: Left panel: an example of fringes in the detectors plane produced by a 60mm *horizontal* baseline. Right panel: an example of fringes in the detectors plane produced by a 60mm *vertical* baseline.

The complex degree of mutual coherence presents a clear decrease in the

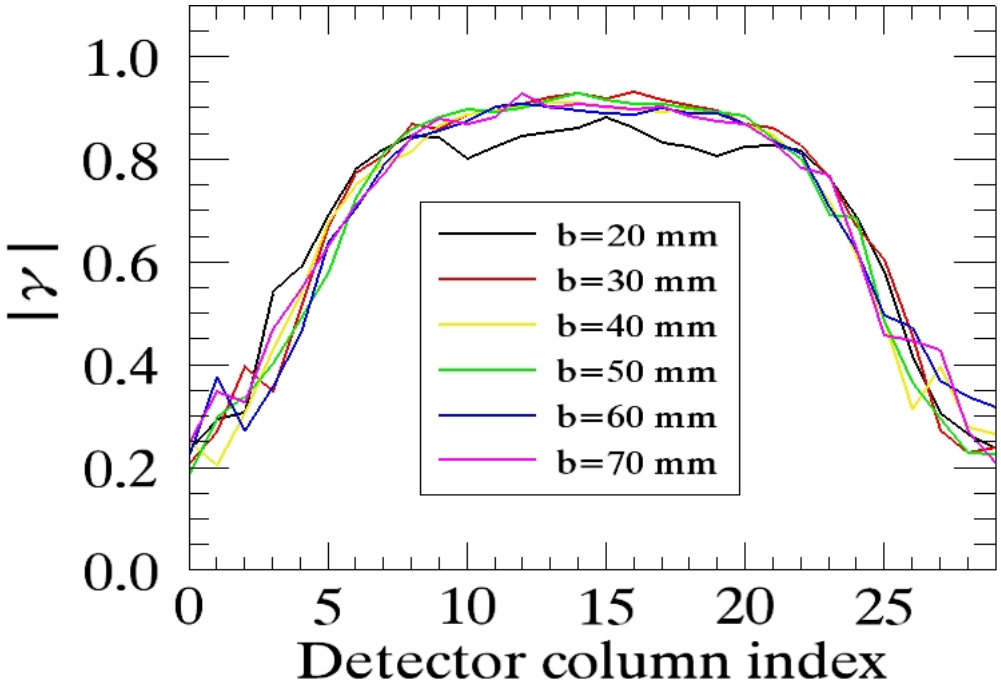

Figure 4.10: Modulus of the complex degree of mutual coherence for horizontal equivalent baselines as a function of the column index of the ZEMAX detectors plane. The back horns sources have a 10° FWHM.

borders of the detectors plane. This is due only to an increasing amount of aberrations while increasing the distance of the detectors from the array

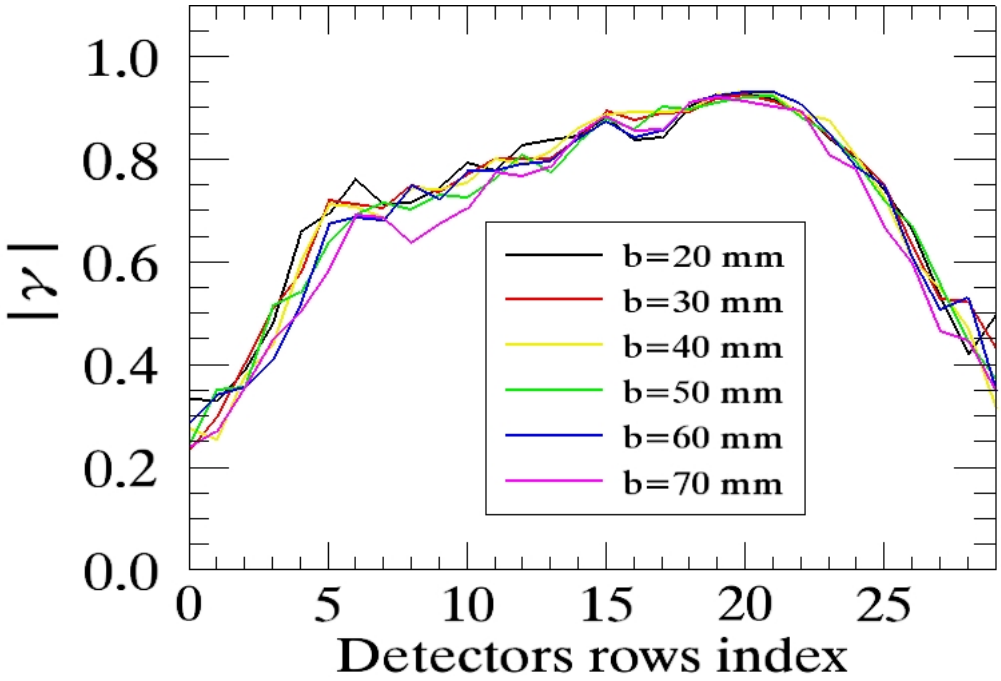

Figure 4.11: Modulus of the complex degree of mutual coherence for vertical equivalent baselines as a function of the row index of the ZEMAX detectors plane.The back horns sources have a 10° FWHM.

center (row/column #15).

Vertical baselines present a degree of coherence with a peak around row #20 instead of at row # 15 (arraycenter), this is due to the presence of coma that in off axis systems breaks the azimuthal symmetry of the image.

The same simulations have been repeated on the same system using a source with 5° FWHMs instead of 10° as in the previous case. Simulations have been done using the same detectors plane of the previous case. Results are presented in figs. 4.12, 4.13 and indicate a clear gain in the fringes efficiency. This is clear because using a narrower beam the parts of mirrors to be used are smaller compared to the ones used with a 10° beam and therefore the surfaces curvature radii is more uniform, leading to less aberrations. It has to be stressed that to compare the performances of the two different illumination cases an edge taper [6] for the total power on the focal plane has to

[6]The edge taper is defined as the level at which the encircled energy carried by the beam is cut. For example is the edge taper is -20dB then 1% of the energy carried by the beam is lost.

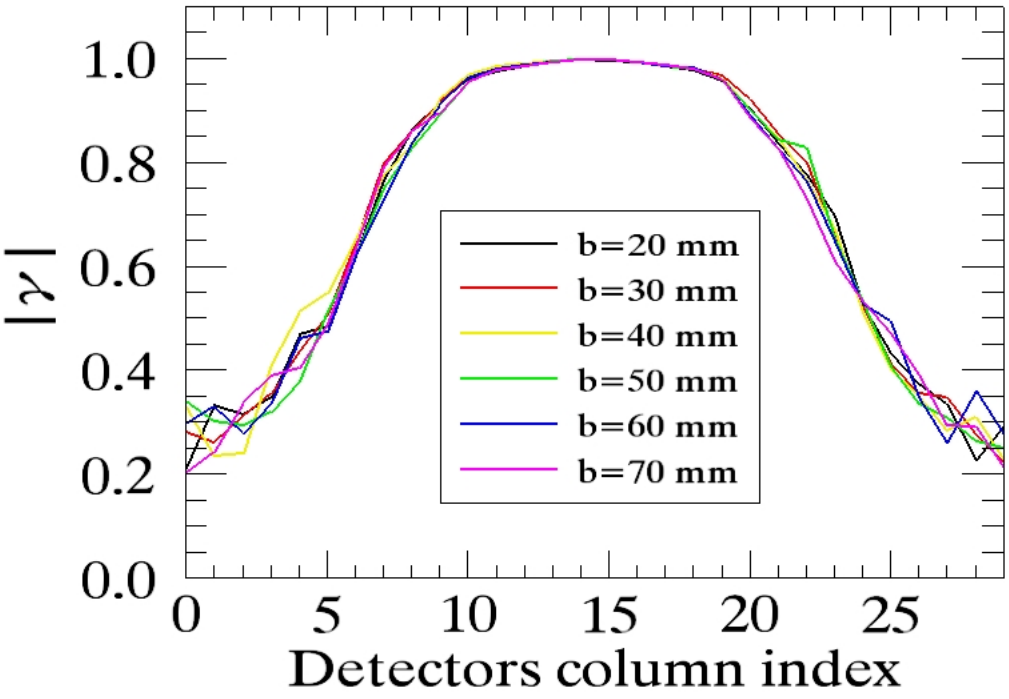

Figure 4.12: Modulus of the complex degree of mutual coherence for horizontal equivalent baselines as a function of the column index of the ZEMAX detectors plane. The back horns sources have a 5° FWHM.

be fixed. Fixing a taper at 95% level means that the rows/columns of interest are those within 3-27 for the 10° illumination case, corresponding to rows/columns 7÷22 for the 5° case. Results of this comparison are presented in figs 4.14 and 4.15, where the values of the complex degree of coherence for each equivalent baseline averaged in this intervals are plotted in both cases as a function of the baseline length. The use of a 10° FWHM beam implies a reduction of the fringe efficiency of order 20% with respect to the 5° FWHM case. This consideration express the crucial role played by the back horns beam in the instrument definition. It's mandatory inside the collaboration to look for a way to try to reduce the back horn beam divergence in order to increase the instrument sensitivity.

Moreover, no significative dependance from the baseline length is found, since the maximum variation in this direction is just of order 4% for the 10° FWHM case and 2% in the 5° FWHM: this higher "stability" is another

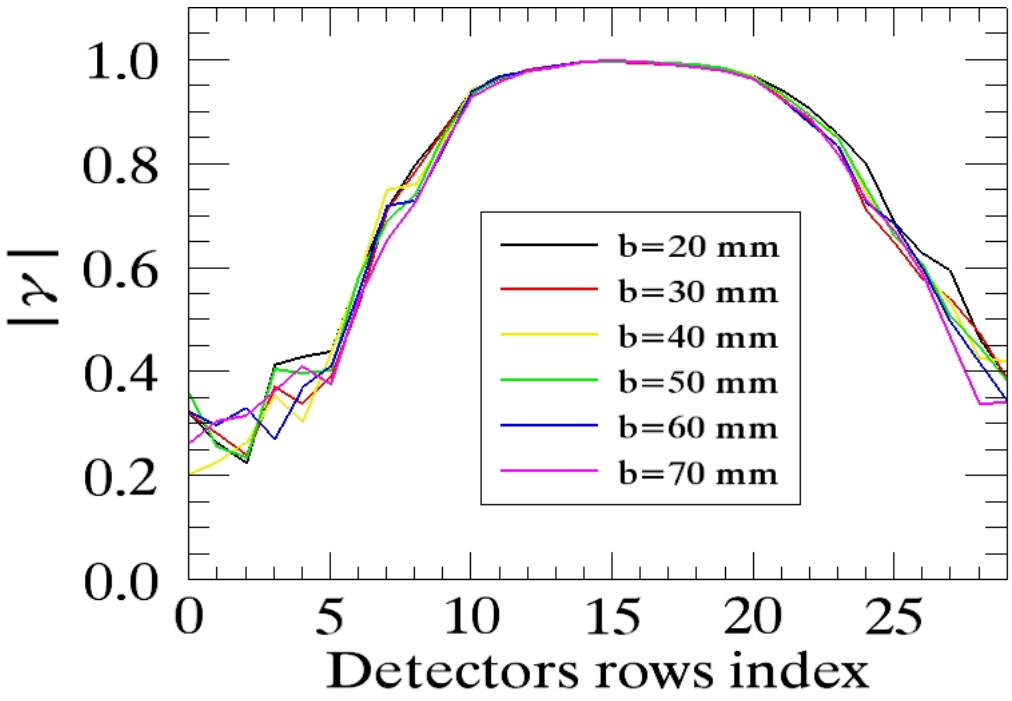

Figure 4.13: Modulus of the complex degree of mutual coherence for vertical equivalent baselines as a function of the row index of the ZEMAX detectors plane.The back horns sources have a 5° FWHM.

indication of the gain in narrowing the illuminating beam.

Finally no significant difference between horizontal and vertical efficiencies is found.

The method presented in this section enables to indirectly derive the aspect of the CFSs of the system via the direct simulation of the fringe patterns in the combiner focal plane. It is important to stress again that these simulations indicate the efficiency level in producing interference fringe: the collaboration must now define an experimental method to validate these simulation, in order to establish their accuracy level.

4.8 Back horns beam image efficiency

The complex degree of mutual coherence is a relative measurement, since it tells what fraction of the total intensity delivered on the detector is used to produce fringes.

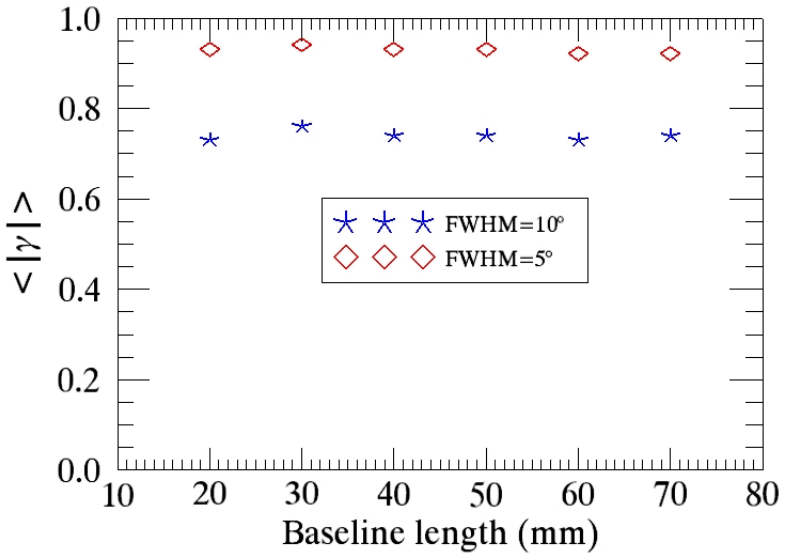

Figure 4.14: Comparison between the mean modulus of the complex degree of mutual coherence as a function of the horizontal equivalent baselines length for a 5° back horns FWHM (red diamonds) and 10° back horns FWHM (blue asterisks).

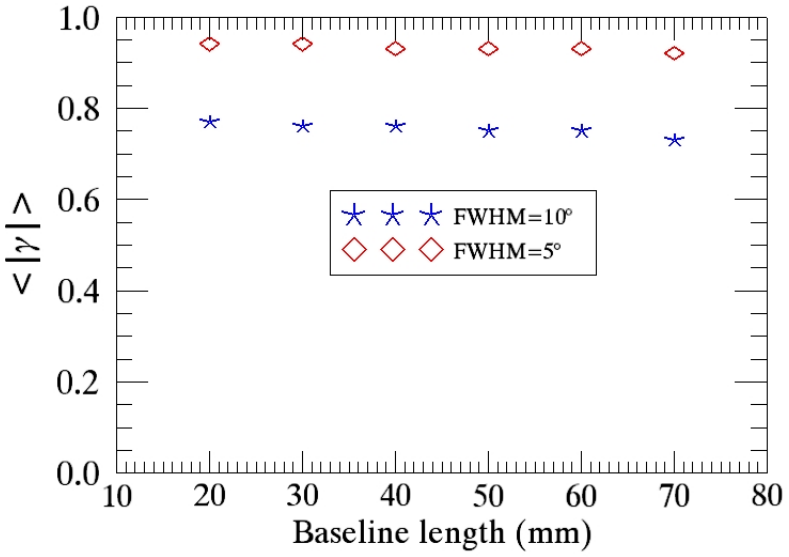

Figure 4.15: Comparison between the mean modulus of the complex degree of mutual coherence as a function of the vertical equivalent baselines length for a 5° back horns FWHM (red diamonds) and 10° back horns FWHM (blue asterisks).

Because of diffraction (like in the Young experiment), fringes will be convolved with the diffraction pattern of the apertures, that is with the image

made by the combiner of the back horns beam pattern. This pattern will tell the total intensity level with respect to the delivered one according to eq. 4.11. Only a fraction of this power will be used to produce fringes, that is

$$I_{tot} = I_i + I_c \tag{4.16}$$

$$I_{tot} = \frac{I_c}{\gamma_{12}} + I_c \tag{4.17}$$

$$I_c = \frac{\gamma_{12}}{1+\gamma_{12}} I_{tot}, \tag{4.18}$$

And the back horns beam pattern on the detectors will tell the relation between I_{tot} and the intensity delivered by the back horns.
Therefore, the effect of γ_{12} decreases in the borders of the detectors plane (see figs 4.10, 4.12 as examples) must be added to the back-horns beam efficiency which is still decreasing at the borders of the detectors array. Fig 4.16 shows the back horns beam pattern image simulated for all the

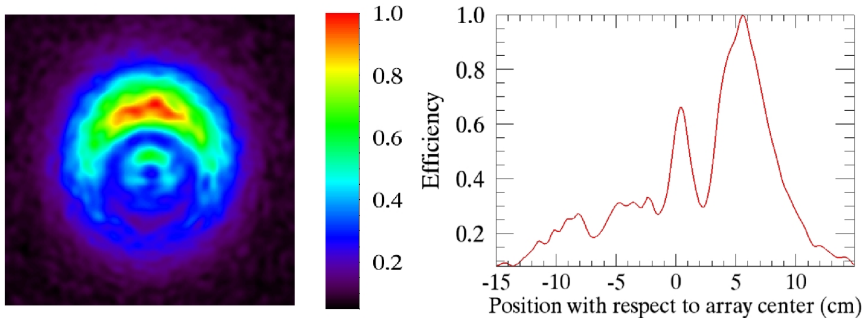

Figure 4.16: Normalized mean image of the back horns beam patterns images: contour plot (left panel) and central pixel vertical cross section (right panel).

back horns simultaneously illuminating the combiner. The average has been performed in order to have a mean "common" profile. Given the proximity of back horns with respect to the primary mirror, and the lateral displacement with respect to the optical axis the pupil functions of each back horns will differ from all the others, leading to a different image in the focal plane.
The mean profile is distorted by aberrations but it can be seen that in the detectors plane borders signal is expected to be a factor 10 less than the peak. By using eq. 4.18 it can be derived that the coherent signal will be a factor 30 (in the borders $\gamma \sim 0.5$) less than the peak total intensity.

This argument indicates that a smaller taper value (with respect to 95%) can be defined for the detectors, since signal in the borders of the focal plane will be a factor 30 smaller that the one in the central region. This means that a longer focal length for the combiner could be chosen, since the upper limit on it given by the number of effectively illuminated detectors is relaxed. By the way a smaller taper value would also decrease the mirror sizes.

4.9 OTF simulations results

To estimate the combiner behavior when incoherently illuminated simulations of its Optical Transfer Function have been carried out in the ZEMAX sequential mode (see fig 4.17). This is a standard built-in ZEMAX procedure. As it can be noticed the efficiency in sampling spatial frequencies higher

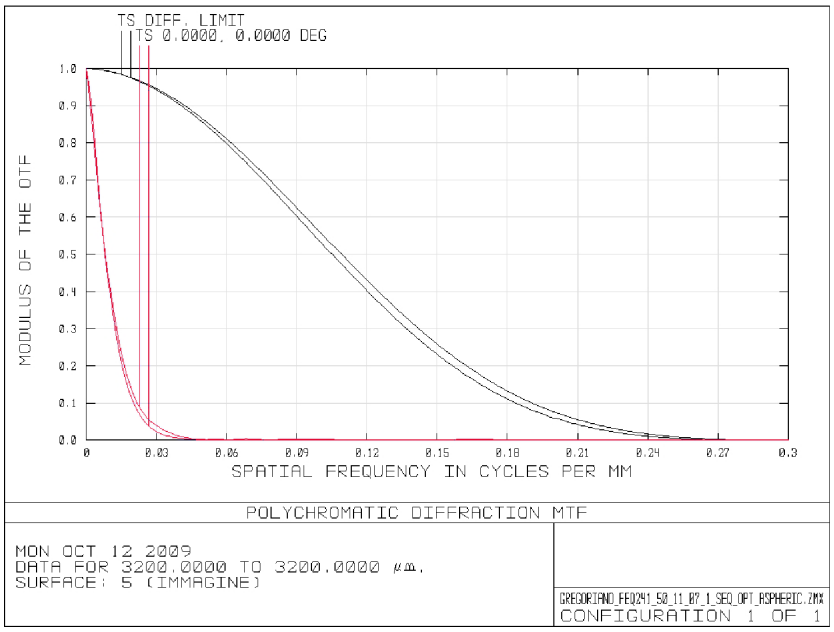

Figure 4.17: Modulus of the OTF (MTF) for a 10° FWHM point-like illuminating object placed at an height h=400 mm with respect to the primary mirror vertex (red line). For comparison the MTF of the same diffraction limited combiner when illuminated by a plane wave lying at infinity is showed (black line). The label T and S stand for *tangential* and *sagittal* rays.

than 0.04 cycles/mm is almost zero. Recalling that $\nu_{sp} \sim \frac{u}{f_{eq}}$ this means that baselines longer than 10 mm are almost not sampled. Uncorrelated sig-

nal coming from distances higher than this won't thus affect measurements. This reflects the fact that the combiner can be seen as a *dirty* imager, the MTF explaining how much is dirty: if it would have been a well performing classical Gregorian telescope its MTF would have been close to the black line in fig 4.17.

Chapter 5

The SAGACE FTS optical layout

5.1 Introduction

In 2007 ASI (Italian Space Agency) came up with a call for proposal for a small space mission.
Among the proposal there is SAGACE (Spectroscopic Active Galaxy And Cluster Explorer, www.asi.it), a multipurpose mission mainly devoted to the observation of the SZ effect from galaxy clusters.
Other targets of the mission are the observation of the millimeter wave part of the spectrum of Active Galaxy Nuclei and the high resolution ($R = \frac{\lambda}{\Delta\lambda} \sim$1000) spectroscopic survey of the C^+ from far ($z \sim 1.5$) starburst galaxies.
The idea is to build a single multipurpose spectrometer operating at different frequency bands to investigate these targets switching its operational mode.
Because of these requirements the collaboration decided to build a Fourier Transform Spectrometer (FTS), the only spectrometer type that guarantees the flexibility needed to observe the targets with the same instrument.
The optical project of the FTS is a task that has to be performed in strict connection with the whole design of the payload. Once the scientific requirements for the mission and the instrument are assessed the optical definition of the instrument is connected with the design of the telescope, that provides the input for the spectrometer, and of the detectors, that are the

instrument output. Moreover, the instrument has to satisfy mechanical conditions of weight and dimensions that have an impact on the design of the cryostat. Finally, the layout has to provide a system for the realization of the optical path difference needed to achieve the desired spectral resolution, that must be mechanically simple and robust.
The Martin-Pupplet two beam interferometer scheme is followed, that is division of the input and the recombination of signals in the output is done via polarization division instead of the beamsplitters used in the standard Michelson scheme.

5.1.1 Main requirements for the spectrometer

Spectral range and resolution

The instrument has to operate in a huge frequency range, from ν_{min}=100 GHz (λ_{max}=3.0 mm) to observe AGNs, to ν_{max}=750 GHz (λ_{min}=0.4 mm) for the C^+ line detection.
Indeed the different observations to be done require different spectral resolutions $R = \frac{\lambda}{\Delta\lambda}$ for a correct detection.

- For AGNs observations no spectral features are expected, this means that a photometric survey is to be preferred in order to maximize sensitivity (increasing bandwidth). Observations could be done with a very low spectral resolution $R \sim 2 - 10$ with spectral elements of few tenths of GHz in the bandwidth from 100 GHz to 200 GHz.

- SZ effect has a smooth spectroscopic feature and a moderate spectral resolution ($R \sim 10 - 50$) is required to reconstruct it. Observations could be done with a number of spectral elements $M \sim 10 - 50$ and spectral elements of few GHz of width in the band 100-4560 GHz.

- The observation of a sharp features as a line (C^+ in this case) require an high resolution ($R \sim 500 - 1000$) operational mode, with spectral elements ∼1 GHz wide in the frequency band 720 GHz-760 GHz.

Telescope and FOV requirements

Given the maximum dimension than can be carried by the space vector (Soyuz), which has a bay around 3.7 m of diameter, the primary mirror of the telescope plus the shields cannot exceed this size. This aperture dimension corresponds to a diffractive PSF of 4-5 arcmin at 100 GHz, 1.5 arcmin at 300 GHz and 0.7 arcmin at 700 GHz.
In order to make surveys of a significant part of the sky a moderate Field Of View around 15-30 arcmin (that means two 3x3 pixels observed regions at 100 GHz) of the telescope is required.

Detectors arrays and bands

Sensitivity simulations have prooved that observations can be carried out by splitting the whole 100 GHz-760 GHz band in 4 different sub-bands: in the same way 4 detectors planes (one per sub-band) are placed after the FTS to detect radiations. These arrays cover a sky area which is roughly 15x15 arcmins and are made by a different number of detectors in each sub-band because of the changing of the diffraction limited PSF in each sub-band, as shown in table 5.1 With this division AGN observations and SZ effect would

Band	Frequency (GHz)	Array size	Pixels number	PSF[1] (arcmin)
#1	100-200	3x3	9	4.5
#2	200-300	6x6	36	2.25
#3	300-450	9x9	81	1.5
#4	700-740	18x18	324	0.75

Table 5.1: Different instruments sub-bands and the number of detectors required to cover the same 15x15 arcmin field

be observed in the first 3 bands while the 4th band would be devoted to the starbust galaxies study.

5.2 Analysis of different solutions for the required spectrometer

The spectrometer needed for the focal plane of SAGACE must have the following performances in order to correctly reach the scientific targets of

the mission

- The spectrometer must have a very broad frequency response from 100 GHz to 760 GHz in a single instrument.
- The spectrometer must be tuned in different operational regimes to fit the different targets to be observed. This requires a very flexible instrument.
- Imaging capability is required in order to produce maps of fraction of the sky.
- High spectral resolution is required especially for the highest frequency sub-band.

5.2.1 Diffraction grating

The use of a diffraction grating (DG now on) could be interesting from the point of view of sensitivity, since it has been shown that DG is the most sensitive instrument in photon noise limited observations [39]. Radiation background is in fact limited to the single spectral element, this allows the use of very low NEP detectors.
On the other hand the use of DG has different drawback to be considered.
A DG has dimensions D comparable to $D \sim R\lambda$, this means that the highest sub-band require an instrument at least 300 mm big, and this is also the dimension of the beam incident to the DG.
Thousands of detectors are required to collect radiation along the line of dispersion, moreover this structure does not allow direct imaging since dispersion destroys the spatial information carried by radiation.
The groove size fixes the spectral resolution and it's therefore not easy to change it; this implies the use of a single DG for each sub-band. This has a drawback since it requires the optimization of the single DGs and their corresponding detectors to their operational sub-band.

5.2.2 Fabry-Perot Interferometer

As for DG, the Fabry-Perot scheme (FP) has a background limited by the spectral element, allowing the sub-band detectors optimization and the use

of very sensitive detectors.
In addition FP presents imaging capabilities.
The price to pay for the low background is anyway high: each spectral element is acquired sequentially. This means that having M spectral elements the integration time for each source increases by a factor M.
As for DGs, different instruments are needed for the sub-bands, since the spectral resolution is fixed by the finesse parameter that cannot be easily changed within the same instrument.
This solution presents also technological issues that appear not to be easily solved.
First of all the mechanical cryogenic apparatus needed to move one of the interferometer mirrors has to be really accurate ($\sim 30\mu$m to satisfy the $\lambda/14$ Marechal criterium [16]) to reach $R \sim 1000$. Moreover, the accuracy in the surface planarity and positioning for λ=0.4 mm is only 1μm which is hard to achieve.

5.3 FTS spectrometer

The FTS solution presents the features closer to what is required for the SAGACE targets.
An FTS has imaging capability, and is very flexible, being possible to observe all the targets with the same instrument. This can be done because the spectral resolution can be changed simply changing the optical path difference (OPD) introduced to produce the interferogram.
Moreover, spectral elements are all observed in the same time, in contrast with the FP interferometer (Fellget advantage). Precisely all the spectral elements are seen by the same detector at the same time and this is a very nice opportunity to limit the detector numbers, saving room in the cryostat.
Finally, since the interferogram is modulated by the OPD change, a differential instrument can be implemented.
The flexibility of the instrument translates into a higher background level that comes from each whole sub-band.
This instrument, as the FP case, requires moving parts to be placed at cryogenic temperatures. Last but not least, beam separators for the sub-band

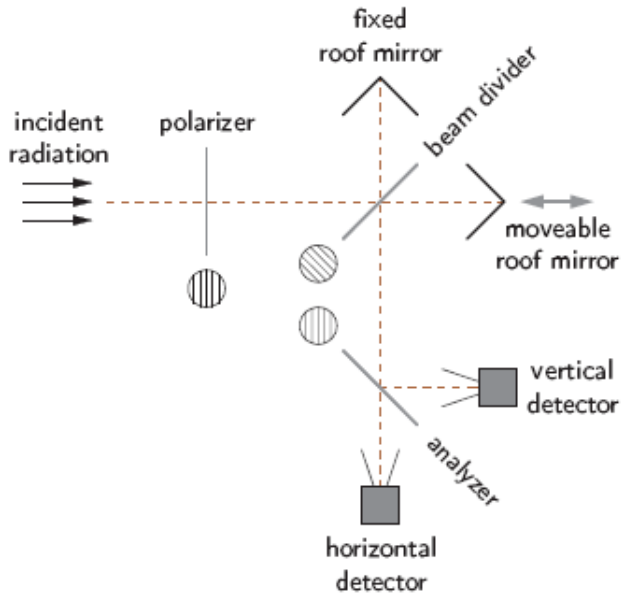

Schematic of a Martin-Puplett interferometer.
The alignment of the wire grids is outlined as seen in
projection by the first incident beam.

Figure 5.1: Scheme of the classical Martin Pupplet interferometer. A wave entering the instrument gets polarized by a polarized and the split in polarization by a beam divider. OPD is inserted with a movable roof mirror. Radiation is detected with a detectors couple.

splitting are needed: it's convenient to build a Martin Pupplet two beam interferometer where the input beam division is done in polarization, instead of a classical amplitude division Michelson one.
Because of all these arguments and of the weaknesses of the other presented solutions the collaboration decided to adopt a Martin-Pupplet [19] FTS instrument to be placed in the telescope focal plane.

5.4 SAGACE FTS Optical Layout

The Martin-Pupplett interferometer is a two beam interferometer very similar to the classical Michelson one. Incoming radiation is split in two parts, that are then phase shifted one with respect to the other, (via the introduction of an OPD with a moveable mirror) and finally recombined to obtain the interferogram.

The main difference with respect to Michelson scheme is that the incoming field division is not performed thanks to a beamsplitter (amplitude division) but with a polarizer that divides radiation in two orthogonally polarized beams (polarization division). This has been proven to be far more efficient than amplitude splitting in the mm-wave spectral region. After inserting an OPD among the two branches of the instrument polarizations are then realigned before detection in order to make fields interfere.

The core of the interferometer is the section where the optical path difference is inserted. In the Michelson case this is done with a simple translating mirror that introduces a delay in one instrument arm with respect to the other one which is fixed.

In the Martin-Pupplet case this is no longer possible because of polarization splitting. Suppose to have a polarized input (eventually produced by a previous wire grid), then polarization division is achieved with a polarizer with polarization axis 45° rotated with respect to original polarization direction. In this way half of the power is transmitted and half reflected back.

Signal are now sent to a translating mirrors couple, where the phase shift is introduced and that sends back field to be superimposed in the interferometer output. What is needed is a 90° rotation of both the polarizations in

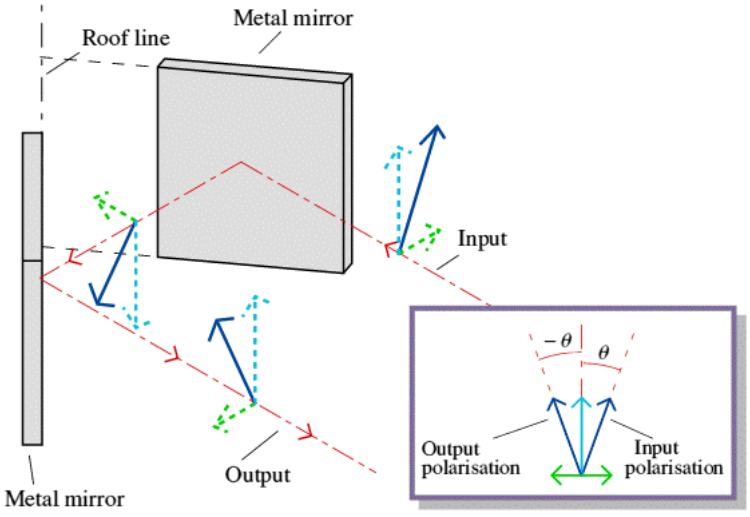

Figure 5.2: Scheme of the action of a roof mirror in polarization rotation.

order to make the field transmitted to be reflected *after* the polarizer and the reflected one to be transmitted *by* the polarizer (fig 5.2). Polarization rotation is achieved with roof mirrors [42], that have the property of rotate the polarization direction of an angle twice the angle of the incoming direction with respect to a line, called the roof line, usually selected to be the direction of the original polarization. This way of dividing signals is much more efficient with respect to beamsplitters when dealing with large bandwidths in the mm-wave part of the electromagnetic spectrum. This scheme has already been used in space missions with astrophysical targets, for example for the FIRAS [3] experiment on the COBE satellite, that measured the CMB frequency spectrum in the early 90's. The other very important

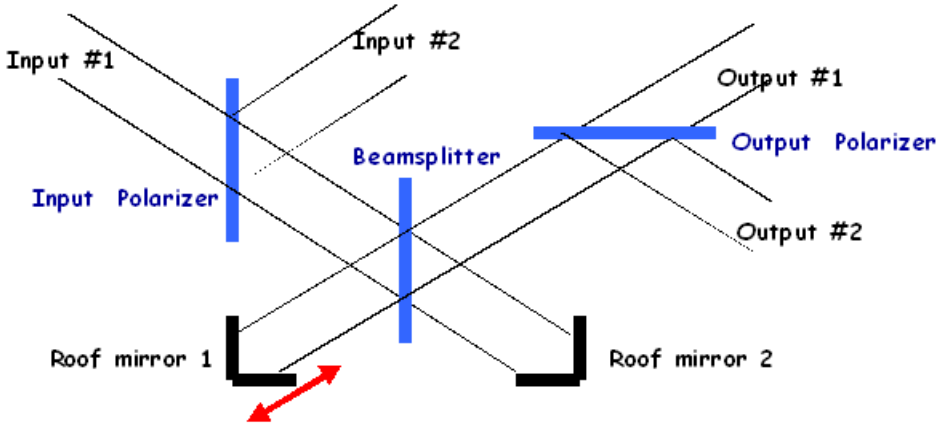

Figure 5.3: Scheme of the optical layout of the differential FTS.

benefit of this design is that it can be easily set up in order to produce a differential measure. This can be done simply with a scheme like the one in figure 5.3. The input polarizer is radiated by two differential fields (for example radiation coming from directions symmetrical with respect to the telescope symmetry axis). Imaging upon it on the two opposite sides, what happens is that during the travel through the instrument one input always suffers an additional reflection (and π radians phase shift) compared to the other field, so that when they are finally superimposed onto the detectors, the modulate dpart of signal is proportional to intensities difference.
Following this fact the idea is then to perform a differential measure, where

one field looks at the source under investigation, while the other field is centered in a blank field close to it, aiming a real time background signal removal for each measurement. The drawback of this strategy is the identification of a efficient map making techniques that enables the true signal map reconstruction from the detected signal differences.

5.4.1 FTS basic perfomances

Whatever the optical configuration of the FTS there are rules that come from the instrument itself.

OPD and sampling

The high resolution band fixes both the maximum OPD that has to be inserted in the spectrometer and the highest sample rate to be used in order to Nyquist sample this high resolution band.
The OPD is given by the relation [41]

$$OPD = \frac{\eta c}{2\delta\nu}, \tag{5.1}$$

where $\eta \sim 1$ is a factor depending on the type of apodization of the signal, c is the speed of light and $\delta\nu$ is the maximum spectral resolution to be achieved. Imposing $\delta\nu_{max} = 1$ GHz (R=740 at 740 GHz) and $\eta = 1$ one gets OPD_{max}=150 mm. Considering a single movable mirror, its stroke should then be 75mm. If a couple of movable (oscillating) roof mirrors is used, then the single mirror stroke is less than 40 mm.
The highest sample rate is fixed by the shortest wavelength to be observed: at 760 GHz frequency the wavelength is λ_{min}=0.4mm, so that the minimum step in the mirror movement in order to at least Nyquist sample this wavelength has to be $d_{min} \leq \frac{\lambda}{2} \sim 200$ μm.
The number of samples per interferogram is then $J = \frac{2OPD_{max}}{d_{min}}$, and after a Fourier transform one gets a number $M = (J-1)/2$ spectral elements.

Beamwidth and resolution

In a two beam interferometer the spectral resolution is limited by the divergence of the beams traveling inside it via the fundamental Jacquinot's

relation [40]

$$R\Omega \leq 2\pi. \tag{5.2}$$

This means that having fixed a given spectral resolution, divergence of a single field propagating in the spectrometer must be controlled at a level higher than the one imposed by eq 5.2. Imposing R=800 one gets $\Omega_{Jacq} \leq 8 \cdot 10^{-3}$sr that means $\theta \sim 3°$.

Starting from this number the minimum size of optical elements of the interferometer can be estimated. Consider a diffraction limited optics at 100 GHz frequency, then from throughput conservation and imposing the maximum available divergency the minimum size of element can be found. Practically one gets

$$\pi D_{min} \Omega_{jacq} = \lambda^2, \tag{5.3}$$

that solved for D_{min} imposing as beam solid angle the Jacquinot's one derived before, gives a minimum dimension $D_{min} \sim 10$ mm. Since the optical elements dimension won't be less than 100 mm to collect all radiation from the telescope field of view, it can be safely said that divergence will be controlled inside the spectrometer at a level high enough ($\theta \sim 1°$) to preserve high resolution observations.

An example of the impact of the mirror's size on divergence is presented in fig 5.4, where the divergence of the half 15 arcmins FOV is computed as a function of the first focusing optical element it strikes in the instrument. The single field divergence is around 1°.

5.4.2 A double FTS instrument

The use of a Martin-Puplett scheme like the standard Michelson one has the disadvantage of having two distinct outputs after the first polarizer: the first output contains the signal transmitted from a sky field and the signal reflected from the symmetrical sky field, the second output contains the other components of the two fields.Each of these outputs has to be used as an input for a FTS. In order not to loose half of the power coming from the sky both these outputs must be used.

A viable solution is to double the instrument, in way similar to [43]. Instead of having a single section with movable roof mirrors that ensures the intro-

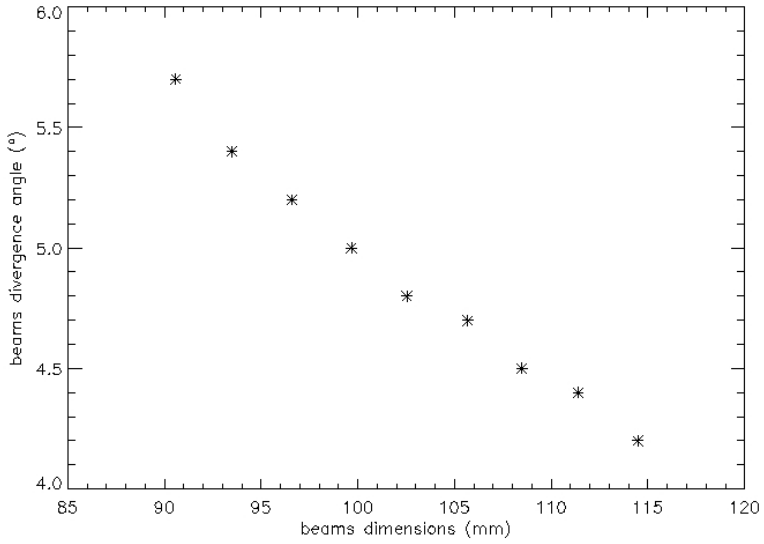

Figure 5.4: Overall beams divergence angle versus the first mirror M1-M2 (see fig. 5.6) aperture size

duction of an optical path difference (and the polarizations rotation), this section has been doubled, each one fed by one of the input grid outputs (sse fig 5.6).

From an optical point of view this solution requires twice the elements needed to build a single spectrometer and in addition a system able to combine the two FTSs outputs in a single beam is needed.

Moreover, due to the energy budget of the satellite and to the big cryostat dimensions that a double drive for the rotating mirrors would induce, a common mechanical system to drive the OPD sections of both the FTSs has to be developed. This offers also the advantage that all the systematics in the instrument due to the drive motion will be the same for both the FTSs and thus the same for both the beams that will be combined before the detection. On the other hand, the room needed to lodge such a system is not much more than the one required for a single FTS. If the FTS is placed in a plane perpendicular to the input plane of the spectrometer, doubling the FTS implies to use just another face of the same solid figure (parallelepiped). Supposing to use the room inside these planes to combine the outputs and detect them, then the required volume won't be much greater than the one

needed for a single FTS.

5.4.3 Input section

The starting point of the instrument, from an optical point of view, is the telescope focal plane. The equivalent focal length of the telescope is $f_{eq} = 9167.33$, the FOV of the instrument is 30'x15', so that the focal plane dimensions are 92 mm x 41 mm. To describe the system a coordinate system with the Z axis coincident with the telescope optical axis, the Y containing the longest side of the FOV is chosen; the input section thus lies in a YZ plane of this reference frame. At this stage a roof mirror (RM in figure 5.6)

Figure 5.5: A scheme of the input FOV of the spectrometer. This coincides with the telescope focal plane.

divides the focal plane in two 15'x15' parts, used as inputs for the differential spectrometer. Because of diffraction effects due to the edge of the roof mirror, with this configuration the very central part of the telescope focal plane won't be usable. Spectrometer inputs are separated by 5' (2.5' for both sides), which is the Airy function FWHM at 100 GHz for the telescope, in order to avoid diffraction by the wedge edge.

In order to symmetrize the divergence behavior of the beams inside one arm of the instrument the central pixel of each array, corresponding to a $\pm$10'(15'/2$\pm$2.5') inclination from the telescope axis, has been selected as principal, central direction of each FTS arm, fixing it as the chief ray for the subsequent ray tracing with ZEMAX [44].

The reflector wedge is inclined so that the beam bending angle is 110°: this angle allows the rim of the following mirrors to stay below the roof edge one. The roof sides are 130mm and 65 mm.

After the FOV division the beam reflects on a couple of paraboloidal mirrors (M1, M2) with equal focal length $f_1 = f_2 = 180$mm. These mirrors have their focus on the $\pm 10'$ telescope pixels, and propagate collimated plane

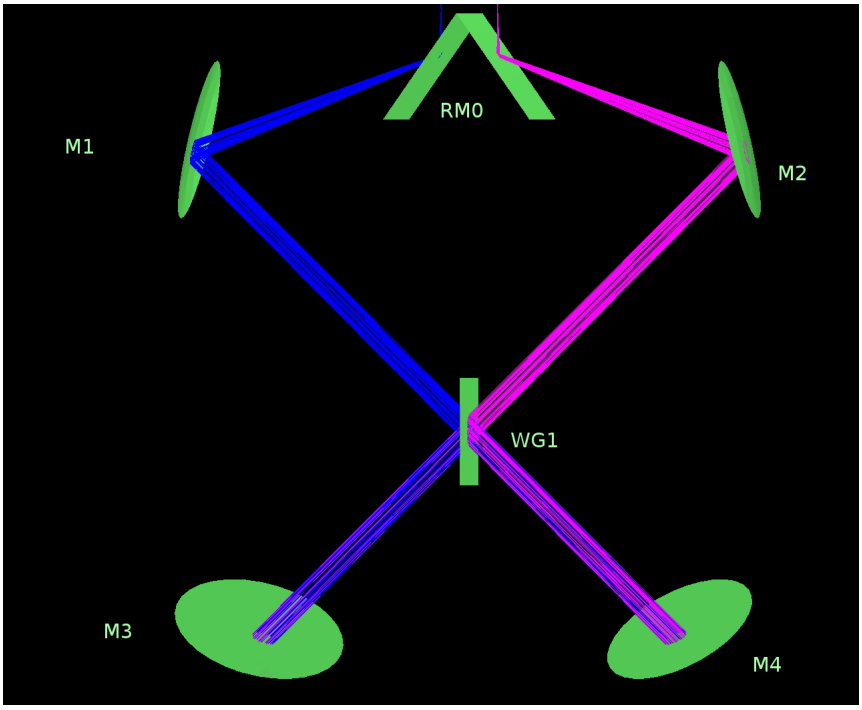

Figure 5.6: Front view of the input section of the spectrometer

waves towards a first polarizer (WG1) whose outputs feed the spectrometers.

The focal length of these mirrors fix the intersections of the beam split by RM with the parent parabolas that define the mirrors. With a focal length of 180 mm the intersection is 210 mm far in the Y direction (horizontal distance between the optical axis and the mirror), increasing the focal length would also increase this distance, increasing the instrument lateral dimension. The bending angle is 60°, so that the reflected beam propagates in a direction 40° tilted with respect to the horizontal. The last part of this section is a couple of paraboloidal mirrors (M3, M4) that transfer the beams to the FTSs, focusing radiation on the wire-grids of each spectrometer.

The use of a focusing element at this stage is required in order to prevent an excessive divergence of the beam and a very large diameter of the wire-grids. Also in this case f_3=f_4=201 mm are limited by dimensions. This focal length is fixed by the distance in X direction we want to place the focus (that is

the position of the FTS wire grid) and therefore defines the instrument dimension in the X direction. The bending angle in the XZ plane is 55°
At first glance it was not obvious to transfer radiation from the telescope to the FTSs with a two couples of parabolic mirrors, in fact one could also use ellipsoidal mirrors, but with this solution the divergence among beams coming from different directions is amplified by the mirror transverse magnification (that showed to be grater than 1).

5.4.4 Optical path difference section

This section of the instrument is made up by two identical FTSs lying in different, parallel XZ planes, orthogonal to the input section plane. Signal focused by mirrors enters two identical two beams interferometers where an identical optical path difference is applied in each interferometer.
The beamsplitters (WG2, WG3 in fig. 5.7) inside the FTS splits the signal focused on it in two beams each containing half of the incoming power. This is done placing their polarization axis 45° tilted with respect to the polarization direction of the incoming radiation.
The split and transmitted beams hit a couple of paraboloidal mirrors (M5,M7-M6,M8) with the same focal length (300 mm), and the focus placed on the wire grid. The plane waves generated by this mirrors are sent to a couple of movable roof mirrors (RM1,RM2-RM3, RM4) that ensure the introduction of the optical path difference and the rotation of 90° of the polarization direction with respect to the incoming radiation polarization.
Beams reflected by the roof mirrors are refocused on the wire-grid: signal that was originally reflected by the grid now crosses it, having its polarization 90° rotated, and viceversa for the beam originally transmitted. Ideally with this scheme 100% of signal is sent towards detectors.
The two FTSs are identical, the only difference is that they lie in different parallel planes. This is essential in order to have the same mechanical tool to drive the roof mirrors to perform the optical path difference.
After the new passage on the wire-grid, signals reflect on another paraboloidal mirrors couple M9, M10 with focus on the wire-grids WG2,WG3 and focal length $f_9 = f_{10} = 182$mm. These mirrors send radiation towards another

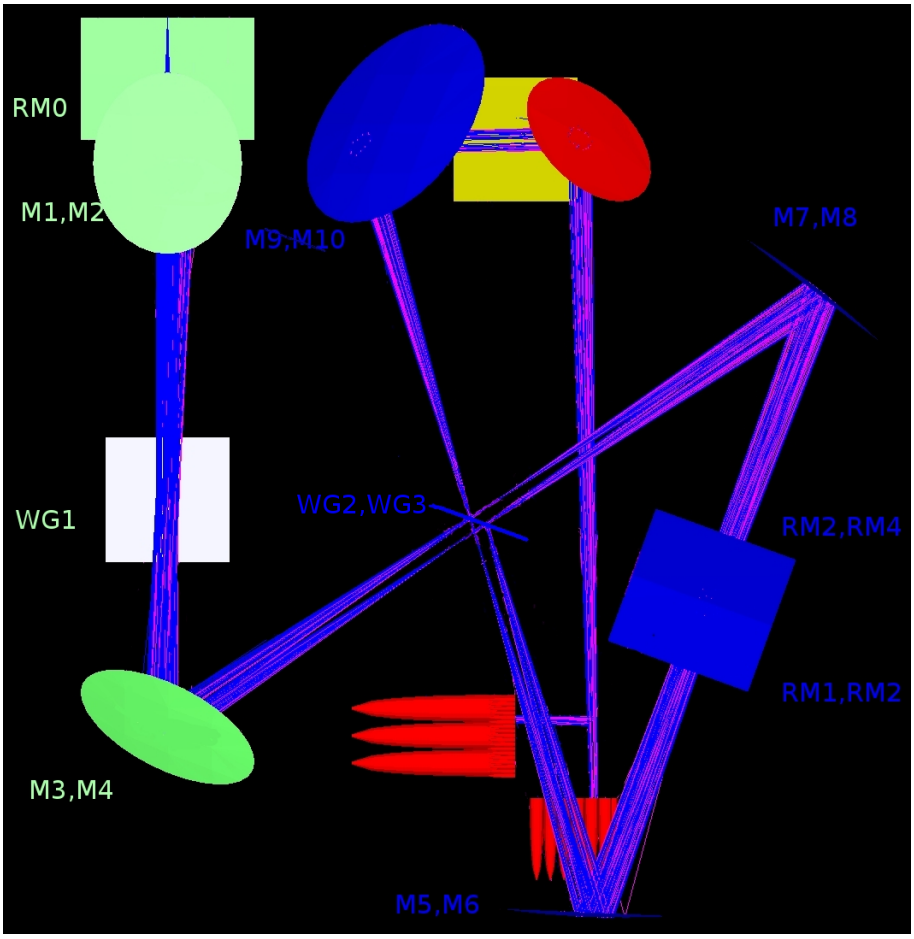

Figure 5.7: Ray tracing of the OPD section common to both the double FTS arms.

common wire-grid, used to combine signals from different FTSs and their focal length is given by the direction of the beam they have to reflect and the height we place them, respecting the limit of not exceeding the RM1 edge. The plane waves generated by these mirrors propagate parallel to the XY plane towards the grid (placed at Y=0) with a 30° angle with respect to the Z axis.

5.4.5 Combining section and signal detection

Once the signal OPD is inserted in the FTSs sections, the FTS outputs must be superimposed in order to use for the detection all the power available collected by the telescope.

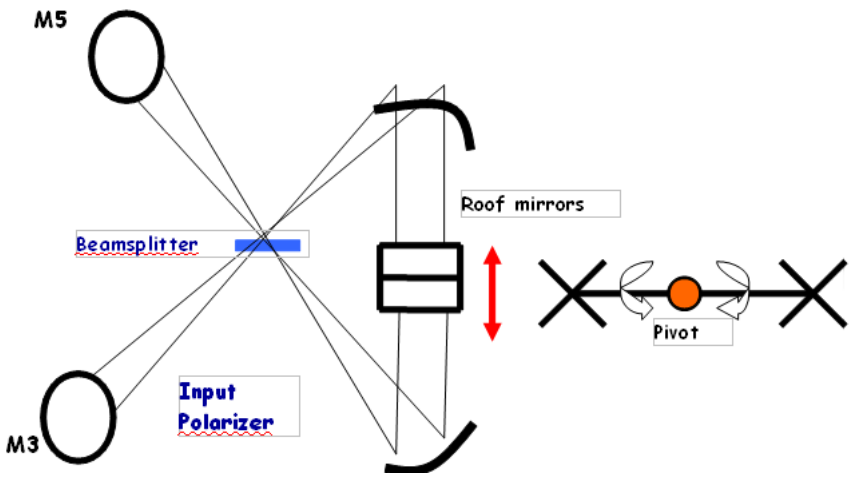

Figure 5.8: Scheme of the OPD section common to both the double FTS arms.

A common wire-grid (figure 5.9) placed in Y=0 and lying in a XZ plane is used to combine the outputs of the FTSs, that have opposite sign (additional π phase shift) since their inputs are of opposite sign. The role of the wire grid is to provide two beams with the same sky signal difference and the same direction. Signals are sent to the polarizer with the mirror couple M9,M10. The difference sign problem is resolved by the grid considering that it couples one beam in transmission with the other in reflection (that gets a π phase shift).

The recombination must also respect the directions of pixels coming from the two parts of the FOV divided on the telescope focal plane, in order to be superimposed on the detector plane to build a differential map. This is done if the two FTS are identical and their outputs are symmetrical with respect to the grid plane.

The signal is then sent to the detectors with a couple of paraboloidal mirrors M11, M12 (f_{11} = f_{12}=250 mm). On the mirrors focal plane lies an array of Winston cones that collects radiation and send it to the bolometers. The focal planes have a dimension of 66 mm x 66 mm, corresponding to a 15'x15' FOV (the spectrometers field input are now superimposed), that is the overall plate scale of the system is 13.6"/mm.

From these values Winston's cones [45] parameters can be calculated. At

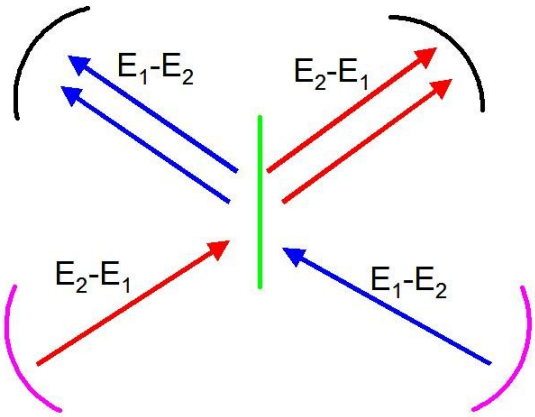

Figure 5.9: Scheme (top view) of the recombination of the FTS outputs (blue and red arrows) with a common wire grid

100GHz the array is 3x3, that is 5' per pixel, corresponding to a linear dimension of 2R=22mm. This is the Winston's cone input aperture. The output aperture can be find using the throughput conservation, using as solid angle the solid angle ($\pi\theta^2$, θ=5.2°) of the beam been refocused by the last parabolic mirrors M11,M12. We find an output diameter $2r$=2mm.
The cone length is given by $L = (R + r)/tan(\theta)$=132 mm. Considering that the pixels number in the other frequency bands is given considering the wavelength ratio with respect to 3.0 mm (100 GHz-200 GHz), the other arrays will be respectively 6x6 (200 GHz-300 GHz), 9x9 (300 GHz-450 GHz) and 18x18 (700 GHz-740 GHz). In the same way the Winston's cones (reported in table 5.2) for the other frequencies are downsized with the same ratios.
A couple of dichroic filters is inserted 50 mm before the focal plane to ensure

Frequency band	R (mm)	r (mm)	L (mm)
100 GHz-200 GHz	11	1	132
200 GHz-300 GHz	5.5	0.5	66
300 GHz-450 GHz	3.65	0.34	44
720 GHz-760 GHz	1.8	0.17	22

Table 5.2: Winston's cones parameters for the four detectors arrays of the instrument

the band splitting defined for the instrument. A complete 3D ray tracing of

the instrument is presented in figure 5.10.

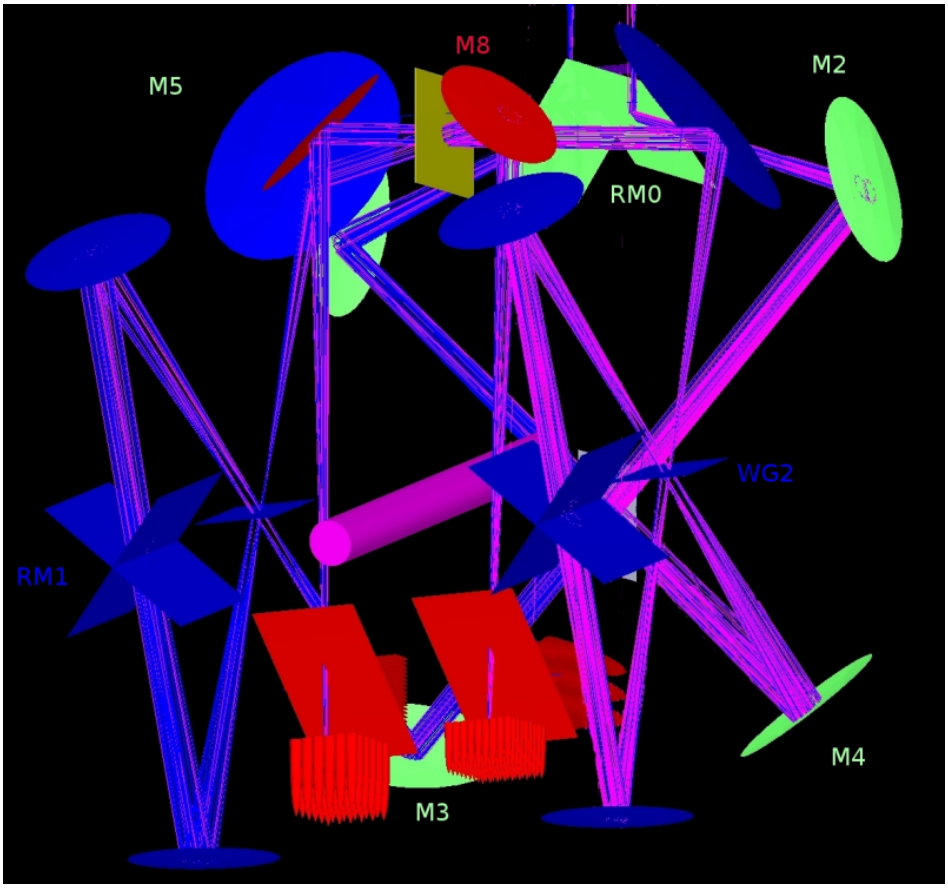

Figure 5.10: Ray tracing of complete FTS.

5.4.6 Lyot stop positioning

In order to minimize the spillover contribution of the telescope without underilluminating it, a Lyot stop (LS) inside the FTS has to be placed. The great advantage to locate the LS inside the spectrometer is that it would be cold, reducing the load on detectors with respect to a warm (100K) stop placed outside the cryostat

On the other hand, placing it inside the spectrometer is not trivial from an optical point of view. Physically the LS is one of the optical element of the chain leading signal from the telescope focal plane to the detectors and has the function of an aperture stop.

The LS could be placed before the OPD section, and in this way it will coincide with a well defined image of the telescope subreflector (telescope aperture stop) but then the detectors (placed after the OPD section) would see its image made by the following optical elements changing both in shape and dimension during the interferogram because of the roof mirrors oscillation.
On the other hand, placing the stop after the movable mirrors would have the advantage of having a well defined image of this stop on the detectors but the LS would see the image of the subreflector changing in shape and dimension always because of the movable mirrors. In this second case the problem of seeing the subreflector image changing during the interferogram is less critical than having the stop image on the detectors changing, because the distance between the subreflector and the LS would be much greater than the distance between the LS and the detectors. For this reason the effect of a changing image, which is something intrinsic in a FTS, is less worrisome. Furthermore, placing the LS after the OPD section offers the possibility of using the combining wire grid WG4 as stop, realizing a stop common to both the instrument arms.
As explained in the previous sections the focal lengths f_1, f_3 cannot be changed because they are strictly related to the room that the FTS takes up; also f_9 is almost fixed.
By the way, the focal length of the paraboloidal couple inside the FTSs is more relaxed (because the only limitation is to have a focal length great enough in order to avoid shadowing of the beam by the movable roof mirrors).
With this scheme, imposing the LS to be lying on the combining wire grid, an analytical expression for this focal length value can be derived.
The LS must coincide with an image of the telescope subreflector: it will be the aperture stop for the optical elements following it, and therefore the entrance pupil. Consider an optical chain made up by 5 focusing elements, that is M1, M4, M6, M8, M10; this is equivalent to the chain of the spectrometer because the effect of the roof mirrors, being placed at half the distance among M6 and M8, is to place after the reflection onto them the entrance pupil of M6 (for the second reflection on it) at a distance which is the same

as the distance between M8 and the previous exit pupil of M6. Because M8 and M6 are identical this is the same than considering the propagation through M6 instead of considering the reflection of the roofs.
Since f_1, f_4 are almost fixed by the dimensions of the FTS, the pupil is propagated until M4, and the pupil output distance from M4 is used as the starting point for the analytical determination of $f_6 = f_8$ needed to have the LS on the combining wire grid, that is d_{out10}=distance among M10 and the grid.
Since the entrance pupil of an optical element is the exit pupil of the previous one $d_{in6} = l - d_{out4}$, where l is the optical path between M4 and M6. In the same way $d_{in8} = h - d_{out6}$, where h is the optical path between M6 and M8 and $d_{in10} = t - d_{out8}$, where t is the optical path between M8 and M10. The condition is $d_{out10} = d$, where d is the distance between the grid and M10. Using the thin lens formula we have:

$$d_{out10} = \frac{f_{10} d_{in10}}{d_{in10} - f_{10}}. \tag{5.4}$$

Recalling that

$$d_{in10} = t - d_{out8} = t - \frac{f_6 d_{in8}}{d_{in8} - f_6} \tag{5.5}$$

$$d_{in8} = h - d_{out6} = h - \frac{f_6 d_{in6}}{d_{in6} - f_6} \tag{5.6}$$

and that h, t, din_6 are fixed, substituting the last two relations in 5.4 and imposing this distance to be equal d, a second order relation in f_6 that has a real root $f_6 = f_8$=231 mm is found.
There are other viable solutions for the LS position.
With the same argument it can be imposed to place the LS everywhere after M9-M10: a good alternative to the wire grid could be M9-M10. The advantage to have a mirror instead of a grid as a stop is that the mirror rim is well defined while in the case of a grid there is the problem to define a structure that carries the wires and that must not reflect radiation in order to work as a stop. Imposing $dout_{10}$=0 we find f_6=411 mm.
The layout presented in this document has f_6=300 mm; with this configuration the subreflector image lies 50 mm after the grid, in the space between WG4 and M11-M12. A possibility would be inserting in these positions a true couple of diaphragms for the beams propagating towards M11-M12.

5.4.7 Mirrors dimensions

Mirrors dimensions have been chosen in order not to loose energy carried by the beam: this was done with the ZEMAX Non-Sequential-Component "detectors" tool.
As an example the dimensions needed in some key points of the instrument to satisfy this criterion are computed. A complete list of the mirrors dimensions is showed in table 5.3.

Optical element	D (mm)
RM1	120x70
M1,M2	140
WG1	130
M3,M4	180
WG2, WG3	90
M5,M6,M7,M8	130
M9,M10	80x120
WG4	140
M11,M12	120

Table 5.3: Dimensions of the optical elements of the spectrometer

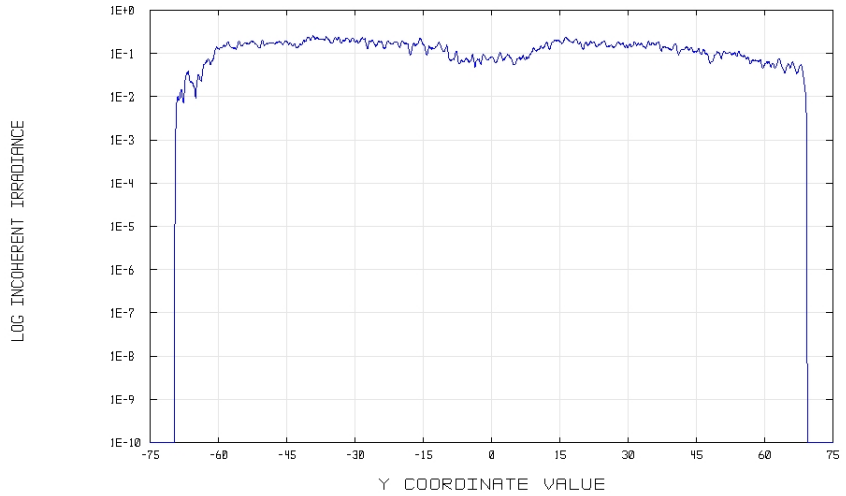

Figure 5.11: Overall beam dimensions on the first polarizers(mm) vs the irradiance (w/cm^2) carried by the beam

All the mirrors will be realized from an aluminum alloy. The same mate-

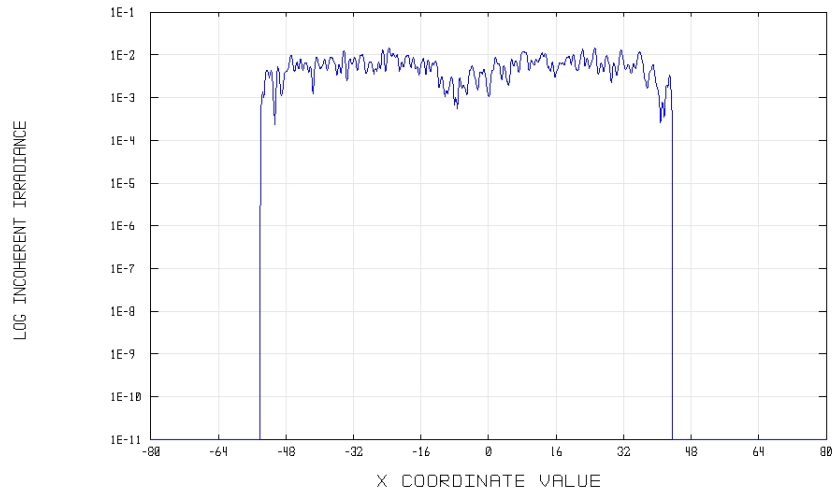

Figure 5.12: Overall beam dimensions after the reflection on M5,M6,M7,M8(mm) vs the irradiance (w/cm^2) carried by the beam

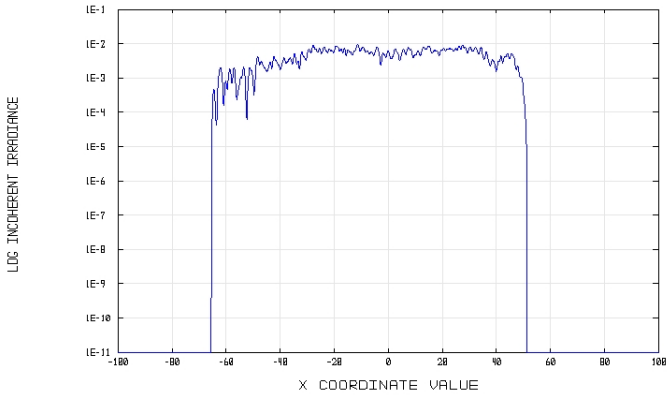

Figure 5.13: Overall beam dimensions (mm) on the combining grid vs the irradiance (w/cm^2) carried by the beam

rial will be used for the supporting structure, in order to prevent differential displacements in the optics when cooled down to cryogenic temperatures. The mirror shape will be realized by using a milling machine which can provide an accuracy up to 10-20 μm. The surface of the optics will be also lapped for alignment purposes. The wire grids are commercial devices and can be provided with the appropriate shape and dimension of the mounting frame, and with the appropriate thickness and spacing of the wires. The

metal wires are then gold coated to minimize the absorption losses. In front of the detectors two high-pass (or low-pass) dichroic filters [42] are used to split the radiation, and after them four band-pass dichroic filters, used to define the frequency band of each array. All these dichroic filters have been already used in a large number of experiments and also operated in space.

5.4.8 The moving roof mirrors

OPD in the FTSs is inserted by oscillating a couple of roof mirrors, realizing a pendulum. This system presents many advantages with respect to the usual linear translation of a single roof mirror, as presented in the original work by Martin and Pupplett.

From the optical and mechanical point of view this layout enables to reduce by a factor 2 the mirrors stroke (for a given OPD) with respect to the single mirror displacement case.

Roof mirrors rotation can be realized with a resonant oscillation around a pivot. This solution minimizes the power dissipation, which is a crucial aspect of the system being placed in a cryogenic environment. This technological solution has been already developed and has been already used in space missions like SPIRE for the Herschel SPIRE [46] mission. The mirror movement has to be done in the beam direction of propagation. This requirement fixes position and radius of the pendulum.

The mirror stroke needed to achieve the required resolution in case of high spectral resolution interferograms ($\delta\nu = 1$ GHz), taking into account the efficiency of sampling and a possible apodization, is $\Delta x \approx 2.75$ cm, symmetric respect to the zero path difference, corresponding to $\pm$ 18 cm of maximum optical path difference. The angular oscillation required to recover this stroke in the proposed layout is about $\pm$ 13° from the equilibrium (the distance between the beam axis and the rotation axis is $\sim$ 20 cm). This translates into maximum lateral displacement of the roof mirrors which is $\Delta y \sim 5.1$ mm. The situation for low resolution interferograms ($\delta\nu = 20$ GHz) is much different: the OPD required is 9 mm, that corresponds to a 0.65° rotation, leading to translations Δx=4.5 mm, Δy=0.012 mm.

The oscillation is performed around an axis where a flex pivot s placed. Ball bearings have been avoided in order to prevent losses due to the fric-

tion. Flex pivot are in fact practically frictionless devices. The design of the mechanical mount of the roof mirrors is shown in figure 5.14. The inertial

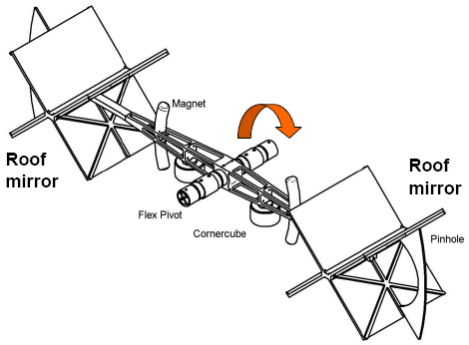

Figure 5.14: Design of the roof mirrors embedded in their mechanical drive.

momentum of the system around the pivot axis is 0.150 kg m^2. The mass of the pendulum is 1.8 kg.

Taking into account the angular excursion necessary to get the spectral resolution and the oscillation period, that has to be of the order of 10 s, Riverhawk flex pivots of the series 400 and 600 suit these requirements (see www.flexpivots.com). Riverhawk has produced flex pivots already successfully used on COBE, ISO e SPITZER. Flex pivots will be mounted in multiple configuration (a couple of 2 or 3 stacked pivots) in order to distribute the angular displacement and to operate them in a condition of endless lifetime. The torsion constant of the selected pivots is in the range $k = 0.004 \div 0.09$ (m-kg)/deg (table 5.4) and the range of the period of oscillation is T $\sim$ 5.8 $\div$26 s. The applied radial load in the present configuration is of few % of the capacity. Here some option is presented, but if necessary specific values of the torsion constant can be required. The energy necessary to the oscillation can be provided by a Voice Coil magnetic motor made by Samarium-Cobalt already used in Spitzer (www.beikimco.com). We can use a superconductive coil as a fixed element and the magnetic gap as mobile element. The motors must provide the energy dissipated by the friction. The motors will be turned on only for a small time interval ($\sim$ 1% of an oscillation) and only when the amplitude of oscillation is reduced by 1%.

These motors can be also used as blockage system during the lift-off opera-

Model	k (m-kg)/deg	T (s)
5012-400	0.004	25.87
5024-600	0.005	25.411
5016-400	0.01	16.824
5020-400	0.021	11.786
5032-600	0.011	16.544
5024-400	0.037	8.99
50324-400	0.087	5.846

Table 5.4: Fundamental parameters of various RiverHawk flex pivots.

tion up to the positioning in the operation orbit. This solution allow us to avoid a mechanical blockage system which could be a potential single failure point.

Bibliography

[1] Penzias, A. A., Wilson, R. W., 1965, *"A Measurement of Excess Antenna Temperature at 4080 Mc/s."* APJ, **142**,419-421

[2] Mather, J.C., et al., 1993, *"Design for the COBE Far Infrared Absolute Spectrophotometer (FIRAS)"* Proc. SPIE, **2019**, 168.

[3] Fixsen, D.J., 1996, *"The Cosmic Microwave Background spectrum from the full COBe data set"* APJ, **473**, 576

[4] Sunyaev, R.A., 1980, *"The microwave background radiation in the direction toward clusters of galaxies"* Sov. Astron. Lett. **6**(4)

[5] J.A.S. Lima, A.I. Silva and S.M. Viegas, 2000, *"Is the radiation temperature-redshift relation of the standard cosmology in accordance with the data?"* Mon. Not. R. Astron. Soc. **312** 747

[6] Luzzi, G., Shimon, M., Lamagna, L., Rephaeli, Y., De Petris, M., Conte, A., De Gregori S., Battistelli, E. S., 2009, *"Redshift Dependence of the CMB Temperature from S-Z Measurements"* ArXiv e-prints, Accepted for pubblication in APJ.

[7] Hinshaw, G., 2009 *"Five-Year Wilkinson Microwave Anisotropy Probe Observations: Data Processing, Sky Maps, and Basic Results"* ApJs, **180** 225-245

[8] Nolta., M.R., 2009, *"Five-Year Wilkinson Microwave Anisotropy Probe Observations: Angular Power Spectra"*, ApJs, **180**, 296-305.

[9] Hu, W. and White, M., 1997 *"A CMB polarization primer"* New Astrononomy Review, **2**, 323-344.

[10] Hu, W., 2008 *"Lecture Notes on CMB Theory: From Nucleosynthesis to Recombination"*, ArXiv e-prints, to appear in XIX Canary Island Winter School of Astrophysics, ed. R. Rebelo and J.A. Rubino-Martin.

[11] Page, L., 2007 *Three-Year Wilkinson Microwave Anisotropy Probe (WMAP) Observations: Polarization Analysis*, ApJs, **170** 225-376.

[12] Thomson, A., R., Swenson, J., M., Moran, G., W., 2001, *"Interferometry and synthesis in radio astronomy"* Wiley

[13] Dunkley, J., 2009 *"Five-Year Wilkinson Microwave Anisotropy Probe Observations: Likelihoods and Parameters from the WMAP Data"* ApJs, **180**, 306-329.

[14] Destri, C. de Vega, H. J. Sanchez, N. G., 2008, *"MonteCarlo Markov chains analysis of WMAP3 and SDSS data points to broken symmetry inflaton potentials and provides a lower bound on the tensor to scalar ratio"* PRD **4**, 043509-+

[15] Lewis, A., Challinor, A., 2006, *"Weak lensing of the CMB"* Physics Reports, **429**, 1, 1-65

[16] Born, M., Wolf., E., *"Princples of optics"* Cambridge University Press 1999.

[17] Sharma., K., K., ''Optics, principles and applications Academic Press 2006.

[18] Charlassier, R., et al., 2009 *"An efficient phase-shifting scheme for bolometric additive interferometry"* A&A **497** 963-971.

[19] Martin, D. H. and Puplett, E., 1970, *"Polarised interferometric spectrometry for the millimeter and submillimeter spectrum"* Infrared Physics, **10**, 105-109.

[20] Polenta, G, et al., 2007 *"The BRaIn Exxperiment"* Proceedings of the XI Marcell Grossman meeting

[21] Charlassier, R., 2008, *"The QUBIC experiment"* Proc. of Moriond meeeting.

[22] Pozar, D., M., *"Microwave Engineering 2nd Edition"*, 1998, J. Wiley & Sons.

[23] Bunn, E.,F., 2007, *"Systematic effects in CMB interferometry experiments"* PrD **75**, 8, 083517-+.

[24] Sharma., K., K., *"Optics, principles and applications* Academic Press 2006.

[25] HalversonN, W., et al., 1998, *"DASI: Degree Angular Scale Interferometer for imaging anisotropy in the cosmic microwave background"*, SPIE **3357** 416-423.

[26] Cartwright, J. K., 2001 *"Polarization Observations with the Cosmic Background Imager"* Bulletin of the American Astronomical Society, **33** 816-+.

[27] Mather J. C., 1984 *"Bolometers: ultimate sensitivity, optimization, and amplifier coupling"* AO, **23** 584-588.

[28] Tucker, G. S., et al., 2008, *"The millimeter-wave bolometric interferometer (MBI)"*, SPIE **7020**.

[29] Labeyrie A., *"Optical stellar interferometry"* Cambridge University Press, 2006

[30] Castro, P. G, et al., 2009 *"Cosmological Parameters from the QUAD CMB Polarization Experiment"* ApJ, **701**,857-864

[31] Kovac, J.M., 2002, *"Detection of polarization in the cosmic microwave background using DASI"*, Nature, **42**, 772-787.

[32] Charlassier, R., et al., 2009 *"Bandwidth in bolometric interferometry"*, submitted to A&A.

[33] V. Mahajan, *"Optical Imaging and aberrations, Part I, Geometrical Optics"*, SPIE Press, 2001

[34] V. Mahajan, *" Optical Imaging and aberrations, Part II, Wave diffraction Optics"*, SPIE Press, 2001

[35] J. Goodman, *"Introduction to Fourier Optics"*, McGraw-Hill, 1996

[36] Hamilton, J., C., et al., 2008, *"Sensitivity of a bolometric interferometer to the cosmic microwave backgroud power spectrum"* A&A **491** 923-927.

[37] Charlassier, R., et al., 2009, *"An efficient phase-shifting scheme for bolometric additive interferometry"* A&A **497** 963-971.

[38] Woody, D., 2001, *"Radio interferometer array Point Spread Functions"* Alma Memo 389

[39] Zmuidzinas J., 1998, *"Progress in Coherent Detection Methods"* http://www.submm.caltech.edu/ jonas/tex/papers/pdf/1998-Zermatt-Zmuidzinas.pdf

[40] Jacquinot, P., 1960, *"New developments in interference spectroscopy"*, Reports on Progress in Physics, **23**, 267-312.

[41] Bell R., J., 1972, *"Introductory Fourier Transform Spectroscopy"*, Academic Press.

[42] Goldsmith P. F., 1998, *"Quasioptical systems"* SPIE press

[43] B. Carli, F. Mencaraglia, 1981, *"Signal doubling in the Martin-Puplett interferometer"* Intenational Journal of Infrared and mm waves, **2**, 5.

[44] ZEMAX, Optima Research Inc.

[45] Welford, W.T. and Winston, R., 1989, *"High collection nonimaging optics"* New York: Academic Press.

[46] Schulz, B., et al., 2007, *"The Spectral And Photometric Imaging Receiver For Herschel (SPIRE)"*,Bulletin of the American Astronomical Society, **38**, 108-+.

Appendix A

Pictures of the various DIBo Measurements

Figure A.1: Picture of the experimental setup for MVNA phase shifter measurements.

Figure A.2: Picture of the experimental setup for MVNA hybrid ring measurements.

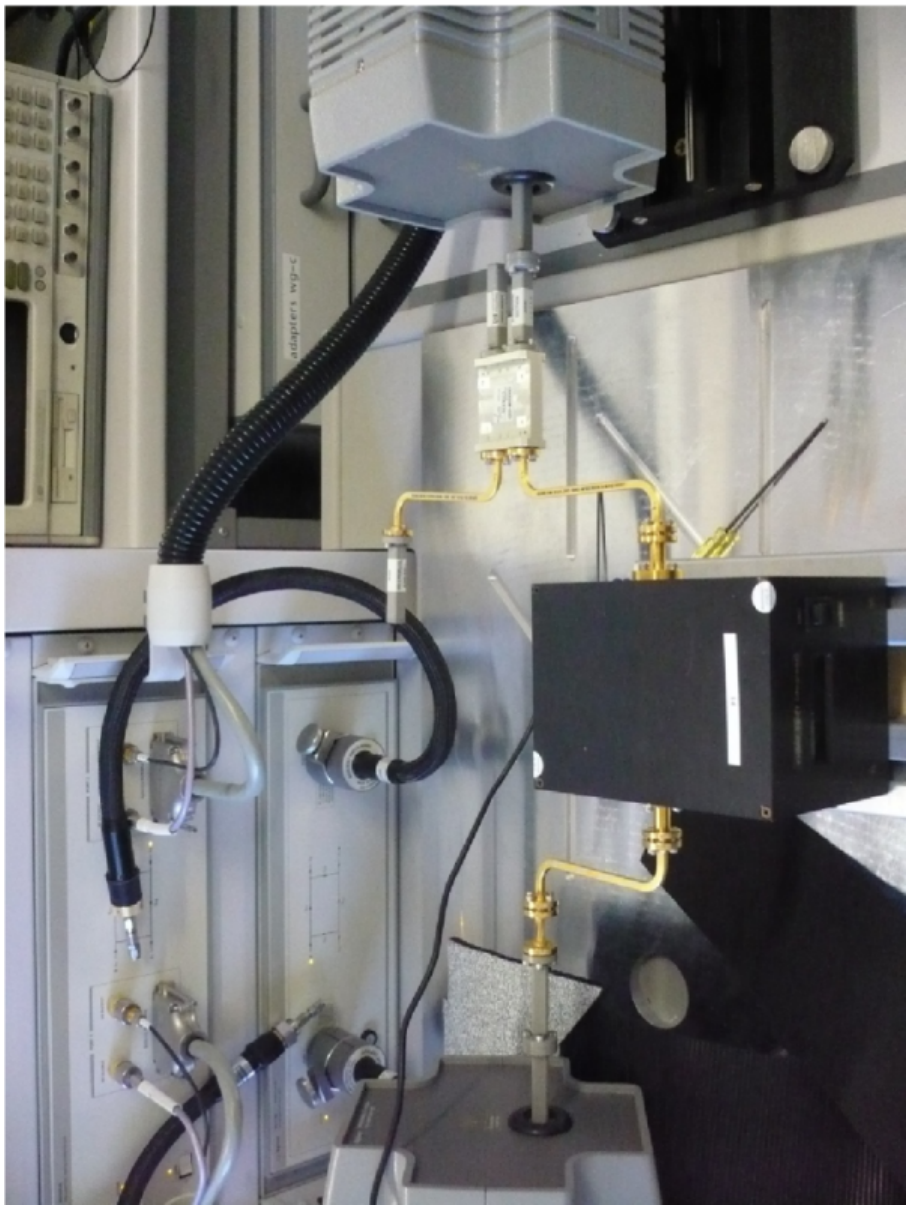

Figure A.3: Picture of the experimental setup for MVNA full arm measurements.

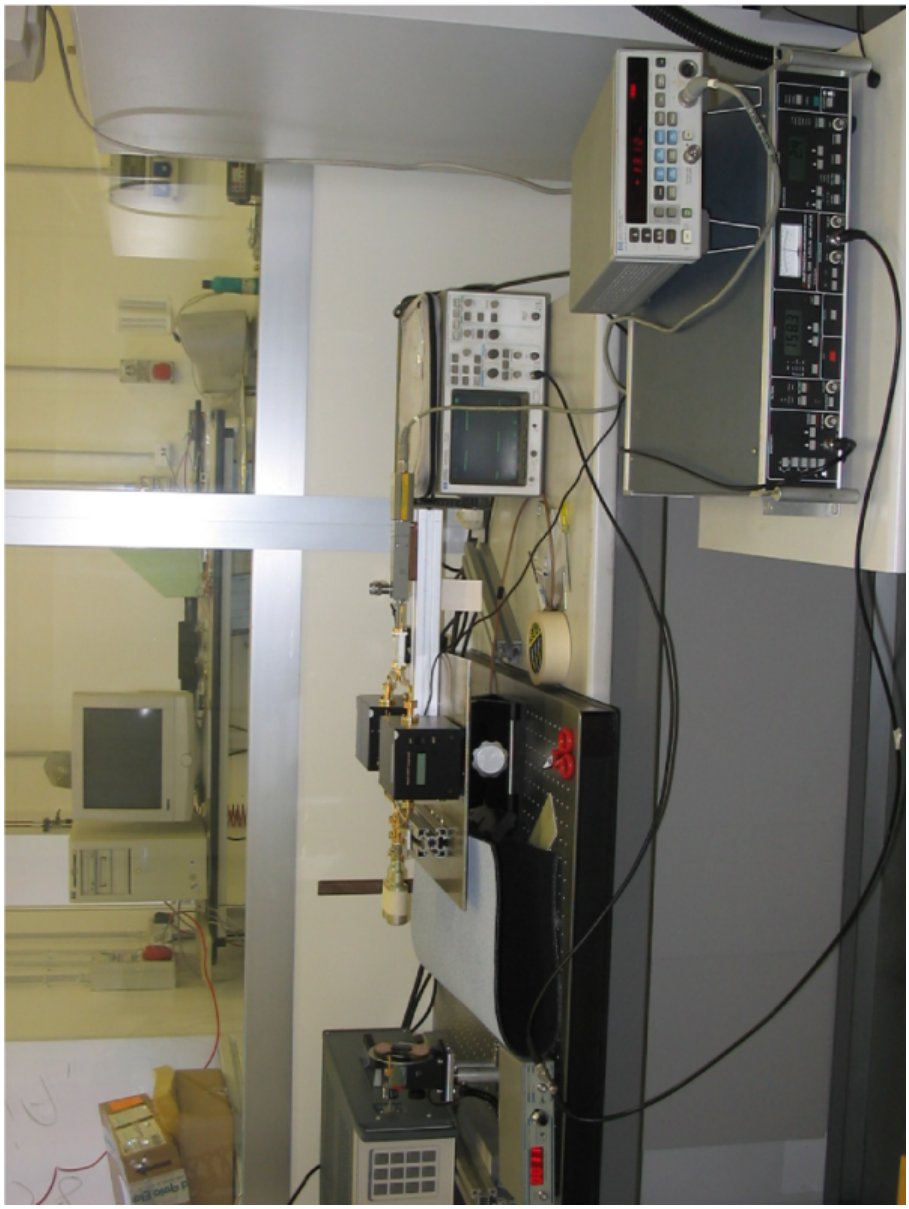

Figure A.4: Picture of the experimental setup for large bandwidth measurements.

Appendix B

Design of off-axis Gregorian and Cassegrain telescopes

A first attempt for the design of the combiner optical layout can be done considering classical telescopes layouts like Cassegrains and Gregorians. The idea is to fit them in a dimension roughly less than 1m^3 to be lodged in a cryostat, and then impose the equivalent focal length f_{eq} to be in the range 200 mm-300 mm. An important requirement for the design is the use of off-axis systems, given the big L ∼240mm dimension of the back horns array that would shadow beams reflected by the primary mirror.

Consider a Gregorian system like the one in figure B.1, where the back horns array lies at an height h from the primary mirror. Let φ be the system bending angle and $k = \dfrac{R_2}{R_1}$ the secondary mirror magnification. Finally, it's supposed that the secondary mirror exit focus F_2 lies at an horizontal distance lh with respect to the point P and that $R_2 = sh$, where l, s are arbitrary proportionality constants. With these choices the system is fixed, and the primary mirror focal length can be derived considering that the total horizontal length has to be equal to lh, and recalling that $PF_1 = \dfrac{2f_p}{1+\cos\varphi}$:

$$PF_1 \sin\varphi + F_1 Q \sin\varphi = lh \tag{B.1}$$

$$\frac{2f_p \sin\varphi}{1+\sin\varphi} + \frac{R_2}{k}\sin\varphi = lh \tag{B.2}$$

$$f_p = h\frac{1+\cos\varphi}{2\sin\varphi}\left(l - \frac{s}{k}\sin\varphi\right). \tag{B.3}$$

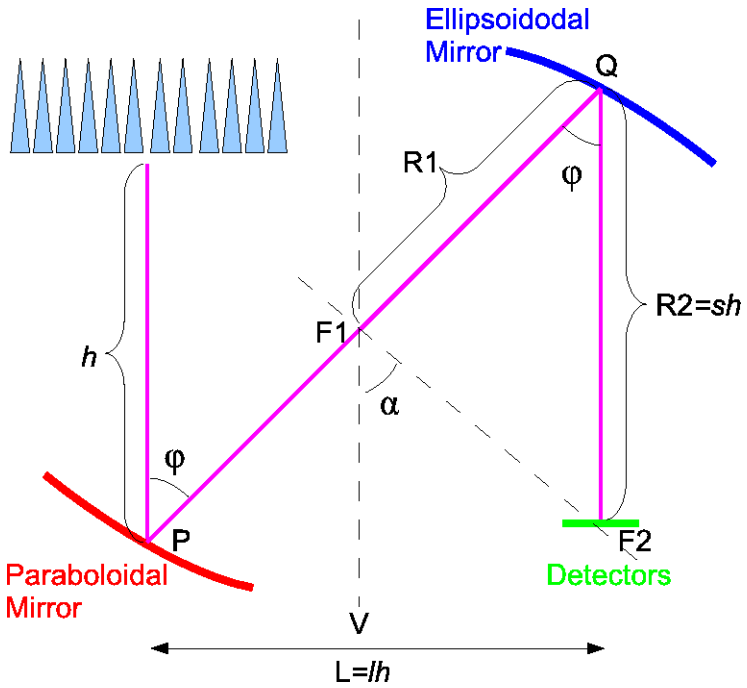

Figure B.1: A sketch of the considered system geometry for a gregorian system

The equivalent focal length of the system is given by

$$f_{eq} = f_p m_0 \frac{1 + \tan^2 \alpha/2}{1 + m_0^2 \tan^2 \alpha/2} \tag{B.4}$$

where $m_0 = \dfrac{e+1}{e-1}$ and α is the angle between the two mirrors symmetry axis.

The eccentricity of the secondary mirror can be derived as follows. The ellipse symmetry axis is the line connecting F_1 to F_2, and the distance among these point is by definition equal $2c$, where c is the ellipse foci coordinate with respect to its symmetry center. This distance can be estimated using Carnot's theorem:

$$2c = \sqrt{R_1^2 + R_2^2 - 2R_1 R_2 \cos\varphi} \tag{B.5}$$

$$2c = \sqrt{\left(\frac{sh}{k}\right)^2 + (sh)^2 - 2\frac{(sh)^2}{k}\cos\varphi} \tag{B.6}$$

$$2c = sh\sqrt{\left(\frac{1}{k}\right)^2 + 1 - \frac{1}{k}\cos\varphi}. \tag{B.7}$$

On the other hand, by definition the sum of the distances of point Q from the two foci is $2a$ and equals:

$$2a = R_1 + R_2 = sh + sh/k = sh\frac{k+1}{k}. \tag{B.8}$$

Recalling the eccentricity definition $e = \frac{c}{a}$, one finally gets:

$$e = \frac{\sqrt{1+k^2-2k\cos\varphi}}{1+k}. \tag{B.9}$$

The angle α between the symmetry axes of the two mirrors can be estimated with the sines theorem; noticing that $\alpha = F_1\widehat{F_2}Q$ and applying sines theorem one has:

$$\frac{R_1}{\sin\alpha} = \frac{F_1F_2}{\sin\varphi} \tag{B.10}$$

$$\sin\alpha = \frac{R_1\sin\varphi}{2c} \tag{B.11}$$

$$\sin\alpha = \frac{sh\sin\varphi}{k}\frac{1}{sh\sqrt{k^2+1-2k\cos\varphi}} \tag{B.12}$$

$$\alpha = \arcsin\left(\frac{k\sin\varphi}{\sqrt{1+k^2-2k\cos\varphi}}\right). \tag{B.13}$$

Plots of the dependance of the system equivalent focal length as a function of the bending angle φ and the secondary mirror magnification k are presented in figs. B.2, B.3. As expected, the equivalent focal length is negative for a Gregorian telescope and its absolute value increases increasing k. On the other hand, increasing the bending angle f_{eq} decreases in modulus.
The equivalent focal length modulus is inversely proportional with respect to c and directly proportional to l.
Imposing the focal length to be in the range 200mm$\div$300mm and by choosing $h \leq 500$ to save room in the cryostat proper values for k, φ, c,l can be derived.

B.0.9 Cutoff frequency in a Cassegrain combiner

Consider a Cassegrain system where the back horns array lies at an height h from the primary mirror. Let φ be the system bending angle and k the secondary mirror magnification. Finally, it's supposed that the secondary

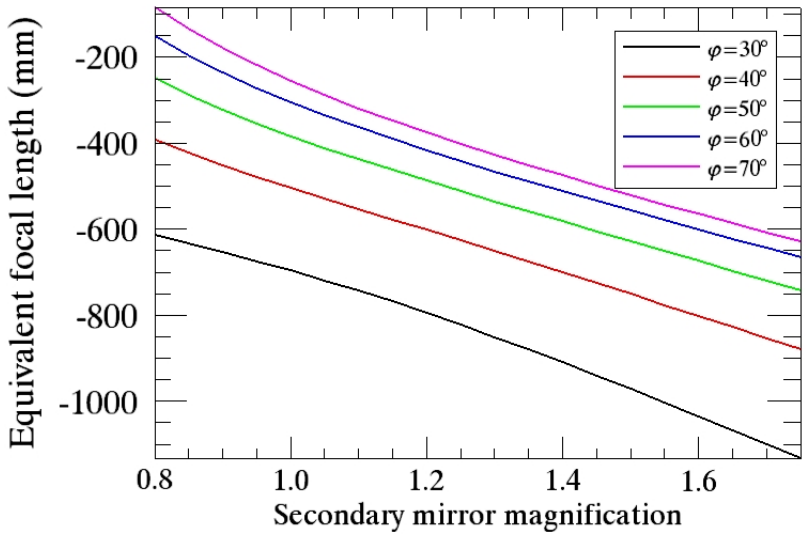

Figure B.2: Equivalent focal length of the Gregorian combiner described in fig. B.1 as a function of the secondary mirror magnification k and of the bending angle φ (various color).

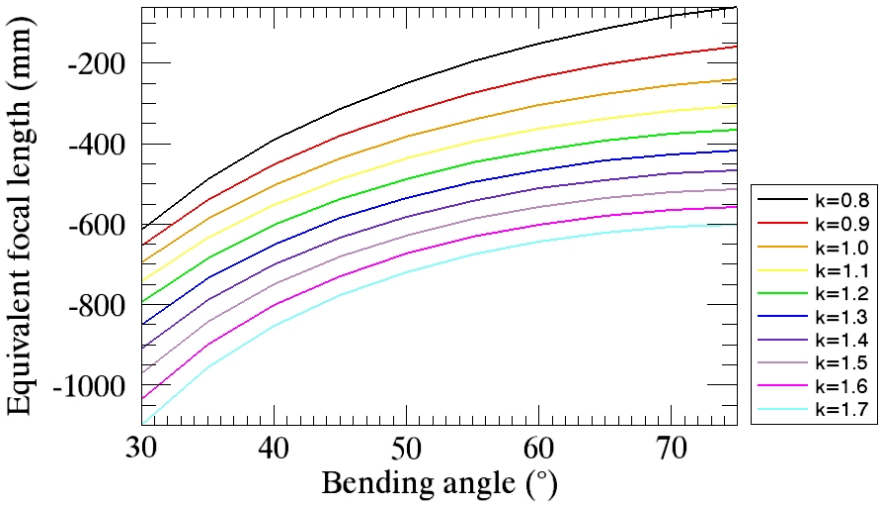

Figure B.3: Equivalent focal length of the Gregorian combiner described in fig. B.1 as a function of the system bending angle φ and of the secondary mirror magnification k (various color).

(hyperboloidal) mirror has $R_2 = sh$ and that the secondary mirror exit focus F_2 lies at an horizontal distance lh with respect to the point P. This geometry is the Cassegrain analogue (that is with an hyperboloid as sec-

ondary mirror instead of an ellipsoid) of the Gregorian case in fig B.1 and is showed in fig B.4. Referring to this figure, according to the hyperbola

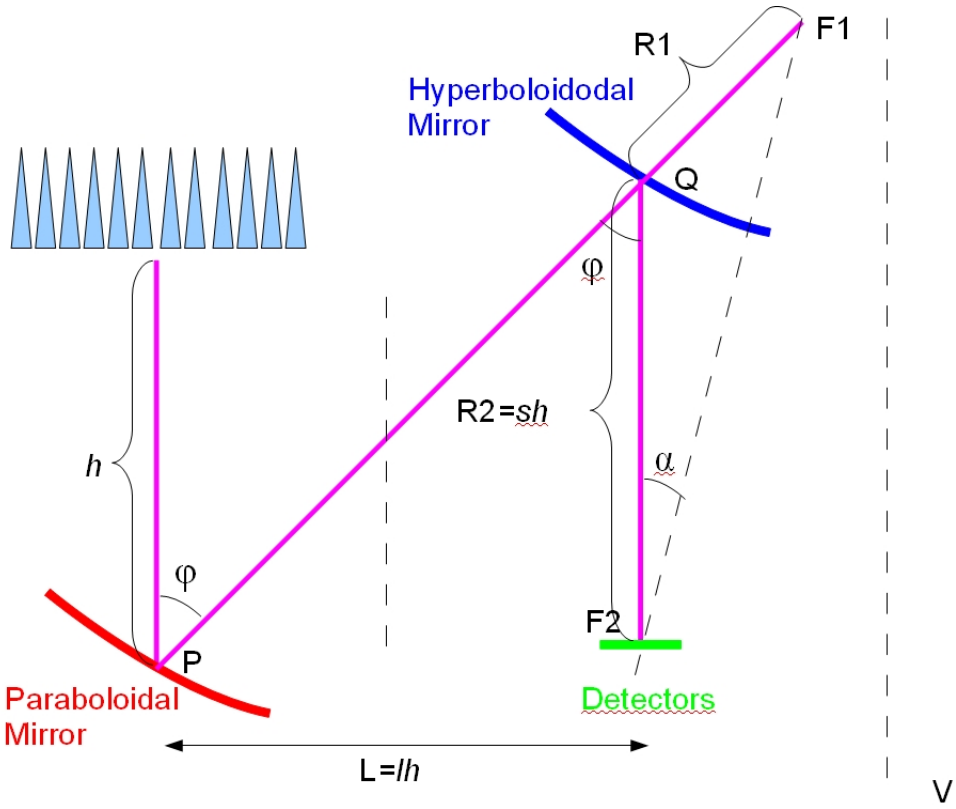

Figure B.4: A sketch of the considered system geometry for a Cassegrain system

definition one has:

$$F_2Q - F_1Q = 2a = sh - \frac{sh}{k} = sh\frac{k-1}{k}. \tag{B.14}$$

Using to Carnot's theorem in the same triangle F_2F_1Q an expression for the foci separation $2c$ is found:

$$2c = \sqrt{(F_2Q)^2 + (F_1Q)^2 - 2F_1QF_2Q\cos(\pi - \varphi)} = sh\sqrt{1 + \frac{1}{k} + \frac{2}{k^2}\cos\varphi}. \tag{B.15}$$

From these relations an expression for the mirror eccentricity is derived:

$$e = \frac{k\sqrt{1 + \frac{1}{k^2} + \frac{2}{k}\cos\varphi}}{k-1}. \tag{B.16}$$

The primary mirror focal length f_p can be derived starting from the evaluation of the distance PF_1

$$PF1_{=}PQ + QF_1 \tag{B.17}$$

$$PF_1 = R_2/\cos/\varphi) + R_1 \tag{B.18}$$

$$\frac{2f_p}{1+\cos\varphi} = \frac{sh}{\cos\varphi} + \frac{sh}{k} \tag{B.19}$$

$$f_p = \frac{h}{2}\frac{(\cos\varphi + k)(1+\cos\varphi)}{k\cos\varphi}. \tag{B.20}$$

In order to evaluate the equivalent focal length of the system the angle (see eq B.4) between the two mirror major axis α has to be determined, this can be done applying the sines theorem to triangle QF_1F_2 , giving the result:

$$\sin\alpha = \frac{\sin\varphi}{k\sqrt{1+\frac{1}{k^2}+\frac{2}{k}\cos\varphi}}. \tag{B.21}$$

Computing the equivalent focal length according to eq B.4, a value around 200mm cannot be found. The system equivalent focal length has an inferior limit which is the distance from the horns array to the primary mirror h. Values as small as 200mm for h are not acceptable because they would imply shadowing of the beams reflected by the primary mirror by the horns array.

Acknowledgements

I would like to thank my supervisor M. Gervasi for guiding my work every day of these three years and for helping me every time I needed it. Moreover thanks to all the Radio Group of the University of Milano Bicocca for these three years of life spent together, especially Andrea for being a constant fellow to compare with and Marco P and Gigi for all the jokes.
Thanks to my students who are teaching me how to teach and be precise, in particular Dario for betting on me as his assistant supervisor for his degree thesis and all the other students I helped in their work of thesis.
I would like to thank the whole QUBIC team for all the fruitful discussions we had since the start of my PhD. Thanks to referees for helping me in making the thesis clearer, especially Creidhe for being so kind and precise.
Thanks to my parents: to my father for having as hobby what exactly is my work and to my mother for laughing on it.
Thanks to my friends who are walking in different paths towards the same goal.
Finally thanks to Mara for making everything possibile in my life. There will never be enough and adequate words to explain what you are doing for me. Just carry with you these words of gratefulness and remember that I will always be with you.